

WL-TR-96-2059



COMBUSTOR DESIGN MODEL EVALUATION

M.S. Anand, S. B. Pope*, and M. K. Razdan

**Allison Engine Company
P.O. Box 420
Indianapolis, IN 46206-0420**

***Sibley School of Mechanical and
Aerospace Engineering
Cornell University
Ithaca, NY 14853-7501**

APRIL 1996

FINAL REPORT FOR 10/01/87 - 01/31/96

Approved for public release; distribution unlimited

19960910 078

DTIC QUALITY INSPECTED 3

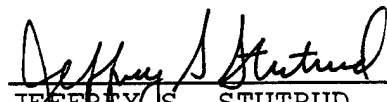
**AERO PROPULSION & POWER DIRECTORATE
WRIGHT LABORATORY
AIR FORCE MATERIEL COMMAND
WRIGHT-PATTERSON AIR FORCE BASE, OH 45433-7251**

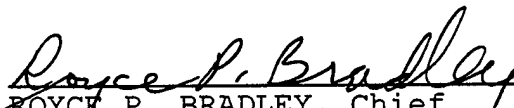
NOTICE


When Government drawings, specifications, or other data are used for any purpose other than in connection with a definitely Government-related procurement, the United States Government incurs no responsibility or any obligation whatsoever. The fact that the government may have formulated or in any way supplied the said drawings, specifications, or other data, is not to be regarded by implication, or otherwise in any manner construed, as licensing the holder, or any other person or corporation; or as conveying any rights or permission to manufacture, use, or sell any patented invention that may in any way be related thereto.

This report is releasable to the National Technical Information Service (NTIS). At NTIS, it will be available to the general public, including foreign nations.

This technical report has been reviewed and is approved for publication.


JEFFREY S. STUTRUD
Project Manager,
Combustion Branch


ROYCE P. BRADLEY, Chief
Combustion Branch


LEO S. HAROOTYAN, JR., Chief
Fuels and Lubrication Division

If your address has changed, if you wish to be removed from our mailing list, or if the addressee is no longer employed by your organization please notify WL/POSC, WPAFB, OH 45433-7103 to help us maintain a current mailing list.

Copies of this report should not be returned unless return is required by security considerations, contractual obligations, or notice on a specific document.

REPORT DOCUMENTATION PAGE			Form Approved OMB No. 0704-0188	
Public reporting burden for this collection of information is estimated to average 1 hour per response, including the time for reviewing instructions, searching existing data sources, gathering and maintaining the data needed, and completing and reviewing the collection of information. Send comments regarding this burden estimate or any other aspect of this collection of information, including suggestions for reducing this burden, to Washington Headquarters Services, Directorate for Information Operations and Reports, 1215 Jefferson Davis Highway, Suite 1204, Arlington, VA 22202-4302, and to the Office of Management and Budget, Paperwork Reduction Project (0704-0188), Washington, DC 20503.				
1. AGENCY USE ONLY (Leave blank)	2. REPORT DATE APRIL 1996	3. REPORT TYPE AND DATES COVERED FINAL 10/01/87-01/31/96		
4. TITLE AND SUBTITLE COMBUSTOR DESIGN MODEL EVALUATION		5. FUNDING NUMBERS C F33615-87-C-2821 PE 62203 F PR 3048 TA 05 WU 64		
6. AUTHOR(S) M. S. ANAND S. B. POPE* M. K. RAZDAN				
7. PERFORMING ORGANIZATION NAME(S) AND ADDRESS(ES) ALLISON ENGINE COMPANY *CORNELL UNIVERSITY PO BOX 420 UPSON HALL INDIANAPOLIS, IN 46206-0420 ITHACA, NY 14853		8. PERFORMING ORGANIZATION REPORT NUMBER EDR 13417Q		
9. SPONSORING / MONITORING AGENCY NAME(S) AND ADDRESS(ES) AERO PROPULSION AND POWER DIRECTORATE WRIGHT LABORATORY AIR FORCE MATERIEL COMMAND WRIGHT PATTERSON AFB OH 45433-7251 POC: JEFFREY STUTRUD, WL/POSL, 513-255-7461		10. SPONSORING / MONITORING AGENCY REPORT NUMBER WL-TR-96-2059		
11. SUPPLEMENTARY NOTES				
12a. DISTRIBUTION / AVAILABILITY STATEMENT APPROVED FOR PUBLIC RELEASE; DISTRIBUTION IS UNLIMITED.			12b. DISTRIBUTION CODE	
13. ABSTRACT (Maximum 200 words) The objective of the program was to evaluate, develop and validate more accurate computer-based analytical models for combustor flows to be used in combustor design. The joint velocity-scalar probability density function (pdf) method, which overcomes several key deficiencies of conventional turbulent combustion models and offers greater accuracy for combustor design calculations, is the focus of the program. Significant progress has been made under this program towards the development of the pdf method as a combustor design tool. Several new models and algorithms used in the pdf method have been developed. The method and the models have been validated in detail for a variety of flows, including swirling, recirculating and reacting flows, involving the essential features of gas turbine combustor flows. The validation was performed using available benchmark quality data, as well as data from specifically designed experiments which were performed at Wright Laboratory. A baseline pdf based combustor design system has been developed.				
14. SUBJECT TERMS Combustor Design Models, Combustor Design Systems, Turbulent Combustion, Probability Density Function (PDF) Method			15. NUMBER OF PAGES 148	
			16. PRICE CODE	
17. SECURITY CLASSIFICATION OF REPORT UNCLASSIFIED	18. SECURITY CLASSIFICATION OF THIS PAGE UNCLASSIFIED	19. SECURITY CLASSIFICATION OF ABSTRACT UNCLASSIFIED	20. LIMITATION OF ABSTRACT SAR	

TABLE OF CONTENTS

<u>Section</u>	<u>Title</u>	<u>Page</u>
SUMMARY		xii
ACKNOWLEDGMENTS.....		xiv
LIST OF FIGURES.....		vii
1. INTRODUCTION.....		1-1
1.1 Program Objectives		1-2
1.2 Overview of the Present Study.....		1-2
2. THE PROBABILITY DENSITY FUNCTION (PDF) METHOD.....		2-1
2.1 Background		2-1
2.1.1 The Turbulence Closure Problem		2-2
2.1.2 Chemistry/Reaction Rates.....		2-3
2.1.3 Scalar Transport.....		2-4
2.1.4 Turbulence/Chemistry Interactions		2-4
2.2 Description of the PDF Method		2-5
2.2.1 The PDF Transport Equation.....		2-7
2.2.2 Modeling and Solution of the PDF Transport Equation		2-9
2.3 Previous Work		2-12
2.4 Key Accomplishments under the Present Study.....		2-14
3. MODELS FOR VELOCITY AND TURBULENCE FREQUENCY		3-1
3.1 Mean Frequency Model (MFM).....		3-1
3.2 Simple Langevin Model I for Velocity using MFM (SLM I)		3-2
3.3 Stochastic Frequency Model I (SFM I)		3-2
3.4 Refined Langevin Model for Velocity using SFM I (RLM).....		3-3
3.5 Stochastic Frequency Model II (SFM II)		3-4
3.6 Simple Langevin Model II for Velocity using SFM II (SLM II).....		3-5
4. MODELS FOR MOLECULAR MIXING OF SCALARS		4-1
4.1 Improved Mixing Model (IMM)		4-1
4.2 Interaction by Exchange with the Mean (IEM) Model.....		4-2

TABLE OF CONTENTS (Cont)

<u>Section</u>	<u>Title</u>	<u>Page</u>
5.	ALGORITHMS TO DETERMINE MEAN PRESSURE	5-1
5.1	Boundary Layer Algorithm	5-1
5.2	Mean Pressure Algorithm I for Elliptic Flows	5-3
5.3	Mean Pressure Algorithm II for Elliptic Flows	5-4
6.	COAXIAL JET FLOWS	6-1
6.1	Overview	6-1
6.2	Background	6-1
6.3	Modeling Considerations	6-2
6.3.1	Intermittency	6-2
6.3.2	Calculations with Uniform $\langle \omega \rangle$	6-2
6.4	Flow Description and Computational Details	6-3
6.5	Results and Discussion	6-5
6.6	Summarizing Remarks	6-11
7.	CONSTANT-DENSITY SWIRLING JET FLOWS	7-1
7.1	Overview	7-1
7.2	Background	7-1
7.3	The Joint PDF Method and Models Used	7-2
7.4	Flow Description and Computational Details	7-3
7.4.1	Flow Description	7-3
7.4.2	Initial Conditions	7-3
7.4.3	Conditional Statistics	7-5
7.4.4	Computational Parameters	7-6
7.5	Results and Discussion	7-6
7.6	Summarizing Remarks	7-18
8.	SWIRLING JET DIFFUSION FLAMES	8-1
8.1	Overview	8-1
8.2	Background	8-1
8.3	Experimental Setup and Techniques	8-2
8.4	Computations	8-4
8.4.1	The Joint PDF Method and Models Used	8-4

TABLE OF CONTENTS (Cont)

<u>Section</u>	<u>Title</u>	<u>Page</u>
8.4.2	Thermochemistry	8-5
8.4.3	Initial Conditions.....	8-6
8.5	Results and Discussion.....	8-6
8.7	Summarizing Remarks.....	8-18
9.	BACKWARD FACING STEP FLOW	9-1
9.1	Overview	9-1
9.2	Background	9-1
9.3	Test Case and Initial Conditions.....	9-2
9.4	Computations with Pressure Algorithm I.....	9-3
9.4.1	Computational Details.....	9-3
9.4.2	Results and Discussion	9-4
9.4.3	Summarizing Remarks	9-10
9.5	Computations with Pressure Algorithm II	9-10
10.	SWIRLING AND RECIRCULATING FLOW COMBUSTORS	10-1
10.1	Overview	10-1
10.2	Background	10-1
10.3	Computational Details	10-1
10.3.1	The PDF Method -- Modeling and Solution Algorithm	10-1
10.3.2	Thermochemistry.....	10-2
10.4	Results and Discussion.....	10-3
10.4.1	Swirling Hydrogen Diffusion Flame.....	10-3
10.4.2	Methane Step-Swirl Combustor	10-10
10.5	Summarizing Remarks.....	10-15
11.	ASSESSMENT OF PDF VERSUS CONVENTIONAL MODELS	11-1
11.1	Overview	11-1
11.2	Background	11-1
11.3	Description of Models Used for Comparison.....	11-2
11.3.1	Laminar Chemistry and Eddy Breakup Models.....	11-2
11.3.2	Assumed PDF Model.....	11-2
11.3.3	The Scalar PDF Method	11-2
11.4	Description of the Solution Methods Used.....	11-3

TABLE OF CONTENTS (Cont)

<u>Section</u>	<u>Title</u>	<u>Page</u>
11.4.1	The Scalar PDF Method	11-3
11.4.2	Finite-Volume Method	11-3
11.4.2	The Joint PDF Method	11-4
11.5	Thermochemistry	11-4
11.6	Results and Discussion	11-5
11.6.1	Swirling Hydrogen Jet Diffusion Flame	11-5
11.6.2	Step-Swirl Methane Combustor	11-6
11.7	Computations for a Low Emissions Lean Premixed Combustor	11-15
11.8	Summarizing Remarks	11-18
12.	CONCLUDING REMARKS	12-1
APPENDIX:	LIST OF PUBLICATIONS	A-1

LIST OF FIGURES

<u>Figure</u>	<u>Title</u>	<u>Page</u>
6-1	Initial conditions for normalized mean axial velocity and Reynolds stresses. Symbols represent experimental data; solid lines are calculated from initial pdf. $\langle w^2 \rangle$ is similar to $\langle v^2 \rangle$	6-4
6-2	Initial profiles of turbulence frequency $\langle \omega \rangle$ and mean of the conserved scalar $\langle \phi \rangle$. .	6-5
6-3	Comparison of results for cases (A) with conditional modeling and uniform $\langle \omega \rangle$, (B) without conditional modeling and uniform $\langle \omega \rangle$, and (C) without conditional modeling and nonuniform $\langle \omega \rangle$, at two axial stations. Symbols represent experimental data.	6-6
6-4	Computed (Case C) radial profiles of normalized mean axial velocity and turbulent kinetic energy compared against experimental data at various axial stations. . . .	6-7
6-5	Computed (Case C) radial profiles of normalized Reynolds stresses compared against experimental data at various axial stations.	6-8
6-6	Computed radial profiles of $\langle \omega \rangle$ for Case C ($\sigma_\omega = 1.0$), Case B (uniform $\langle \omega \rangle$), and the two other values of σ_ω compared at different axial stations.	6-9
6-7	Mean axial velocity profiles from calculations with three different values of coflow velocity U_b	6-11
7-1	Radial profiles of conditional mean axial velocity from pdf (stochastic velocity-frequency model) calculations compared against data at various axial stations. . . .	7-7
7-2	Radial profiles of conditional mean axial velocity from pdf ($\langle \omega \rangle$ -model) calculations compared against data at various axial stations (see Figure 7-1 for legend)	7-8
7-3	Profiles of mean relaxation rate $\langle \omega \rangle$ from stochastic model calculations (solid lines) compared with those from $\langle \omega \rangle$ -model calculations (dashed lines) at various axial stations.	7-9
7-4	Profiles of conditional mean swirl velocity $\langle W \rangle$ from stochastic model calculations compared against data (see Figure 7-1 for legend).	7-10
7-5	Profiles of conditional turbulent kinetic energy from stochastic model calculations compared against data (see Figure 7-1 for legend).	7-11

LIST OF FIGURES (Cont)

<u>Figure</u>	<u>Title</u>	<u>Page</u>
7-6	Profiles of conditional and unconditional mean axial velocity and turbulent kinetic energy at $x/D = 5.29$ from stochastic model calculations. Solid line - jet fluid; short dashed line - annular jet fluid; long dashed line - coflow; extra long dashed line - unconditional.....	7-12
7-7	Profiles of conditional axial velocity variance from stochastic model calculations compared against data (see Figure 7-1 for legend)..	7-13
7-8	Profiles of conditional axial velocity variance from $\langle\omega\rangle$ -model calculations compared against data (see Figure 7-1 for legend)..	7-13
7-9	Profiles of (conditional) triple correlation $\langle u^2 v \rangle$ from stochastic model calculations compared against data (see Figure 7-1 for legend).....	7-14
7-10	Profiles of (conditional) triple correlation $\langle u^2 v \rangle$ from $\langle\omega\rangle$ -model calculations compared against data (see Figure 7-1 for legend).....	7-14
7-11	Profiles of (unconditional) triple correlation $\langle u^2 v \rangle$ from stochastic model calculations (solid line); from Reynolds-stress model (Eq. 7.6) using results from Reynolds-stress closure calculations (short dashed line); and from model (Eq. 7.6) using results from stochastic model calculations (long dashed line).....	7-16
7-12	Profiles of conditional $\langle u^3 \rangle$ from stochastic model compared against data (see Figure 7-1 for legend).....	7-17
7-13	Profiles of (conditional) fourth-order correlation $\langle w^4 \rangle$ from stochastic model calculations compared against data (see Figure 7-1 for legend).....	7-17
7-14	Profiles of (conditional) fourth order correlation $\langle w^4 \rangle$ from $\langle\omega\rangle$ -model compared against data (see Figure 7-1 for legend).....	7-18
8-1	Schematic of the Swirling Jet Diffusion Flame Combustor test section.....	8-3
8-2	Radial profiles of computed conditional and unconditional mean axial velocity (lines) compared against data (symbols) for the nonswirling case (Case 2).	8-10
8-3	Computed profiles of Favre-averaged mean temperature ($\langle T \rangle$) and Reynolds-averaged mean temperature (\bar{T}) compared against data (symbols) for the nonswirling case (Case 2).	8-10
8-4	Computed profiles of Favre-averaged temperature variance ($\langle T'^2 \rangle$) and Reynolds-averaged temperature variance ($\bar{T'^2}$) compared against data (symbols) for the nonswirling case (Case 2).....	8-11

LIST OF FIGURES (Cont)

<u>Figure</u>	<u>Title</u>	<u>Page</u>
8-5	Radial profiles of computed conditional mean axial velocity (lines) compared against data (symbols) for the 30 degree swirl case (Case 3).....	8-11
8-6	Radial profiles of computed conditional mean tangential velocity (lines) compared against data (symbols) for the 30 degree swirl case (Case 3).....	8-12
8-7	Computed profiles of Reynolds-averaged mean temperature with (solid lines) and without (dotted lines) the inclusion of molecular diffusion compared against data (symbols) for the 30 degree swirl case (Case 3).....	8-12
8-8	Computed profiles of Reynolds-averaged temperature variance (lines) compared against data (symbols) for the 30 degree swirl case (Case 3).....	8-15
8-9	Radial profiles of computed conditional mean axial velocity (lines) compared against data (symbols) for the 45 degree swirl case (Case 4).....	8-15
8-10	Radial profiles of computed conditional mean tangential velocity (lines) compared against data (symbols) for the 45 degree swirl case (Case 4)..	8-16
8-11	Computed profiles of Reynolds-averaged mean temperature (lines) compared against data (symbols) for the 45 degree swirl case (Case 3).....	8-16
8-12	Radial profiles of computed conditional turbulent kinetic energy (lines) compared against data (symbols) for the 30 degree swirl case (Case 3).....	8-17
8-13	Radial profiles of computed conditional turbulent shear stress (lines) compared against data (symbols) for the 30 degree swirl case (Case 3).....	8-17
8-14	Radial profiles of computed conditional triple correlation $\langle u^2 v \rangle$ (lines) compared against data (symbols) for the 30 degree swirl case (Case 3).....	8-18
8-15	Radial profiles of computed conditional fourth moment $\langle v^4 \rangle$ (lines) compared against data (symbols) for the 30 degree swirl case (Case 3).....	8-18
9-1	Schematic of the flow considered. Backward-facing step studied experimentally by Pronchick and Kline (1983).	9-2
9-2	Computed mean streamwise velocity profiles (lines) compared against data (symbols).	9-5
9-3	Computed mean transverse velocity profiles (lines) compared against data (symbols).	9-5
9-4	Computed streamwise velocity variance profiles (lines) compared against data (symbols).	9-6

LIST OF FIGURES (Cont)

<u>Figure</u>	<u>Title</u>	<u>Page</u>
9-5	Computed transverse velocity variance profiles (lines) compared against data (symbols).	9-6
9-6	Computed shear stress profiles (lines) compared against data (symbols)..	9-7
9-7	Computed $\langle u^3 \rangle$ profiles (lines) compared against data (symbols)..	9-7
9-8	Computed $\langle v^3 \rangle$ profiles (lines) compared against data (symbols)..	9-8
9-9	Computed $\langle u^2 v \rangle$ profiles (lines) compared against data (symbols)..	9-8
9-10	Computed $\langle v^2 u \rangle$ profiles (lines) compared against data (symbols) ..	9-9
9-11	Computed contours of mean pressure (normalized by ρU_{ref}^2) ..	9-9
10-1	Schematic of the hydrogen swirling jet diffusion flame configuration..	10-4
10-2	Convergence history for the mean axial and radial velocities for the hydrogen flame computations..	10-5
10-3	Computed mean axial velocity profiles compared against data for the hydrogen flame.	10-7
10-4	Computed mean swirl velocity profiles compared against data for the hydrogen flame.	10-7
10-5	Computed mean temperature profiles compared against data for the hydrogen flame.	10-8
10-6	Computed turbulent kinetic energy profiles compared against data for the hydrogen flame.....	10-8
10-7	Computed profiles of higher-order turbulent correlations compared against data for the hydrogen flame.....	10-9
10-8	Schematic of the step-swirl combustor. The fuel used is methane.	10-10
10-9	Computed mean axial velocity profiles (lines) compared against data (symbols) for the methane flame.	10-12
10-10	Computed mean radial velocity profiles (lines) compared against data (symbols) for the methane flame.	10-12
10-11	Computed mean swirl velocity profiles (lines) compared against data (symbols) for the methane flame	10-13
10-12	Computed mean temperature profiles (lines) compared against data (symbols) for the methane flame.	10-13
10-13	Computed turbulent kinetic energy profiles (lines) compared against data (symbols) for the methane flame.....	10-14

LIST OF FIGURES (Cont)

<u>Figure</u>	<u>Title</u>	<u>Page</u>
10-14	Computed profiles of fourth moment of axial velocity (lines) compared against data (symbols) for the methane flame.	10-14
11-1	Computed axial velocity profiles compared with experimental data for the swirl hydrogen flame.....	11-7
11-2	Computed swirl velocity profiles compared with experimental data for the swirl hydrogen flame.	11-7
11-3	Computed turbulent kinetic energy profiles compared with experimental data for the swirl hydrogen flame.	11-8
11-4	Solutions for the mean temperature compared with experimental data for the swirl hydrogen flame.....	11-8
11-5	Solutions for the temperature variance compared with experimental data for the swirl hydrogen flame.....	11-9
11-6	Computed axial velocity profiles compared with experimental data for the step-swirl methane combustor.....	11-12
11-7	Computed radial velocity profiles compared with experimental data for the step-swirl methane combustor.....	11-12
11-8	Computed swirl velocity profiles compared with experimental data for the step-swirl methane combustor.....	11-13
11-9	Computed turbulent kinetic energy profiles compared with experimental data for the step-swirl methane combustor.	11-13
11-10	Computed mean temperature profiles compared with experimental data for the step-swirl methane combustor.	11-14
11-11	Schematic of the RSPN low emissions combustor module.	11-16
11-12	Contour plots of mean mixture fraction, temperature and axial velocity computed using the pdf method for the RSPN low emissions combustor. PDF methods offer unique capability for premixed combustor design. (Scalar PDF is used here.)	11-17

SUMMARY

The main objective of the Combustor Design Model Evaluation program is to evaluate, develop and validate quantitatively accurate advanced analytical methods and models to meet the challenges of designing advanced combustors. The main challenge is to design combustors, that meet stringent requirements of combustor aerothermal performance, emissions, operability, exhaust signature and durability, in a cost- and time-effective manner through greater reliance on analytical design methods.

The specific objectives of the program are to:

- Develop and validate more accurate computer-based analytical models for combustor flows.
- Design benchmark quality experiments and use the data from advanced diagnostic measurements for such development and validation.
- Incorporate the analytical models into a next-generation gas turbine combustor design system and assess its capabilities.

The joint velocity-scalar probability density function (pdf) method (or joint pdf method for short) is the focus of the model development and validation efforts at Allison under this program. The pdf method was selected as the most promising candidate for further development as a combustor design tool after a review of several current and evolving approaches. The pdf method overcomes the main deficiencies of the current models; turbulent transport and turbulence/chemistry interactions appear in closed form in the pdf method and need not be modeled. Significant previous development work with the method had demonstrated its advantages over conventional models and its feasibility for development as a combustor design tool. However, considerable work needed to be done in order for the method to be used for the complex swirling recirculating flow fields in practical combustors.

Benchmark experimental configurations were designed in conjunction with Wright Laboratory, Combustion Branch (WL/POSC) personnel and University of Dayton Research Institute (UDRI) personnel. Measurements were made by UDRI personnel at WL/POSC under a separate program. These data as well as data available from other sources (such as data from NASA Hot Section Technology [HOST] programs) were used for model validation in the current program.

Substantial progress has been made under the current program in developing and validating the pdf method for complex flows such as in gas turbine combustors. The primary areas of

progress have been in the development of the models for the turbulent frequency and the development of the algorithms for determining the mean pressure field within the pdf calculations. Other areas have included the treatment of swirling flows and treatment near solid walls. These developments are key to the application of the pdf method to complex flows of practical interest. The pdf method has been applied to variety of swirling, recirculating, nonreacting and reacting flows under this program. Results from pdf calculations are in excellent agreement with detailed benchmark experimental data for temperature and turbulent velocity correlations up to fourth order. The results from the joint pdf method have been assessed against the results from other conventional methods as well as the scalar pdf method (a subset of the joint pdf method). The pdf methods have been shown to be more accurate than conventional turbulent combustion models. A baseline design system based on the pdf methods has been developed. Areas of further development to fully utilize the design system have been identified and discussed. All the program objectives have been achieved.

ACKNOWLEDGMENTS

The work was performed under the U. S. Air Force contract No. F33615-87-C-2821 from Wright Laboratory (WL), Wright Patterson AFB. The authors would like to thank the Air Force technical monitors Dr. Mel Roquemore and Mr. Jeff Stutrud for their support, useful discussions and coordination of the experiments at WL. Thanks are also due to Messrs. Curtis Reeves, Dale Shouse and Jeff Liffick who served as technical monitors in the past.

The computer resources of NASA's National Aerodynamic Simulation (NAS) program at NASA, Ames, were used for many of the computations performed in this program, under grants from NASA Lewis Research Center. We would like to thank Dr. Lou Povinelli and Dr. Ed Mularz of NASA Lewis for their support and for sponsoring the NAS grants.

We would like to thank Dr. Fumi Takahashi and other University of Dayton Research Institute (UDRI) personnel for their meticulous efforts to produce benchmark quality data for model validation, and Dr. Dilip Ballal for heading up the UDRI effort.

We would like to acknowledge the contribution of Dr. Andrew Hsu of Allison who performed the assessment study presented in Chapter 11.

1. INTRODUCTION

Future high performance gas turbine engines are placing exacting requirements on combustor design in regard to aerothermal performance, emissions, operability, exhaust signature, durability and combustor envelope. To meet these requirements in a cost- and time-effective manner, improved combustor design systems are needed that are based on fundamentally sound and quantitatively accurate physicochemical models of combustion processes. The accuracy in modeling these processes is key to the accurate prediction of critical combustion performance characteristics such as efficiency, emissions, exit and wall temperatures, lean blowout, stability, flashback, autoignition, etc., in advanced high performance and low emissions combustor concepts.

Current combustor design systems lack the quantitative accuracy needed for the reliable analytical predictions of key combustor operating characteristics. This deficiency results in high costs and time involved in the prolonged testing needed during the combustor design and development phase. The current design system relies on considerable empiricism and "experience database." This approach has limited utility when radically new concepts and designs for the combustors are becoming inevitable due to the increasingly stringent requirements and aggressive goals for the combustors as well as the engines as a whole. The limitations of the current design system stem mainly from the deficiencies in the physicochemical models for the key combustion processes such as the treatment of the turbulent transport of momentum and scalars, and the two-way interactions between turbulence and reactions. Conventional turbulent combustion models suffer from the turbulence closure problem (need to model the turbulent transport) and the inability to treat realistic finite-rate reactions in a turbulent flow field. A fundamentally different approach is needed to address these critical issues.

An important aspect of any model development activity is the validation of the model results against reliable benchmark quality data. This comparison serves to validate the model as well as to guide the improvements needed for the model. The benchmark experiments must be designed and carried out such that they provide accurate inlet and boundary conditions as well as the measurements within the flow field for all the quantities needed for the computations and model validation. At the same time, the combustor geometries should be simple enough to permit the accurate simulation of the flow geometry to focus attention on the modeling issues. Finally, the developed model needs to be assessed for its ability to compute gas turbine combustor flows. This assessment again needs to be performed by comparison against benchmark quality

measurements for laboratory combustors which incorporate the essential features of gas turbine combustors.

The current program seeks to address the above issues through the development and validation of a fundamentally different and more accurate analytical combustor design model. The program objectives are presented in the next section. The overview of the program, including a brief description of the approach and the key achievements under the program are given in the following subsection. An overview of the rest of this report is also presented in that subsection.

1.1 Program Objectives

The objectives of this program are the following:

- Develop and validate more accurate computer-based analytical models for combustor flows.
- Design benchmark quality experiments and use the data from advanced diagnostic measurements for such development and validation.
- Incorporate the analytical models into a next-generation gas turbine combustor design system and assess its capabilities.

1.2 Overview of the Present Study

The joint velocity-frequency-scalar probability density function (pdf) method (or joint pdf method for short) is the focus of the model development and validation efforts at Allison under this program. The pdf method was selected as the most promising candidate for further development as a combustor design tool after a review of several current and evolving approaches. The pdf method overcomes the main deficiencies of the current models; turbulent transport and turbulence/chemistry interactions appear in closed form in the pdf method and need not be modeled. Before the start of the current program, significant progress had been made in the development of the pdf approach and its advantages over current methods had been demonstrated for several simple reacting and nonreacting flows. However, considerable work needed to be done in order for the method to be used for the complex swirling recirculating flow fields in practical combustors.

A review of existing benchmark quality data showed that substantial voids existed in the data with respect to availability of inlet condition measurements as well the quality and completeness

of the data. Also, benchmark quality data (meeting the criteria described above) for swirling and recirculating reacting flows were almost nonexistent. Hence benchmark experimental configurations were designed in conjunction with Wright Laboratory, Combustion Branch (WL/POSC) personnel and University of Dayton Research Institute (UDRI) personnel. Measurements were made by UDRI personnel at WL/POSC under a separate program. These data as well as any suitable data from other sources (such as data from NASA Hot Section Technology [HOST] programs) were used for model validation in the current program.

Substantial progress has been made under the current program in developing and validating the pdf method for complex flows such as in gas turbine combustors. The primary areas of progress have been in the development of the models for the turbulent frequency and the development of the algorithms for determining the mean pressure field within the pdf calculations. Other areas have included the treatment of swirling flows and treatment near solid walls. These developments are key to the application of the pdf method to complex flows of practical interest. The pdf method has been applied to variety of swirling, recirculating, nonreacting and reacting flows under this program. Results from pdf calculations are in excellent agreement with detailed benchmark experimental data for temperature and turbulent velocity correlations up to fourth order. The results from the joint pdf method have been assessed against the results from other conventional methods as well as the scalar pdf method (a subset of the joint pdf method). The pdf methods have been shown to be more accurate than conventional turbulent combustion models. A baseline design system based on the pdf methods has been developed. All the program objectives have been achieved.

In Chapter 2 of this report, a discussion of the important modeling issues for gas turbine combustor flows and the unique advantages offered by the pdf method over other methods is presented. It is followed by a description of the pdf method including the governing equations, the modeling, solution algorithm and the key model development efforts under the program. The models for velocity and turbulent frequency developed and used under this program are described in Chapter 3. The models used for the molecular mixing of scalars are described in Chapter 4. The algorithms developed for determining the mean pressure field used in the pdf solution are described in Chapter 5. The determination of the mean pressure field and the associated pdf solution algorithm is an important aspect in making pdf calculations for complex elliptic recirculating flows. Chapters 6 through 10 describe the application and validation of the pdf method and its models for a wide range of flows of varying complexities. Available benchmark quality data as well as new experiments designed and conducted to provide benchmark data are also described in those chapters. The joint pdf calculations are assessed against results from the scalar pdf method and several conventional models in Chapter 11.

Concluding remarks and areas of further development of the pdf-based design system are presented in Chapter 12.

2. THE PROBABILITY DENSITY FUNCTION (PDF) METHOD

2.1 Background

A combustor design methodology based on advanced analytical tools can be used with confidence in the design of advanced gas turbine combustion systems if the various physicochemical processes occurring in the combustor are accurately modeled and simulated. These processes include the mean flow dynamics; turbulent transport of momentum and scalars; molecular mixing of scalars; reaction kinetics; spray injection, droplet formation, dispersion, and evaporation; soot formation and oxidation; convective and radiative heat transfer; and the interactions between the different processes, namely turbulence/chemistry interactions, turbulence/spray dynamics interactions, etc. In addition, accurate numerical schemes and solution algorithms are needed to solve the governing equations for these processes to obtain quantitatively accurate predictions for the combustor flow and performance characteristics.

The model development and validation efforts under this program take into account all the above aspects, although the primary attention is focussed on the simulation of the turbulent reacting flow field (i.e., mean flow, turbulence, scalar transport, reactions, and their interactions). Several past and ongoing work at Allison and elsewhere focus on the advanced spray and evaporation models and heat transfer. Attention is paid in the development of the method in the current program so that the method is compatible with the spray and other advanced models and that those models can be easily incorporated.

The main difficulties in computing practical turbulent reacting flows, such as in gas turbines, arise due to the simultaneous presence of turbulence, mean and fluctuating strain rates and pressure gradients, swirl, body forces, scalar transport, complex finite-rate reactions and the interactions between the various processes. Conventional Reynolds-averaged approaches, which are widely used currently, suffer from the "turbulence closure problem," inability to treat complex finite-rate reactions and to accurately account for the interactions between turbulence and reactions. The probability density function (pdf) method used and developed in the present study are remarkably successful in alleviating the major difficulties; the effects of turbulent transport, complex finite-rate reactions, body forces, variable-density, mean pressure gradients, and turbulence chemistry interactions are in closed form and can be treated without approximation. The only remaining closure problems are due to the fluctuating pressure gradient

and to molecular transport (including effects of fluctuating velocity and scalar gradients). Some of these issues and the advantages of the pdf method are discussed in more detail in the following subsections.

2.1.1 The Turbulence Closure Problem

In conventional Reynolds-averaged approaches, turbulence models are needed to overcome the classical turbulence closure problem, i.e. the normal and shear stresses (the so-called Reynolds stresses) are unknown in the mean momentum equations. The gradients of the Reynolds stresses that appear in the mean momentum equations represent the turbulent convective transport of momentum. In mean-flow closure models, such as the k- ϵ model [2-1]¹, the Reynolds stresses are related to the mean velocity gradients through an isotropic eddy viscosity, based on the gradient diffusion (or gradient transport) assumption. Although, robust and reasonably successful in predicting a variety of turbulence flows, the k- ϵ model has serious limitations for accurately predicting the location and extent of recirculation zones and flows with significant streamline curvature such as in curved boundary-layers and swirling flows, since the assumption of isotropic eddy viscosity is erroneous for such flows [2-2, 2-3]. Several modifications to the k- ϵ model have been proposed over the years but they have had only partial successes in overcoming the fundamental problems with the models.

The next level of closure in the Reynolds-averaged approach is the second-order closure, in which transport equations for the Reynolds stresses are solved or approximated through algebraic relations [e.g., 2-4, 2-5]. However, in these equations the third-order correlations, which represent the turbulent convective transport of the Reynolds stresses, are unknown and need to be modeled. Again, the modeling approach adopted is to relate the third-order correlations to the Reynolds stresses through gradient diffusion assumptions. The second-order closure models better account for the anisotropy of turbulent transport. While they have produced better results than the k- ϵ model for many flows especially with streamline curvature, they have not been unequivocally established as a superior alternative to the k- ϵ model. The robustness and the simplicity of the k- ϵ model compared to the second-order models make the former a more widely used choice for complex practical flows.

The main drawback of both classes of turbulence models, the mean and second-order closures, is the assumption of gradient transport. The assumption is essentially ad hoc and is not valid for many flows, especially variable-density and reacting flows [2-6]. With the joint velocity-scalar

¹ References are listed at the end of each section

pdf method [2-7], the turbulence closure problem described above does not exist and hence the gradient transport assumptions are avoided. The convective transport by both mean and turbulent velocities appear in closed form and need not be modeled.

An alternative approach to computing turbulent flows is direct numerical simulation (DNS) [2-8]. DNS attempts to simulate the stochastic flow field exactly, by considering the instantaneous Navier-Stokes equations. To truly simulate the turbulent processes, the numerical simulation should resolve the smallest scales of turbulence. This fact puts severe restrictions on the magnitude of the Reynolds number of the flows that can be simulated even with the present day high-speed and large-storage computers. DNS cannot be used for computing flows in practical geometries of interest, much less as a design tool for gas turbine combustors for many years to come. The utility of DNS lies largely in providing guidance for developing other turbulent combustion models. Indeed DNS has been used to develop the turbulence frequency models developed for the pdf method (see Section 3.2). In another approach, large eddy simulation (LES), only the large energy-containing scales are resolved and the subgrid scales are modeled. It is still very computer intensive and impractical for design calculations. Moreover, it has the same limitations as conventional approaches for calculating reacting flows (see next subsection).

2.1.2 Chemistry/Reaction Rates

For reacting flows, the turbulence models, such as k - ϵ and Reynolds stress models, need to be extended to include additional models for scalar flux, mean reaction rates, correlations involving instantaneous reaction rates, and models to account for additional effects of variable density.

Combustion of practical fuels typically involve several hundred coupled reactions and tens of species. The rates of these reactions vary exponentially with temperature and are non-linearly dependent on species concentrations (Arrhenius rate expressions). In Reynolds-averaged approaches the mean reaction rate, i.e., the mean of the instantaneous Arrhenius reaction rates based on the instantaneous temperature and composition values, is needed in the calculation. The most prevalent current practice with these approaches is to use the Arrhenius reaction rate corresponding to the mean temperature and composition rather than the mean of the instantaneous rates. Given the highly nonlinear reaction rates and the large turbulent fluctuations in temperature and composition, such a practice can lead to an order-of-magnitude error in the value of the reaction rate and can even yield the wrong sign [2-9]. The current combustion models can determine mean reaction rates accurately only under very restrictive special cases

(when all the reaction rates are linear and weakly coupled or when the entire combustion process is very fast or very slow). A general nonlinear, finite-rate, multi-step reaction mechanism cannot be treated by these conventional models.

The most striking advantage of the pdf method is its ability to treat arbitrarily complex, finite-rate, coupled multi-step reactions without approximations. (Although this is theoretically true, reasonable simplifications of the chemistry may be required to reduce computer resource requirements. There is ongoing work aimed at developing efficient computational procedures without requiring simplification.)

There are several past and ongoing efforts to overcome the reaction closure problem in the Reynolds-averaged methods, such as laminar flamelet model, assumed pdf approaches, conditional moment closure, etc., but all of them are based on restrictive simplifying assumptions and none of them has the advantage that the pdf method has for treating reactions in the turbulent combustion of practical fuels without approximation. Another combustion model, the linear eddy model, has many similarities with the pdf method for treating the reactions but lacks the rigor of the pdf method in its formulation nor is it directly applicable to multidimensional flows.

2.1.3 Scalar Transport

In addition to the mean reaction rates, the calculation of scalar transport (i.e., transport of species and other scalars) is important in turbulent reacting flows. In conventional Reynolds-averaged approaches, the turbulent flux of the scalar needs to be modeled while solving the conservation equation for the scalar. The same ideas behind the modeling of the Reynolds stresses (section 2.1.1), namely gradient diffusion, are applied for the modeling of scalar fluxes as well. As with the momentum flux, the gradient diffusion assumptions for scalar flux can be erroneous especially in reacting flows (see section 2.1.4). With the joint pdf method, the (mean and) turbulent flux of scalar is in closed form and need not be modeled.

2.1.4 Turbulence/Chemistry Interactions

Several processes such as turbulence production and dissipation, turbulent transport, reaction and the accompanying heat release and volume expansion, occurring in turbulent combustion are strongly interconnected. The effect of turbulent fluctuations on mean reaction rates was described in Section 2.1.2. In turn, the turbulence is influenced by the reaction.

The volume expansion (density change) resulting from reaction affects turbulence production and dissipation through changes in velocity gradients and interactions between variable-density

and the mean pressure gradients. While these effects are difficult to model in the conventional approaches, they appear in closed form in the joint pdf method and need not be modeled.

Another important effect of the heat release is the occurrence of the phenomenon of counter-gradient diffusion [2-10, 2-11] in which the scalar flux and the scalar gradient are of the same sign in certain regions of the flow contrary to conventional gradient transport modeling assumption. A more general case of this phenomenon is when the scalar flux vector is aligned at an angle other than diametrically opposite to the scalar gradient [2-12, 2-13]. The reason for this phenomenon lies in the fact that the difference between the densities of the reactants and the products can be quite large, and the strong mean pressure gradient across the reaction zone imparts greater acceleration to the low-density products than to the reactants. None of the conventional models can treat this phenomenon in a general way. Special models are used for particular situations under consideration [2-10, 2-14]. With the joint pdf method, the phenomenon of counter-gradient diffusion and other variable-density effects are automatically calculated as demonstrated by Anand et al. [2-11, 2-13].

In summary, the joint pdf method is inherently successful in overcoming the most important modeling difficulties, such as turbulent transport, complex reactions, and turbulent chemistry interaction. The pdf method provides a more complete description of the turbulent flow field than the conventional models that usually calculate only the first and second moments. In addition, when there are multiple streams or fluids conditional modeling is easily accomplished in the pdf method. Effects of large scale structures and phenomena such as intermittency, unmixedness, etc. can be accounted for. These advantages make the pdf method the most suitable approach for computing turbulent reacting flows and warrant its development as a gas turbine combustor design tool.

2.2 Description of the PDF Method

There is a hierarchy of pdf methods currently in use. They are based on (a) the joint pdf of compositions ϕ , (b) the joint pdf of velocity and composition, \underline{U} , ϕ , and (c) the joint pdf of velocity, turbulent frequency and composition, \underline{U} , ω , ϕ . Methods (b) and (c) are referred to as the joint pdf method in this report and method a) is referred to as the scalar pdf method. The primary focus of the present study is on the most advanced and comprehensive method (c), while work with method (b) has also been performed. The scalar PDF method overcomes the difficulty with treating complex chemistry/reaction rates (section 2.1.2) and the effect of turbulence on chemistry. The joint pdf method in addition overcomes the turbulent transport issue (of

momentum and scalars) and more comprehensively treats the two-way interactions between turbulence and chemistry (section 2.1.4).

The joint pdf approach involves the solution of the transport equation of the velocity-frequency-scalar pdf. The joint PDF $f(\underline{V}, \eta, \underline{\psi}; \underline{x}, t)$, is the probability density of the occurrence of the simultaneous event $\underline{U}(\underline{x}, t) = \underline{V}$, $\omega(\underline{x}, t) = \eta$ and $\phi(\underline{x}, t) = \underline{\psi}$, where \underline{U} is the velocity vector, ω is the turbulence frequency, ϕ is a set of scalars and \underline{V} , η , and $\underline{\psi}$ are independent variables in the velocity, frequency and scalar spaces respectively. Any single point correlation (means, variances, third moments, etc.) at a position \underline{x} and time t can be evaluated from the following properties of the joint pdf:

$$\overline{Q(\underline{U}, \omega, \underline{\phi})} = \iiint Q(\underline{V}, \eta, \underline{\psi}) f(\underline{V}, \eta, \underline{\psi}; \underline{x}, t) d\underline{V} d\eta d\underline{\psi}, \quad (2.1)$$

$$\iiint f(\underline{V}, \eta, \underline{\psi}; \underline{x}, t) d\underline{V} d\eta d\underline{\psi} = 1. \quad (2.2)$$

The integrals in Equations 2.1 and 2.2 are over the entire velocity-frequency-scalar space; Q represents any quantity (or correlation) whose mean or "expectation" is required; and the overbar in Equation 2.1 represents the Reynolds-averaged mean.

For variable-density reacting flows, it is more appropriate to consider the density-weighted pdf \tilde{f} or alternatively the mass density function (mdf) F defined by

$$\tilde{f}(\underline{V}, \eta, \underline{\psi}; \underline{x}, t) \equiv \rho(\underline{\psi}) f(\underline{V}, \eta, \underline{\psi}; \underline{x}, t) / \bar{\rho}, \quad (2.3)$$

and

$$F(\underline{V}, \eta, \underline{\psi}; \underline{x}, t) \equiv \rho(\underline{\psi}) f(\underline{V}, \eta, \underline{\psi}; \underline{x}, t) = \bar{\rho} \tilde{f}, \quad (2.4)$$

respectively, where $\bar{\rho}$ is the mean density. The density-weighted or Favre-averaged mean (denoted by angled brackets) of any quantity Q is given by:

$$\begin{aligned} \langle Q(\underline{U}, \omega, \underline{\phi}) \rangle &\equiv \overline{\rho Q} / \bar{\rho} \\ &= \iiint \rho(\underline{\psi}) Q(\underline{V}, \eta, \underline{\psi}) f(\underline{V}, \eta, \underline{\psi}) d\underline{V} d\eta d\underline{\psi} / \bar{\rho} \\ &= \iiint Q(\underline{V}, \eta, \underline{\psi}) \tilde{f}(\underline{V}, \eta, \underline{\psi}) d\underline{V} d\eta d\underline{\psi} \end{aligned}$$

$$= \iiint Q(\underline{V}, \eta, \psi) F(\underline{V}, \eta, \psi) d\underline{V} d\eta d\psi / \bar{\rho} . \quad (2.5)$$

(Note: The attributes \underline{x} and t are implied and not specifically stated for brevity.)

The pdf f represents the number probability density of events in the state space (velocity-frequency-scalar space) while the mdf F represents the probability density of the mass associated with the events.

2.2.1 The PDF Transport Equation

The transport equations for f , \tilde{f} or F can be derived starting from the familiar instantaneous conservation equations for mass, momentum, scalar (species, enthalpy, etc.) and a general model equation for the turbulence frequency. The conservation equations are listed below.

Continuity (instantaneous):

$$\frac{\partial \rho}{\partial t} + \frac{\partial(\rho U_i)}{\partial x_i} = 0 , \quad (2.6)$$

where $\rho(\Phi)$ is the instantaneous fluid density uniquely determined by the set of scalars Φ , and U_i is the instantaneous velocity in the i -th direction.

Momentum (instantaneous):

$$\frac{DU_j}{Dt} = -\frac{1}{\rho} \frac{\partial \bar{P}}{\partial x_j} + g_j + A_j , \quad (2.7)$$

where the material derivative (or the rate of change) following the fluid is

$$\frac{D}{Dt} = \frac{\partial}{\partial t} + U_k \frac{\partial}{\partial x_k} . \quad (2.8)$$

The first term on the right-hand side (of Eq. 2.7) represents the mean pressure gradient, g_j is the body force per unit mass in the j -th direction and

$$A_j = \frac{1}{\rho} \left(\frac{\partial \tau_{ij}}{\partial x_i} - \frac{\partial p'}{\partial x_j} \right) \quad (2.9)$$

represents the terms due to the sum of the viscous and viscous-diffusive stress tensor (τ_{ij}) and the fluctuating pressure gradient ($\partial p'/\partial x_j$). Note that the instantaneous pressure P has been decomposed into its mean and fluctuating parts while writing Eq. 2.7, i.e.

$$P = \bar{P} + p' . \quad (2.10)$$

Scalar conservation (instantaneous):

$$\frac{D\phi_\alpha}{Dt} = S_\alpha + \Theta_\alpha , \quad \alpha = 1, 2, \dots, \sigma , \quad (2.11)$$

where the number of scalars considered is σ , S_α is the rate of addition of scalar α (per unit mass of the fluid) due to reaction or other sources, and

$$\Theta_\alpha = -\frac{1}{\rho} \frac{\partial J_i^\alpha}{\partial x_i} , \quad (2.12)$$

where \underline{J}^α is the diffusive flux vector of species α . Note that the scalars could represent species mass fractions, enthalpy, conserved scalars such as mixture fraction, etc.

Turbulence frequency (instantaneous):

$$\frac{D\omega}{Dt} = \Lambda , \quad (2.13)$$

where Λ , which can be derived from the Navier-Stokes equation, describes the evolution of the turbulent frequency. The turbulence frequency is the inverse of the turbulence time scale τ and is defined by

$$\omega = \tau^{-1} = \varepsilon/k , \quad (2.14)$$

where k is the turbulent kinetic energy and ε is the rate of dissipation of k .

The molecular transport quantities τ_{ij} , and \underline{J}^α , and Λ are complicated functions of the local properties and their gradients.

The transport equation for the mdf, derived from the conservation equations 2.6, 2.7, 2.11, and 2.13 using simple techniques described in Ref. 2-7, is:

$$\begin{aligned} \frac{\partial F}{\partial t} + \underline{V}_j \frac{\partial F}{\partial x_j} + \left(g_j - \frac{1}{\rho(\underline{\Psi})} \frac{\partial \bar{P}}{\partial x_j} \right) \frac{\partial F}{\partial V_j} + \frac{\partial}{\partial \psi_\alpha} [S_\alpha(\underline{\Psi}) F] = \\ - \frac{\partial}{\partial V_j} [< A_j | \underline{V}, \eta, \underline{\Psi} > F] - \frac{\partial}{\partial \psi_\alpha} [< \Theta_\alpha | \underline{V}, \eta, \underline{\Psi} > F] - \frac{\partial}{\partial \eta} [< \Lambda | \underline{V}, \eta, \underline{\Psi} > F] . \end{aligned} \quad (2.15)$$

The terms on the left-hand side of the mdf transport equation represent, respectively, the time rate of change of the mdf, transport in physical space (convection), transport in velocity space by mean pressure gradient and body forces, and transport in scalar space due to reaction for example. All the terms on the left-hand side are known functions of the independent variables \underline{x} , t , \underline{V} , η , and $\underline{\Psi}$. Hence they are in closed form and need not be modeled. The terms on the right-hand side involve conditional expectations. For example, $< A_j | \underline{V}, \eta, \underline{\Psi} >$ is the conditional expectation of A_j given that $\underline{U} = \underline{V}$, $\omega = \eta$, and $\phi = \underline{\Psi}$. The conditional expectations involve the effects of viscous dissipation, molecular diffusion and the fluctuating pressure gradient. They are in general unknown and need to be modeled. It should be noted that these effects are modeled in the conventional methods as well. Hence there is no additional modeling burden created. In fact, the major modeling difficulties with the conventional methods are alleviated in the pdf method. The pdf method also allows a more sophisticated and detailed modeling of the molecular and fluctuating pressure gradient terms than conventional models.

2.2.2 Modeling and Solution of the PDF Transport Equation

The transport equation for the pdf (or the mdf) could in principle be solved using finite-volume methods. However, due to the large dimensionality of the pdf (a total of $7+\sigma$ independent variables including spatial coordinates, time, velocity and scalars) finite-volume methods are uneconomical since the computer requirements rise exponentially with the dimensionality of the pdf. Monte Carlo methods are most suited and economical for these computations. In the Monte Carlo method used, the flow field is simulated using a large number of computational particles

(representing fluid particles) whose evolution mimics the evolution of fluid particles. Hence a Lagrangian viewpoint is adopted in modeling and solving the mdm transport equation.

In the solution technique, notional particles representing fluid particles are distributed throughout the solution domain overlaid by a spatial or computational grid. Each particle represents a specified fluid mass and is attributed with values for its spatial position (\underline{x}^*), velocity (\underline{U}^*), scalar values (ϕ^*) and turbulence frequency (ω^*). These values evolve according to the equations described below which include modeled terms where needed. Starting from arbitrary initial conditions and specified boundary conditions, the particle values are marched in time-steps which are a fraction of a characteristic time scale in the flow until a steady-state solution is reached. As will be demonstrated below, the solution of these evolution equations constitutes the solution of the mdm transport equation. Means of any functions of the independent variables are determined by summing the values of the required properties over all the particles in each of the spatial bins or cells and fitting splines through these sums over the whole domain. More details can be obtained from Ref. 2-7 and other works listed in the Appendix.

The increment $d\underline{x}^*$ in the position of a particle over an infinitesimal time interval dt during the time step is given by the exact equation:

$$d\underline{x}^* = \underline{U}^* dt \quad . \quad (2.16)$$

This exact equation causes the mean and turbulent convection to be in closed form since the velocity used is the instantaneous velocity which includes the mean and fluctuation.

The general form for the increment in the particle velocity is

$$dU_i^* = - \frac{1}{\rho^*} \frac{\partial \bar{P}}{\partial x_i} dt + g_i dt + a_i dt \quad , \quad (2.17)$$

where $\rho^*(\phi^*)$ is the density of the particle, and \underline{a} represents the model for the effects of the viscous dissipation and fluctuating pressure gradient. In general, the model \underline{a} consists of both deterministic and random parts. The model \underline{a} is constructed such that it is determined by the current properties of the computational particles. In other words, \underline{a} is fully evaluated from the current mdm but includes a random component.

Similarly, the general forms of the increments in the scalar and frequency values of the particle over an infinitesimal time interval dt are:

$$d\phi_{\alpha}^* = S_{\alpha}(\phi^*) dt + \theta_{\alpha} dt, \quad (2.18)$$

and

$$d\omega^* = \lambda dt. \quad (2.19)$$

Again, the models $\underline{\theta}$ and λ could have deterministic and random parts and are constructed such that they are evaluated from the current mdf.

The transport equation of the mdf F (which is an Eulerian quantity by definition) can be derived from the Lagrangian particle evolution equations (2.16 through 2.19) using techniques presented in Ref 2-7. The resulting equation is:

$$\begin{aligned} \frac{\partial F}{\partial t} + V_j \frac{\partial F}{\partial x_j} + \left(g_j - \frac{1}{\rho(\underline{\Psi})} \frac{\partial \bar{P}}{\partial x_j} \right) \frac{\partial F}{\partial V_j} + \frac{\partial}{\partial \psi_{\alpha}} [S_{\alpha}(\underline{\Psi}) F] = \\ - \frac{\partial}{\partial V_j} [a_j | \underline{V}, \eta, \underline{\Psi} > F] - \frac{\partial}{\partial \psi_{\alpha}} [\theta_{\alpha} | \underline{V}, \eta, \underline{\Psi} > F] - \frac{\partial}{\partial \eta} [\lambda | \underline{V}, \eta, \underline{\Psi} > F]. \end{aligned} \quad (2.20)$$

A comparison of Eqs. 2.15 and 2.20 shows that the mdf of the computational particles (Eq. 2.20) evolves identically as the mdf of the fluid provided the corresponding conditional expectations (i.e., those of \underline{a} and \underline{A} , $\underline{\theta}$ and $\underline{\Theta}$, and λ and Λ) are equal. In other words, as long as the models are constructed such that "on the average" the computational particles behave the same way as the fluid particles, the solution of the evolution equations (2-16 through 2-19) is *statistically equivalent* to solving the mdf transport equation for the fluid and consequently the conservation equations for the fluid. Any turbulent correlation of any order extracted from the computed mdf will accurately reflect the correlations in the fluid even though the computational particles may behave differently from the fluid particle in microscopic detail.

Some of the models for \underline{a} and λ are described in the next chapter and the models for $\underline{\theta}$ are described in chapter 4. These models typically need information of the turbulence time scales. The motivation for including the turbulence frequency and the development of the joint velocity-frequency-scalar pdf method, is that the turbulence time scales are determined within the calculations.

2.3 Previous Work

A review of the development and application of the pdf method prior to the present program can be found in Refs. 2-7, 2-13 and 2-15. Although there had been some preliminary work with the velocity pdf in the late sixties by Lundgren and some scalar pdf work in the mid-seventies by Dopazo and O'Brien, and Pope, the development of the joint velocity-scalar pdf method was pioneered by Pope in the early eighties. Pope and coworkers, including Anand et. al., applied the joint pdf method to several simple reacting and nonreacting flows. The flows studied included homogeneous turbulence, self-similar jets, wakes, and mixing layer, the thermal wake, one-dimensional planar and spherical premixed flames, and diffusion flames. All these flows were either two-dimensional (2-D) parabolic or 1-D time-dependent flows. These fundamental studies contributed to the systematic and rigorous development of the pdf method, including its basic models and solution algorithms, and demonstrated the advantages (discussed in section 2.1) of the pdf method for computing turbulent reacting flows.

All previous work involved at most the sophistication of the joint velocity-scalar pdf method. A major drawback of the joint velocity-scalar pdf method, i.e., without the turbulence frequency, is that it does not contain any information on the time scales of the turbulent motions, needed for the models used in the calculations. However, given the time scale information, the method provides a complete description of the one-point joint velocity-scalar statistics throughout the flowfield. Previous studies discussed in the previous paragraph assumed either a uniform turbulence time scale across the flow that was estimated from mean flow properties or otherwise externally supplied the turbulence time scale to the pdf calculations. The assumption of a uniform time scale is not valid in general except in homogeneous turbulence or in specifically designed experiments. In fact, in most practical reacting and non-reacting flows the turbulence time scale varies significantly within the flow.

Hence a major thrust of the present study has been toward the development and validation of the joint velocity-frequency-scalar pdf method in which the turbulence frequency (inverse of the turbulence time scale, which is the primary quantity of interest) is also included as a random variable in the joint pdf. This causes the joint pdf equation and the calculations to be fully self-contained.

Another important issue in the joint pdf method is the calculation of the mean pressure gradient needed for solving the evolution equation for the particle velocities. Theoretically, there is no problem in determining the mean pressure gradients. Within every iteration or time-step in the calculations, the mean pressure field can be extracted from the pdf through the solution of the Poisson equation for pressure. However, a robust algorithm is needed to solve the Poisson

equation which involves the evaluation of second derivatives of mean velocities and other terms which are very sensitive to statistical errors inherent in the calculations.

For parabolic flows, the boundary-layer assumptions can be used to determine the transverse pressure gradient from the transverse momentum equation (see section 5.1). A pdf method for elliptic flows was first demonstrated by Anand et al. [2-15] for a 2-D flow. The method was subsequently applied to 3-D in-cylinder flows for spark ignition engines by Haworth and El Tahry [2-16, 2-17]. In this method, the Monte Carlo (MC) calculations for the pdf are combined with conventional finite-volume (FV) calculations [2-18] for the mean fields. The mean pressure field and the turbulence time scale are supplied to the MC calculations by the FV calculations. In turn, the MC calculations supply to the FV calculations the Reynolds stresses extracted from the pdf solution, thereby avoiding the use of conventional turbulence models. This combined algorithm exploits the advantages of both methods to yield an economical algorithm for pdf calculations of elliptic flows. This method was intended to demonstrate the feasibility of pdf calculations for such flows.

However, for more complex flows, especially variable density and reacting flows with fast or finite-rate multistep chemistry, the coupling between the two methods becomes quite complex and it becomes more difficult to fully exploit the advantages of the pdf method. Therefore, it is desirable to perform pdf calculations independently, without recourse to FV calculations. Hence, another major aspect of the present study is to develop and validate a robust and efficient algorithm for determining the mean pressure.

A third aspect of the present study that builds on the previous studies is the application of the pdf method to more complex flows of practical interest and validation against experimental data. As explained previously, the previous studies were involved with fundamental development of the pdf method and models and served to demonstrate the advantages of the pdf method. Understandably, the studies involved many simple and idealized flows. Results were compared with data from fundamental experiments and/or known behavior in flows such as homogeneous turbulence, decaying grid-generated turbulence self-similar flows and some simple flames. The method needed to be applied to and validated for more complex flows involving the essential features of gas turbine combustor flows such as swirl, recirculation and realistic multi-step chemistry, for the method to be developed as a gas turbine computer design tool.

2.4 Key Accomplishments under the Present Study

The objective of the present program was to perform the necessary model and algorithm development and validation to develop the pdf method as a combustor design and analysis tool. Consistent with the discussion in the previous subsection, two of the major aspects of the present study are the development of the joint velocity-frequency-scalar method, and the mean pressure algorithms for elliptic flows. Three variants of the frequency and velocity models and two variants of the pressure algorithm were developed and validated. A method for computing swirling flows with the boundary-layer algorithm was developed and validated. The validation of the models were performed for a wide variety of flows starting with fundamental flows for model development and preliminary validation as well as more complex gas-turbine-combustor-like flows for final validation. Available benchmark quality data were used where possible. However, due to incompleteness of data sets or lack of good quality data for flows of practical interest, benchmark quality experiments were designed in conjunction with WPAFB and the University of Dayton Research Institute (UDRI) personnel. The experiments were set up and performed by UDRI personnel at WPAFB.

The specific key accomplishments are:

- development of the model for mean turbulent frequency and validation for general inhomogeneous turbulent flows
- development of the treatment of swirl in the boundary-layer algorithm
- development of the stochastic models for turbulence frequency and the corresponding models for the velocity
- validation of the above for a variety of flows, including non-swirling and swirling, non-reacting and reacting flows, through comparison against benchmark quality data
- development and validation of the treatment near walls for wall bounded flows
- development and validation of the mean pressure algorithm for elliptic flows
- development of an improved mean pressure algorithm
- design of benchmark experiments. (The data are not specific to the pdf method. They can be used by the scientific community for validation of other models as well.)
- validation against backward-facing step flow and step-swirl methane combustor (swirling, recirculating and reacting flows)
- comparison of joint pdf calculations against calculations from scalar pdf and other conventional models (design system assessment performed under Allison IR&D program)
- publication of several papers. (A list of the papers is presented in the Appendix.)

The pdf model development and validation efforts have been very successful. The results of pdf calculations are in very good agreement with data for temperature and velocities (mean, variance and up to fourth order turbulent correlations). A baseline version of the joint pdf based combustor design system has been developed. Several enhancements to the design system have been identified and planned for the future to fully meet the requirements of the gas turbine combustor design system.

REFERENCES

- 2-1 W. P. Jones and B.E. Launder, "The Prediction of Laminarization with a Two-Equation Model of Turbulence," International Journal of Heat and Mass Transfer, **15**, 1972, pp 301-314.
- 2-2 W. Rodi, "Influence of Buoyancy and Rotation on Equations for the Turbulent Length Scale," Proceedings 2nd Symposium on Turbulent Shear Flows, London, 1979.
- 2-3 M. A. Leschziner and W. Rodi, "Computation of Strongly Swirling Axisymmetric Free Jets," Report SFB 80/T/216, University of Karlsruhe, April 1983, AIAA J., Vol 22, No. 12, 1984, pp 1742-1747.
- 2-4 W. Rodi and G. Scheurer, "Calculations of Curved Shear Layers with Two-Equation Turbulence Models," Physics of Fluids, **26**, 1983, pp 1422-1436.
- 2-5 B. E. Launder, E. J. Reece, and W. Rodi, "Progress in the Development of a Reynolds-Stress Turbulence Closure," J. Fluid Mechanics, **68**, 1975, pp 537-566.
- 2-6 P. A. Libby and F. A. Williams, "Turbulent Reacting Flows," Topics in Applied Physics **44**, Springer-Verlag New York, 1980.
- 2-7. S. B. Pope, "PDF Methods for Turbulent Reactive Flows," Progress in Energy and Combustion Science, **11**, 1985, pp 119-92.
- 2-8. R. S. Rogallo and P. A. Moin, Annual Review of Fluid Mechanics, **16**, 1986, pp 99-137.
- 2-9. A. T. Norris and A. T. Hsu, "Comparison of PDF and Moment Closure Methods in the Modeling of Turbulent Reacting Flows," AIAA Paper 94-3356, 1994.
- 2-10. P. A. Libby and K. N. C. Bray, "Counter-gradient Diffusion in Premixed Turbulent Flames," AIAA Journal, **19**, 1981, pp 205-213.
- 2-11. M. S. Anand and S. B. Pope, "Calculations of Premixed Turbulent Flames by PDF Methods," Combustion and Flame, **67**, No. 2, 1987.
- 2-12. G. M. Masuya and P. A. Libby, "Nongradient Theory for Oblique Turbulent Flames with Premixed Reactants," AIAA Journal, **19**, 1981, pp 1590-1599.

- 2-13. M. S. Anand, "PDF Calculations for Premixed Turbulent Flames," Ph.D. Thesis, Cornell University, Ithaca, New York, 1986.
- 2-14. P. A. Libby, "Theory of Normal Premixed Turbulent Flames Revisited," Progress in Energy and Combustion Science **11**, No. 1, 1985, pp 83-95.
- 2-15 M.S. Anand, S. B. Pope, and H. C. Mongia, "A PDF Method for Turbulent Recirculating Flows," U.S.-France Joint Workshop on Turbulent Reactive Flows, Rouen, France, 6-10 July 1987. Also in *Turbulent Reactive Flows*, Lecture Notes in Engineering, **40**, Springer-Verlag, pp 672-693, 1989.
- 2-16 D. C.Haworth, and S. H. El Tahry, "Application of PDF Method to In-Cylinder Flows in Reciprocating Engines," in Seventh Symposium on Turbulent Shear Flows, pp 13.1.1, Stanford University, 1989.
- 2-17 D. C. Haworth, and S. H. El Tahry, General Motors Research Laboratories, Report GMR-6844, 1989.
- 2-18 S. V. Patankar, *Numerical Heat Transfer and Fluid Flow*, Hemisphere, 1980.

3. MODELS FOR VELOCITY AND TURBULENCE FREQUENCY

This chapter describes the models developed and/or used in the present program, for velocity and turbulence frequency in the particle evolution equations (2.17 and 2.19 respectively). Three different models for turbulence frequency and the corresponding velocity models are described and discussed in the sections to follow.

3.1 Mean Frequency Model (MFM)

The mean frequency model was developed as a means for supplying the turbulence time scale to the joint velocity-scalar pdf calculations before the joint velocity-frequency-scalar pdf method was developed. In this model the randomness of the turbulence frequency ω is not accounted for; rather a transport equation for the mean turbulence frequency $\langle\omega\rangle$ is solved in conjunction with the pdf calculations to supply the time scale for the pdf calculations. Details of the development of the model are presented by Anand et al. [3-1].

The transport equation for $\langle\omega\rangle$ ($= k/\langle\epsilon\rangle$) is derived from the standard equations [3-2] for the turbulent kinetic energy k and the mean dissipation $\langle\epsilon\rangle$ with a simplification of the resulting diffusion terms:

$$\frac{\partial\langle\omega\rangle}{\partial t} + \langle U_i \rangle \frac{\partial\langle\omega\rangle}{\partial x_i} = C_1 S_{ij} S_{ij} - C_2 \langle\omega\rangle^2 + \frac{C_\mu}{\sigma_\omega} \frac{\partial}{\partial x_i} \left[\frac{k}{\langle\omega\rangle} \frac{\partial\langle\omega\rangle}{\partial x_i} \right], \quad (3.1)$$

where S_{ij} is the mean rate of the strain given by

$$S_{ij} = \frac{1}{2} \left(\frac{\partial\langle U_i \rangle}{\partial x_j} + \frac{\partial\langle U_j \rangle}{\partial x_i} \right), \quad (3.2)$$

and C_1 ($=0.1$), C_2 ($=0.88$), C_μ ($=0.09$) and σ_ω ($=1.0$) are constants. The values of the constants are derived from the standard values of the constants in the k and $\langle\epsilon\rangle$ equations. The left-hand side of Eq. 3.1 represents the transport of $\langle\omega\rangle$ by the mean flow. The terms on the right represent the production, dissipation and turbulent diffusion of $\langle\omega\rangle$ respectively. Eq. 3.1 is solved by finite differences using the mean velocity and kinetic energy fields extracted from the pdf solution. The mean frequency in turn is used in the models used in the pdf method. This

frequency model was used in conjunction with the boundary layer algorithm (section 5.1) and applied for the calculations presented in Chapters 6 and 7.

3.2 Simple Langevin Model I for Velocity using MFM (SLM I)

The velocity model used belongs to a class of stochastic models called the Langevin model. The models used here are a simplification of the generalized Langevin models used in some previous studies with the pdf method [3-3]. The simple Langevin model used by Anand and Pope [3-4] is considerably simpler to implement and sufficiently accurate for most of the flows under consideration.

The simple Langevin model for velocity corresponding to the mean frequency model (section 3.1) is:

$$dU_i^* = - \frac{1}{\rho^*} \frac{\partial \bar{P}}{\partial x_i} dt + g_i dt - \left(\frac{1}{2} + \frac{3}{4} C_o \right) (U_i^* - \langle U_i \rangle) \langle \omega \rangle dt + (C_o \langle \omega \rangle k)^{1/2} dW_i, \quad (3.3)$$

where C_o is a universal constant (due to Kolmogorov), and dW_i represents an isotropic Wiener random process with the properties that its mean and variance have the values $\langle dW_i \rangle = 0$ and $\langle dW_i dW_j \rangle = dt \delta_{ij}$. A comparison of Eq. 3.3 with Eq. 2.17 shows that the last two terms in Eq. 3.3 correspond to a_i in Eq. in 2.17 and collectively model the effects of viscous dissipation and fluctuating pressure gradients. The first of the two terms is a deterministic term, called the drift term since it tends to relax the particle velocity toward the mean velocity and reduce the velocity variance. The second of the two terms is a random term and models the return-to-isotropy phenomenon of turbulence. The constant C_o was determined by Anand and Pope [3-4] to have the value 2.1. As discussed in section 2.2.2 the first two terms on the right-hand side of Eq. 3.3 are exact and account for the effects of the mean pressure gradient and body forces without requiring modeling. Note that the first term contains the interaction between the instantaneous particle density and the mean pressure gradient. This is the reason that turbulence chemistry interaction phenomena such as counter-gradient diffusion and turbulence modulation due to reaction (see section 2.1.4) are automatically calculated in the joint pdf method.

3.3 Stochastic Frequency Model I (SFM I)

The stochastic frequency model provides the foundation for the joint velocity-frequency-scalar pdf method. The turbulence frequency is considered a random property in the calculations which

is consistent with the real situation. Indeed turbulent flow consists of a range of length and time scales. In addition, the model accounts for internal intermittency of turbulence, accounts for the effects of large scale turbulent structures, and better accounts for the origin and history of the fluid particles.

The stochastic frequency model was constructed with reference to known and computed (by direct numerical simulations [3-5]) properties of homogeneous turbulence. The model was then extended to inhomogeneous turbulence and validated against several self-similar flows. The model was then extensively exercised and validated for more complex practical flows. A brief description of the model is presented here. Details of the construction and validation of the model are presented in Refs. 3-6 through 3-9.

According to the model, the increment in the particle frequency over an infinitesimal time interval dt is given by

$$d\omega^* = \frac{\omega^*}{\langle \omega \rangle} C_{\omega 1} S_{ij} S_{ij} dt - \omega^* \langle \omega \rangle [C_{\omega 2} + C_{\chi} \Omega_{ln}] dt + \omega^* (2C_{\chi} \langle \omega \rangle \sigma^2)^{1/2} dW + \langle \omega \rangle^2 h dt, \quad (3.4)$$

where

$$\Omega_{ln} = \ln(\omega^*/\langle \omega \rangle) - \langle (\omega^*/\langle \omega \rangle) \ln(\omega^*/\langle \omega \rangle) \rangle, \quad (3.5)$$

and dW represents a Wiener random process. The constants in the equation (3.4) have the values $C_{\chi} = 1.6$ and $\sigma = 1.0$. The values $C_{\omega 1} = 0.04$ and $C_{\omega 2} = 0.70$ were found to result in the best agreement with data (see Chapter 7). The term involving the quantity h serves to entrain nonturbulent fluid in the intermittent region and is discussed in detail in Ref. 3-7. Additional comments regarding the role of the term are presented in Chapter 7. This model has been used for computing flows presented in Chapters 7 and 8.

3.4 Refined Langevin Model for Velocity using SFM I (RLM)

The velocity model corresponding to the SFM I model is referred to as the refined Langevin model since the use of instantaneous frequency (rather than the mean frequency) necessitates changes to the simple Langevin model (section 3.2) as described in Refs. 3-5 and 3-6. The model is given by

$$dU_i^* = -\frac{1}{\rho^*} \frac{\partial P}{\partial x_i} dt + g_i dt - \left(\frac{1}{2} + \frac{3}{4} C_0\right) (U_i^* - \langle U_i \rangle) \left(\frac{k'}{k}\right) \langle \omega \rangle dt + d_i dt + (C_0 \omega^* k')^{1/2} dW_i \quad (3.6)$$

The salient differences between the simple Langevin model SLM I (Eq. 3.3) and the refined model are that the random term contains the instantaneous frequency (rather than the mean), the ω -weighted mean kinetic energy k' is used, and there is an additional drift term d_i which is needed to account for the correlations between U and ω that result from random term. The additional drift term d_i is a complicated function of the Reynolds-stress tensor, its ω -weighted counterpart and k' , as discussed in Ref. 3-7. Due to these differences, the appropriate value of the constant for C_0 for this model is different from that in SLM I. The recommended value is $C_0 = 3.5$. This model is used for the computations reported in Chapters 7 and 8.

3.5 Stochastic Frequency Model II (SFM II)

The stochastic frequency model SFM II is a variation of the SFM I model and is the most recent model developed [3-10]. Compared to the previous stochastic frequency model SLM I (section 3.2), the new model is easier to implement and is expected to be more robust. Not only is the frequency model easier to implement and needs fewer computations, but also the corresponding velocity model is much simpler, easier to implement and expected to be more robust.

According to the SFM II model, the increment in the particle frequency over an infinitesimal time interval dt is given by

$$d\omega^* = \frac{\omega^*}{\langle \omega \rangle} C_{\omega 1} S_{ij} S_{ij} dt - \omega^* \langle \omega \rangle [C_{\omega 2} + C_3 \Omega_r] dt + \langle \omega \rangle (2C_3 \Omega_r \omega^* \sigma^2)^{1/2} dW + C_3 \Omega^2 dt \quad (3.7)$$

where

$$\Omega_r \equiv \Omega / \langle \omega \rangle \quad (3.9)$$

and

$$\Omega \equiv C_\Omega \langle \omega \mid \omega^* \geq \langle \omega \rangle \rangle \quad (3.10)$$

is the conditional mean frequency defined as an "above-average" mean, i.e. it is proportional to the mean of the instantaneous frequencies that are greater than or equal to the unconditional mean frequency. The constant C_Ω (determined in terms of incomplete gamma functions) has the value 0.6893, and is specified such that $\Omega = \langle \omega \rangle$ in homogeneous turbulence.

Although equations 3.4 and 3.7 are cast in the same general form, the basis for the derivation of the two models are very different, and the corresponding constants appearing in the equations have significantly different values. The SFM I model is based on a log-normal distribution for the pdf of frequency while the SFM II model is based on a Gamma distribution. The SFM II model was also constructed with reference to direct numerical simulation results [3-5]. By construction, the values of the constants σ^2 and C_3 are 0.25 and 1.0 respectively. The recommended values for $C_{\omega 1}$ and $C_{\omega 2}$ are 0.08 and 0.9 respectively.

A significant feature of the SFM II model is that it includes the conditional mean frequency which will be significantly higher than the unconditional mean in the intermittent region and avoids the inclusion of an ad hoc term as in the previous model to account for intermittency and entrainment of nonturbulent fluid. However, a drawback of the model compared to SFM II is that the conditional (mean) frequency, and not the instantaneous particle frequency, appears in the particle velocity equation corresponding to SFM II (see next subsection). This means that the full effect of all the turbulence time scales is not felt by the velocity equation.

It should be noted that both the SLM I and SLM II models performed equally well for the cases studied. Even though SFM II may be simpler to implement and more robust than SFM I, the latter is also computationally quite tractable. More studies will be required before a clear preference emerges.

3.6 Simple Langevin Model II for Velocity using SFM II (SLM II)

The model for the increment in the particle velocity, that corresponds to the SFM II model, is a variant of the simple Langevin model (SLM I) described in section 3.2. The SLM II model is described by:

$$dU_i^* = - \frac{1}{\rho^*} \frac{\partial \bar{P}}{\partial x_i} dt + g_i dt - \left(\frac{1}{2} + \frac{3}{4} C_o \right) (U_i^* - \langle U_i \rangle) \langle \omega \rangle dt + (C_o \langle \omega \rangle k)^{1/2} dW_i . \quad (3.3)$$

As explained before, the first two terms on the right exactly account for the acceleration due to mean pressure gradients (including variable-density effects) and body forces respectively. The

last two terms together model the effects of viscous dissipation and the fluctuating pressure gradient.

The main difference between the SLM II and SLM I models is that the conditional mean frequency Ω appears instead of the unconditional mean frequency $\langle\omega\rangle$. The consequences of this have been explained in the previous subsection. Also, the value of C_0 appropriate for the SLM II model is 2.5. The SFM II and the SLM II models have been used to compute the flows described in Chapter 10.

REFERENCES

- 3-1 M. S. Anand, S. B. Pope, and H. C. Mongia, "Calculations of Axisymmetric Turbulent Jets by the PDF Method," Seventh Symposium on Turbulent Shear Flows, Stanford University, 1989, pp 3.3.1-3.3.6.
- 3-2 B. E. Launder and D. B. Spalding, Computational Methods in Applied Mechanical Engineering, 3, 1974, pp 269-289.
- 3-3 D. C. Haworth and S. B. Pope, Physics of Fluids, 29, 1986, pp 387-405.
- 3-4 M. S. Anand and S. B. Pope, "Diffusion Behind a Line Source in Grid Turbulence," Turbulent Shear Flows 4, Eds. L.J.S. Bradbury et al., Springer Verlag, 1985, pp 46-61.
- 3-5 P. K. Young and S. B. Pope, Journal of Fluids Mechanics, 104, 1981, p 311.
- 3-6 S. B. Pope and Y. L. Chen, "The Velocity-Dissipation Probability Density Function Model for Turbulent Flows," Physics of Fluids A, 2, No. 8, 1990, pp 1437-1449.
- 3-7 S. B. Pope, "Application of the Velocity-Dissipation Probability Density Function Model to Inhomogeneous Turbulent Flows," Physics of Fluids A, 3, No. 8, 1991, pp 1947-1957.
- 3-8 M. S. Anand, S.B. Pope and H.C. Mongia (1993) "PDF Calculations for Swirling Flows," AIAA 93-0106. To be published AIAA Journal.
- 3-9 Anand, M.S., Takahashi, F. Vangsness, M.D., Durbin, M.D., and Schmoll, W.J., "An Experimental and Computational Study of Swirling Hydrogen Jet Diffusion Flames," ASME Paper 95-GT-307. To be published in the Transactions of the ASME.
- 3-10 Jayesh and S. B. Pope, " Stochastic Model for Turbulent Frequency," Report FDA 95-05, Cornell University, Ithaca, NY, 1995.

4. MODELS FOR MOLECULAR MIXING OF SCALARS

This chapter describes the models developed and/or used in the present program, for the molecular mixing of scalars in the particle evolution equations (i.e. the term involving θ in Eq. 2-18). Two different models for scalar mixing are described and discussed. One of the models, the improved mixing model, is a "particle interaction model" which means that the model is based on the direct interaction between the properties (or scalar values) of the individual particles that are in close proximity. The other is a relaxation to mean model, in which the individual particles interact with the local mean value of the scalar which is of course based directly on the properties of the other particles in the vicinity.

4.1 Improved Mixing Model (IMM)

The improved mixing model is a particle interaction model. It is a significantly more sophisticated and improved version of the well known Curl's model [4-1] and overcomes many of the undesirable features of the Curl's model. The model was developed by Pope [4-2] and has been used by the majority of joint pdf studies as well as for nearly all the flows in the present study. The model is described by the illustration given below.

Consider a general scalar variable ϕ . In the mixing model, pairs of particles, $N_p/2$ in number (a total of N_p particles), are picked by a random but sophisticated procedure described in Ref. 4-2. The number N_p is determined by

$$N_p = C_\phi N \langle \omega \rangle \Delta t , \quad (4.1)$$

where C_ϕ is a model constant usually in the range 1.5 to 2.0 (2.0 is used in the present study), N is the total number of particles in the computational cell, $\langle \omega \rangle$ is the mean turbulence frequency in the cell, and Δt is the interval of the computational time-step. Let p and q denote two particles of a pair. Their scalar values change from those at time t to those at time $t + \Delta t$ as follows:

$$\phi^p(t + \Delta t) = (1 - \xi) \phi^p(t) + \xi \phi_m , \quad (4.2)$$

and

$$\phi^q(t + \Delta t) = (1-\xi) \phi^q(t) + \xi \phi_m , \quad (4.3)$$

where

$$\phi_m = [\phi^p(t) + \phi^q(t)] / 2 \quad (4.4)$$

is the common mean value for the two particles and ξ is a random variable with the distribution $A(\xi) = 10 \xi^3 [1 - 3\xi/4]$. The value ξ ($0 < \xi < 1$) controls the extent of the mixing; with $\xi = 0$ no mixing occurs, with $\xi = 1$ maximum mixing occurs and both particles mix to their common mean ϕ_m .

Since the common mean ϕ_m is the same before and after the mixing process, the local mean scalar value $\langle \phi \rangle$ calculated as an ensemble average of all the particles in the cell (section 2.2.2) does not change due to mixing process. However, since the mixing process brings the two mixing particles closer to each other in the ϕ -space, the variance of the scalar $\langle \phi'^2 \rangle$ decreases. It can be shown that the effect of the mixing process on the scalar variance is

$$d\langle \phi'^2 \rangle / dt = - C_\phi \langle \omega \rangle \langle \phi'^2 \rangle . \quad (4.5)$$

Thus, the mixing model serves to dissipate the fluctuations in the scalar and is used to model the molecular dissipation process represented by the term $\underline{\theta}$ in Eq. 2-18.

4.2 Interaction by Exchange with the Mean (IEM) Model

This model was originally suggested by Dopazo [4-3]. It is a deterministic model (i.e. it does not involve any random numbers), and is only based on the scalar value of the particle and the mean scalar value at the particle location. The model for $\underline{\theta}$ is described by:

$$d\phi_\alpha^* = - C_\phi (\phi_\alpha^* - \langle \phi_\alpha \rangle) \langle \omega \rangle dt . \quad (4.6)$$

It can be seen that the model has the desired effect of moving the value of the particle composition towards the mean composition reducing the fluctuation in the scalar values. Indeed.

the variance of the scalars vary as in Eq. 4.5. The value of the constant for this model is in the range 1.0 to 1.5.

The model is very simple to implement. All the particles mix, and there is no need to develop an algorithm to pick the pairs of particles to mix. Also, for general variable-density flows additional care should be taken in the particle interaction models to ensure that the mixing is weighted appropriately to account for the differences in the masses of the mixing particles. But with the IEM model, the mass of the particle is not a consideration in carrying out the mixing process.

However, there are several drawbacks with the model. Since each particle changes a different amount towards the mean value (depending upon its own scalar value), there is no guarantee that the mean value $\langle \phi_\alpha \rangle$ remains unchanged after the mixing process. The mean is conserved in a statistical sense only when there are a large number of particles in the simulation. Also, if the profiles of $\langle \phi_\alpha \rangle$ have overshoots and undershoots (over and below their allowed values) due to the nature of the splines used for smoothing mean fields, the particles scalar values can also go out of bounds as a result of this mixing model. Another major deficiency is that since this model considers only the mean value, it is completely missing out the information of the pdf of composition contained in the ensemble of particles. For example, since it does not use the information on the evolving pdf, starting with an arbitrary initial pdf of scalars in a mixing problem in homogeneous turbulence, this model will not relax to a Gaussian pdf as expected. Nevertheless, due to its extreme simplicity and overall good performance for most flows with proper initial specification of the pdf, the utility of this model for complex multi-dimensional flows should not be overlooked. This model is used for the flows computed in Chapter 10.

REFERENCES

- 4-1. R. L. Curl, A.I.Ch.E Journal, **9**, 1963, p 175.
- 4-2. S. B. Pope, "An Improved Mixing Model," Combustion Science and Technology, **28**, 1982, pp 131-145.
- 4-3. C. Dopazo, Physics of Fluids, **18**, 1975, p 397.
- 4-4. S. B. Pope, "PDF Methods for Turbulent Reactive Flows," Progress in Energy and Combustion Science, **11**, p. 119, 1985.

5. ALGORITHMS TO DETERMINE MEAN PRESSURE

This chapter briefly describes the Monte Carlo solution algorithm and the algorithms for determining the mean pressure within the solution. Two types of algorithms are described. The first, boundary-layer algorithm, is applicable to one-dimensional (1-D) time-dependent or 2-D planar or 2-D axisymmetric flows without reverse-flows. The other class is the elliptic flow algorithm which is applicable to general 2-D and 3-D flows. It should be noted that the flow is 1-D, 2-D or 3-D only in the time-mean sense. In all the pdf calculations, all three components of physical space and all three components of velocity are considered in the computation of the particle motions and velocities. (Note: For the discussion presented in this chapter $\langle P \rangle$ and $\langle \rho \rangle$ refer to the mean pressure and mean density, respectively, which are Reynolds-averaged quantities. For all other variables, angled brackets $\langle \rangle$ indicate Favre-averaged quantities.)

5.1 Boundary Layer Algorithm

This algorithm is applicable to parabolic flows (1-D time-dependent or 2-D planar or axisymmetric flows without reverse-flow) such as jets, wakes, mixing layers, etc. The boundary layer assumptions can be used to calculate these flows. According to the assumption all axial gradients of mean quantities are assumed to be small compared to the transverse gradients and are neglected. The transverse pressure gradient is determined from the solution of the transverse mean momentum equation. However, in the present study involving swirling flows (without recirculation) the axial pressure gradient is not assumed zero. Instead it is calculated from the transverse (radial) pressure distribution as explained later in this section. A more detailed explanation of the material in this section can be found in Refs. 5-1 and 5-2.

For the discussions to follow, the notation $\underline{U} \equiv (U_1, U_2, U_3) \equiv (U, V, W) \equiv (\langle U \rangle + u, \langle V \rangle + v, \langle W \rangle + w)$ is used. In addition, due to the geometry of the flows considered, polar cylindrical coordinates (x, r, θ) are used. In the boundary-layer algorithm, the solution is marched downstream starting from initial conditions. The joint pdf at each step in the x-direction (the predominant flow direction) is represented by a large number, N , of computational particles. At the axial location x , each particle has the position $\underline{x}^*(x)$, velocity $\underline{U}^*(x)$, and the scalar value $\phi^*(x)$. In the general step from x to $x+\Delta x$, each particle evolves over at time interval Δt^* given by:

$$\Delta t^* = \Delta x / U_1^* \quad (5.1)$$

Note that all particles advance by the same Δx , but have different time intervals Δt^* . The increment to their velocities, frequency and scalar values are given by the corresponding evolution equations discussed in the previous two chapters.

The 2-D axisymmetric case applicable to swirling flows is considered. There are no theoretical limitations for computing swirling flows with the pdf method. Extensions were made to the boundary-layer algorithm to be able to compute swirling flows. The main extensions to the algorithm are to calculate and include the axial pressure gradient and to include all terms arising from the nonzero $\langle W \rangle$ field. The mean radial pressure gradient is computed from the mean radial momentum equation with the boundary-layer approximation that all the axial gradients are negligible. The azimuthal gradients are zero due to axisymmetry. The mean radial pressure gradient is given by:

$$\frac{1}{\langle \rho \rangle} \frac{\partial \langle P \rangle}{\partial r} = \frac{1}{r} \left(\langle W \rangle^2 + \langle w \rangle^2 - \langle v \rangle^2 - r \frac{\partial \langle v^2 \rangle}{\partial r} \right) . \quad (5.2)$$

The mean pressure, as a function of r at a given x , is given by

$$\langle P(r; x) \rangle = \langle P(R_o; x) \rangle - \int_r^{R_o} \frac{\partial \langle P \rangle}{\partial r} , \quad (5.3)$$

where R_o is the radius of the outer boundary of the jet. The mean axial pressure gradient at $x + \Delta x$, as a function of r , is then deduced by

$$\frac{\partial \langle P(r; x + \Delta x) \rangle}{\partial x} = \frac{\langle P(r; x + \Delta x) \rangle - \langle P(r; x) \rangle}{\Delta x} . \quad (5.4)$$

Any externally imposed axial pressure gradient can be incorporated through $\langle P(R_o; x) \rangle$ in Eq. 5.3. In the present study, $\langle P(R_o; x) \rangle$ is taken to be constant for all x . The axial pressure gradient is important in calculating the evolution of the mean axial velocity (especially its decay on the centerline) when appreciable swirl is present in the flow.

5.2 Mean Pressure Algorithm I for Elliptic Flows

The pressure algorithm is constructed for steady-state, constant- or variable-density, high Reynolds number flows. Details of the algorithm and its implementation can be found in Ref. 5-3. The equation for mean pressure is the Poisson equation (Eq. 5.6) derived from the mean momentum equation (Eq. 5.5):

$$\frac{\partial \langle \rho \rangle \langle U_i U_j \rangle}{\partial x_i} = - \frac{\partial \langle P \rangle}{\partial x_j}, \quad (5.5)$$

$$\frac{\partial^2 \langle P \rangle}{\partial x_j \partial x_j} = - \frac{\partial^2 \langle \rho \rangle \langle U_i U_j \rangle}{\partial x_i \partial x_j}. \quad (5.6)$$

Since the right-hand side of the equation can be evaluated from the pdf solution, Eq. 5.6 can be solved for the mean pressure $\langle P \rangle$ with appropriate boundary conditions. Starting from arbitrary initial conditions, if an iterative or pseudo-time marching algorithm is used to reach the steady-state for variable-density flows, then, because the transient terms are absent from Eq. 5.6, the mean pressure given by Eq. 5.6 is not correct until the steady-state is achieved. This is true even for the constant density cases unless the initial velocity field satisfies the continuity equation and Eq. 5.6 is solved in a coupled manner with the mean momentum equation which is not solved directly in the pdf method. A consequence is that the mean continuity equation

$$\frac{\partial \langle \rho \rangle \langle U_i \rangle}{\partial x_i} = 0 \quad (5.7)$$

will not be satisfied. Given a field that does not satisfy Eq. 5.7, a velocity correction $\Delta \underline{U}$ can be obtained by

$$\Delta U_i = \frac{1}{\langle \rho \rangle} \frac{\partial \Phi}{\partial x_i}. \quad (5.8)$$

By requiring that $\{\langle \rho \rangle \langle U_i \rangle + \langle \rho \rangle \Delta U_i\}$ be divergence free, we obtain a Poisson equation for Φ :

$$\frac{\partial^2 \Phi}{\partial x_j \partial x_j} = - \frac{\partial \langle \rho \rangle \langle U_i \rangle}{\partial x_i}. \quad (5.9)$$

These observations suggest the following basic algorithm: every so-many steps

1. solve Eq. 5.9 for Φ
2. add the velocity correction, Eq. 5.8
3. solve Eq. 5.6 for $\langle P \rangle$.

The spirit of the algorithm is similar to that of the SIMPLER algorithm used in conventional FV calculations [5-4]. However, the solution strategy and the implementation in the pdf calculations are markedly different. All mean quantities in the pdf method are calculated by forming ensemble averages and smoothing using some splining procedure. Since the Poisson equation for pressure involves second derivatives of mean quantities. It is necessary to evaluate the profiles of the means with very little statistical error. Typically, the splines used are cross-validated cubic B-splines [5-5] in order to obtain the required accuracy. But, they are quite expensive to form since the cross-validation and error reduction is an iterative procedure.

However, an efficient and economical procedure to solve the set of equations in the pressure algorithm has been developed. It utilizes the spline representation of the mean fields and exploits the fact that the resulting matrix equations for both $\langle P \rangle$ and Φ have the same form and the matrix on the left-hand side of the two equations is the same and constant through out the calculation. Hence the expensive matrix inversion is performed only once at the beginning of the calculations, and the equations for $\langle P \rangle$ and Φ are solved by the inexpensive back-substitution procedure on subsequent steps. Additional economies can also be realized by not solving these equations on every step but once in a few steps while allowing the mean velocity fields to change.

Although, this algorithm was successfully implemented and demonstrated for elliptic recirculating flows (see Chapter 9), it is felt that a more robust and economical algorithm will be needed for more complex 2-D and 3-D flows. Also it would be very cumbersome and difficult to fit cubic B-splines in irregular geometries and exploit the implementation algorithm described in the previous paragraph.

5.3 Mean Pressure Algorithm II for Elliptic Flows

The main purpose of the elliptic flow algorithm is to determine the mean pressure field to be used in the particle velocity equations (Chapter 3) while ensuring that the mean conservation

equations for mass and momentum are satisfied. The elliptic flow algorithm described in this section is an alternative to the one described in the previous subsection. In as much as the role of calculating the mean pressure is to ensure that the mean mass and momentum equations are satisfied, this algorithm does not attempt to directly solve the Poisson equation for the pressure but performs several corrections to the particle properties to ensure the same result. The algorithm performs a velocity correction to satisfy mean mass conservation and determines a mean pressure correction on every step starting from arbitrary initial conditions. Variance reduction techniques are applied so that mean momentum conservation is also maintained (i.e. turbulent processes such as mixing, viscous dissipation, etc. are performed on subensembles such that the subensemble means are not changed). In addition, a correction to the position of the particles is made to ensure that the consistency condition for particle methods, namely that the volume associated with a subensemble of particles should equal the geometric volume occupied by the particles, is satisfied. For statistically stationary flows, a steady state is achieved in which these corrections tend to zero (in the mean, and the variance decreases as the number of particles increases).

In the algorithm a velocity correction potential Φ is determined such that after adding the velocity correction

$$\Delta \underline{U} = \frac{1}{\langle \rho \rangle} \nabla \Phi, \quad (5.10)$$

(which is the same as Eq. 5.8), the corrected velocity field satisfies the continuity equation (Eq. 5.7). When the velocity increment is determined by Eq. 5.10 for a time step Δt , it is equivalent to the effect of a mean pressure correction

$$\Delta \langle P \rangle = - \Phi / \Delta t. \quad (5.11)$$

The Poisson equation for the velocity correction potential (same as Eq. 5.9) is set up and solved using bilinear basis function representation for calculating mean quantities [5-7]. Thus, the mean pressure field is not determined directly from the solution of the Poisson equation. However, any error in the mean pressure field is compensated by the velocity correction, i.e., the potential Φ is such the total effect of the correct pressure should be felt. Computations using this pressure algorithm have been successfully validated against data for nonreacting and reacting flows [5-8]. The results are presented in Chapters 9 and 10.

In contrast, the pressure algorithm developed and used by Anand et al. [5-3] solves for the Poisson equation for pressure as well as for the velocity correction potential. However, since the

Poisson equation involves second derivatives of mean velocities it is necessary to determine the mean velocity field to a high degree of accuracy. Hence, as discussed previously, bidirectional cross-validated cubic splines are used to determine means in that algorithm which can be computationally expensive. The current algorithm is expected to be less expensive and more robust. The more important advantage is that it is easier to extend the current algorithm to irregular geometries (body-fitted grids) and to three-dimensional flow calculations.

REFERENCES

- 5-1. S. B. Pope, "PDF Methods for Turbulent Reactive Flows," Progress in Energy and Combustion Science, **11**, p. 119, 1985.
- 5-2. M. S. Anand, S.B. Pope and H.C. Mongia, "PDF Calculations for Swirling Flows," AIAA 93-0106, 1993. To be published AIAA Journal.
- 5-3. M. S. Anand, S.B. Pope and H.C. Mongia (1990) "Pressure Algorithm for Elliptic Flow Calculations with the PDF method," CFD Symposium on Aeropropulsion, NASA CP-3078, 347-362.
- 5-4. S. V. Patankar, Numerical Heat Transfer and Fluid Flow, Hemisphere, 1980.
- 5-5. C. de Boor, A Practical Guide to Splines, Springer-Verlag, New York, 1978.
- 5-6. S. B. Pope, "Position, Velocity and Pressure Correction Algorithm for Particle Method Solution of the PDF Transport Equations," Report FDA 95-06, Cornell University, Ithaca, NY, 1995.
- 5-7. T. D. Dreeben and S. B. Pope, FDA 92-13, Cornell University, Ithaca, NY, 1992.
- 5-8. M. S. Anand, A. T. Hsu, and S. B. Pope, "PDF Calculations for Swirl Combustors," AIAA Paper 96-0522, 1996. Submitted to AIAA Journal.

6. COAXIAL JET FLOWS

6.1 Overview

The pdf method is applied to calculate the flow field of two concentric jets issuing into stagnant surroundings. The main objective of this study was to validate the pdf method using the mean frequency model (MFM) and the simple Langevin model (SLM I) for general inhomogeneous flows. A modeled transport equation for the mean turbulence frequency is solved, in contrast to previous studies with the pdf method that assumed the frequency to be constant across the flow. This results in a significant improvement in the agreement of the model predictions with experimental data of McDonnell et al. [6-1]. Other aspects of the modeling are investigated, including the modeling of intermittency, the effect of the universal constant in the Langevin model for velocities, and the assumption of a coflow for the simulation. The study is reported in detail by Anand et al. [6-2]

6.2 Background

A local turbulent time scale, τ , or its inverse, the turbulent frequency, $\langle\omega\rangle$, is needed for the models use in the pdf method. For the study of recirculating flows (Anand et al. 1987), the turbulent frequency was supplied to the pdf calculations from the accompanying conventional finite-volume calculations. In all other studies with the pdf method, the turbulent frequency was assumed to be constant across the flow. The assumption of a uniform $\langle\omega\rangle$ is valid by definition for the homogeneous turbulence cases [6-4, 6-5]. For the self-similar free shear flows [6-6, 6-7] the turbulence frequency was assumed based on self-similarity to be proportional to the inverse of the mean-flow time scale. The same assumption was used for calculating the $\langle\omega\rangle$ in the studies of jet diffusion flames [6-8, 6-9] where the emphasis was more on the chemical modeling aspects than on the velocity fields. The assumption of a uniform $\langle\omega\rangle$ is perhaps reasonable in the self-similar regime and in the region far downstream of the inlet for the free shear flows studied previously. However, the effect of a uniform $\langle\omega\rangle$ on the pdf calculation in the developing (non-self-similar) region close to the inlet or for other inhomogeneous flows need to be investigated.

6.3 Modeling Considerations

The boundary layer algorithm (section 5.1) is used since the flow is parabolic in nature. The mean frequency model (MFM) (section 3.1) is used for the frequency and simple Langevin model (SLM I) is used for the velocities. Calculations were also made with the assumption of uniform $\langle\omega\rangle$ for comparison.

In the boundary-layer algorithm (see section 5.1), modeled particles representing fluid particles are marched downstream based on their axial velocities. It is therefore necessary that the axial velocities be always positive. Hence, a coflow stream with a small positive axial velocity surrounding the jets is assumed for the simulations, although the jets issue into stagnant surroundings in the experiments. The effect of this assumed coflow is also investigated.

Other aspects of the modeling that are investigated in the present study are the modeling of intermittency and the effect of the universal constant in the Langevin model for the velocities.

6.3.1 Intermittency

The phenomenon of intermittency, which results from nonturbulent fluid surrounding the turbulent flow under consideration, is accounted for by conditional modeling based on a passive scalar ϕ^* [6-6, 6-8]. The value $\phi^*>0$ represents turbulent fluid and $\phi^*=0$ denotes nonturbulent fluid. Within the turbulent fluid, the ϕ^* value of a particle evolves by molecular mixing, which is modeled by the IMM model (section 4.1).

In the intermittency model, nonturbulent fluid is entrained (i.e., becomes turbulent) at a specific rate. The nonturbulent fluid exchanges momentum and energy with the turbulent fluid. The model involves three constants: C_g ($=2.0$) controls the rate of entrainment; C_m ($=1.5$) and C_e ($=5.0$) control the rate of momentum and energy transfer, respectively. Haworth and Pope [6-6] concluded that although the intermittency model works reasonably well in conjunction with particle interaction models for velocity (not used here), it is not entirely satisfactory in conjunction with the Langevin model which is the preferred model. In the present study, calculations are performed both with and without the intermittency model.

6.3.2 Calculations with Uniform $\langle\omega\rangle$

For the calculations in the present study for which $\langle\omega\rangle$ is assumed constant in the r-direction, the last term (diffusion term) in Eq. 3.1 is zero by assumption. The rest of the terms in the equation

are weighted by the local turbulent kinetic energy and integrated over the cross-sectional area of the flow to obtain an integral estimate for the value of $\langle \omega \rangle$.

6.4 Flow Description and Computational Details

The flow studied is of two concentric nonswirling jets issuing into stagnant surroundings. Detailed experimental data for the flow, including mean velocities and turbulent normal and shear stresses, are reported in Ref. 6-1. The central air jet of diameter D (24.1 mm) is surrounded by an annular air jet with inner and outer diameters of 29 mm and 36.7 mm, respectively. The average axial velocity in the central jet is 4.67 m/s and that in the annular jet is 6.6 m/s. The Reynolds number of the central jet (based on D) is approximately 6100.

Initial conditions for the computations are prescribed from experimental data. Due to the wall thickness of 2.5 mm between the central and annular jets, a reverse flow region is indicated by the data at $x/D=0.08$ from the nozzle exit. Hence, the next axial measurement station at $x/D=0.62$ is taken as the initial plane for the calculations.

In this and the next section, the following notation is used: $\langle U \rangle$ is the mean axial velocity; u , v , and w are the fluctuating velocities in the axial, radial, and azimuthal directions. The reference velocity used for normalization ($U_{0,c} = 4.28$ m/s) is the mean axial velocity on the centerline at the initial station. The radial distance, r , is normalized by the central jet radius, $R (=D/2)$.

The initial velocity pdf is prescribed to be joint normal with the mean and covariances taken from linearly interpolated experimental data available (see Figure 6-1). Two sets of experimental data available for $\langle U \rangle$ and $\langle u^2 \rangle$ give an indication of the scatter in the data. The nominal number of particles used for the computations is 23,000. A coflowing stream of mean axial velocity $U_b=0.4$ m/s is assumed. With the initial peak mean axial velocity being approximately 6 m/s, the velocity ratio (low speed to high speed) is 0.066.

The initial values of $\langle \omega \rangle$ are derived from experimental data based on

$$\langle \omega \rangle = - C_\mu \frac{k}{\langle uv \rangle} \frac{\partial \langle U \rangle}{\partial r} \quad (6.1)$$

which follows from the k - ϵ model assumptions. The experimental data for k , $\langle uv \rangle$, and $\langle U \rangle$ are smoothed using B-splines to evaluate Eq. 6.1.

The initial profile of $\langle\omega\rangle$ from Eq. 6.1, the integrated uniform value estimated, and the initial profile of $\langle\phi\rangle$ are shown in Figure 6-2.

The initial pdf of ϕ was taken to be a double-delta function of magnitude $\langle\phi\rangle$ at $\psi=1.0$ and magnitude $(1-\langle\phi\rangle)$ at $\psi=0$. Hence, initially, the profile of $\langle\phi\rangle$ corresponds to the profile of the intermittency factor γ , which is defined as the probability of the fluid being turbulent. The profile of $\langle\phi\rangle$ is specified to vary smoothly from $\langle\phi\rangle=1$ to $\langle\phi\rangle=0$ in the region where the kinetic energy profile drops in the outer shear region of the annular jet.

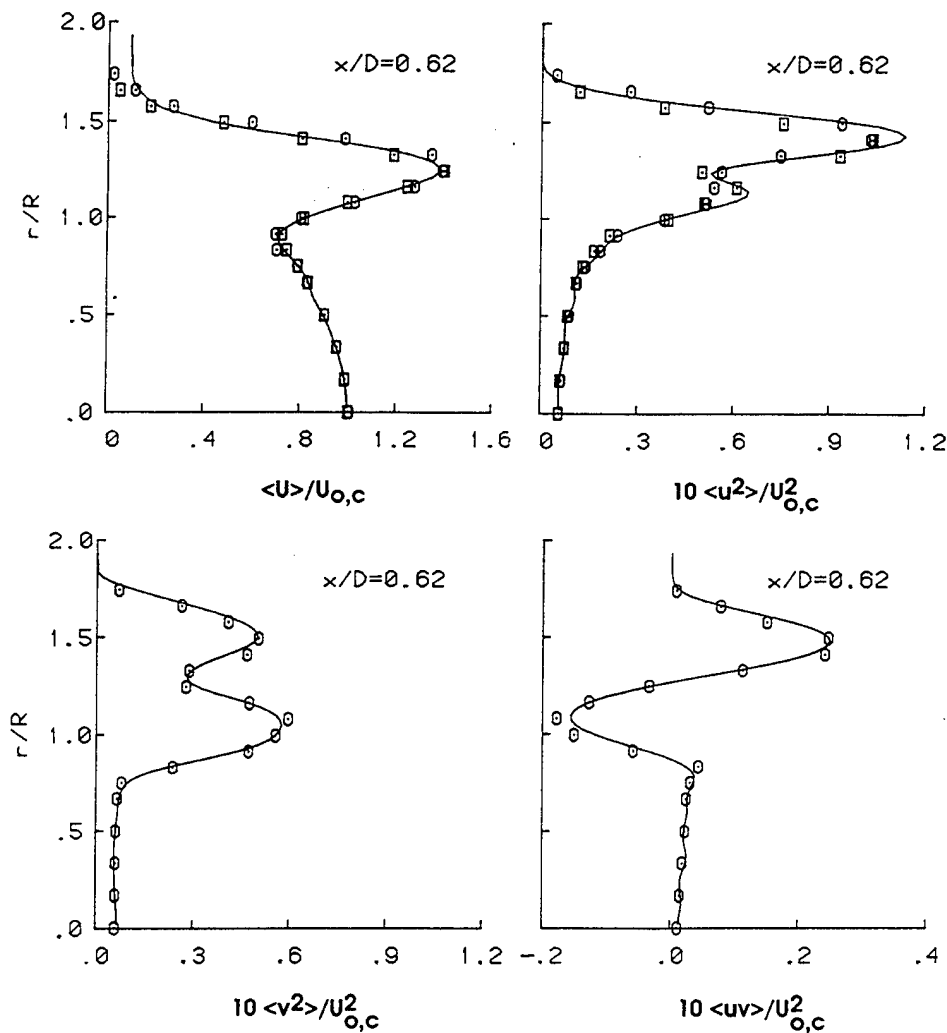


Figure 6-1. Initial conditions for normalized mean axial velocity and Reynolds stresses. Symbols represent experimental data; solid lines are calculated from initial pdf. $\langle w^2 \rangle$ is similar to $\langle v^2 \rangle$.

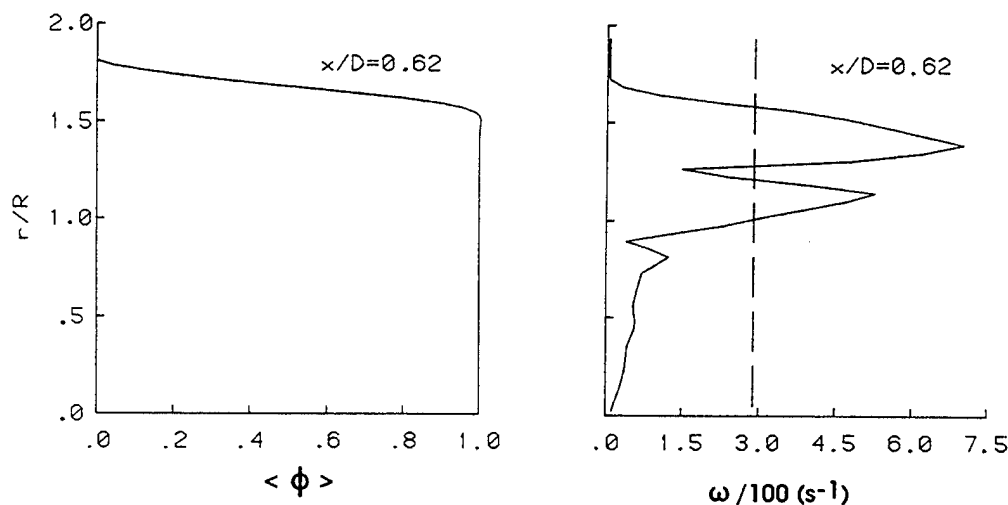


Figure 6-2. Initial profiles of turbulence frequency $\langle \omega \rangle$ and mean of the conserved scalar $\langle \phi \rangle$.

6.5 Results and Discussion

Limited results are presented first for three cases with variations in the modeling used. Case A includes modeling of intermittency and the assumption of a uniform $\langle \omega \rangle$. For Case B, intermittency is not modeled (i.e., the entire flow is assumed turbulent), but $\langle \omega \rangle$ is assumed to be uniform. For Case C, intermittency is not modeled, and $\langle \omega \rangle$ is nonuniform (MFM model).

Results for the mean axial velocity, turbulent kinetic energy, and shear stress for the three cases are shown in Figure 6-3 at two axial stations. Overall, Case C has the best agreement with data, while Case A has the worst. The difference between modeling (A) and not modeling intermittency (B) affects the peak and outer-edge values of turbulent stresses. However, the jet spreading rate for both cases is smaller compared with data, although not modeling intermittency (B) improves the spreading rate and peak values of turbulent stresses.

A more significant improvement in the results is seen when $\langle \omega \rangle$ is assumed to be nonuniform (C). The mean axial velocity profile spreads more in accordance with the data, while the magnitude of turbulent kinetic energy has increased in the central and outer regions of the jet.

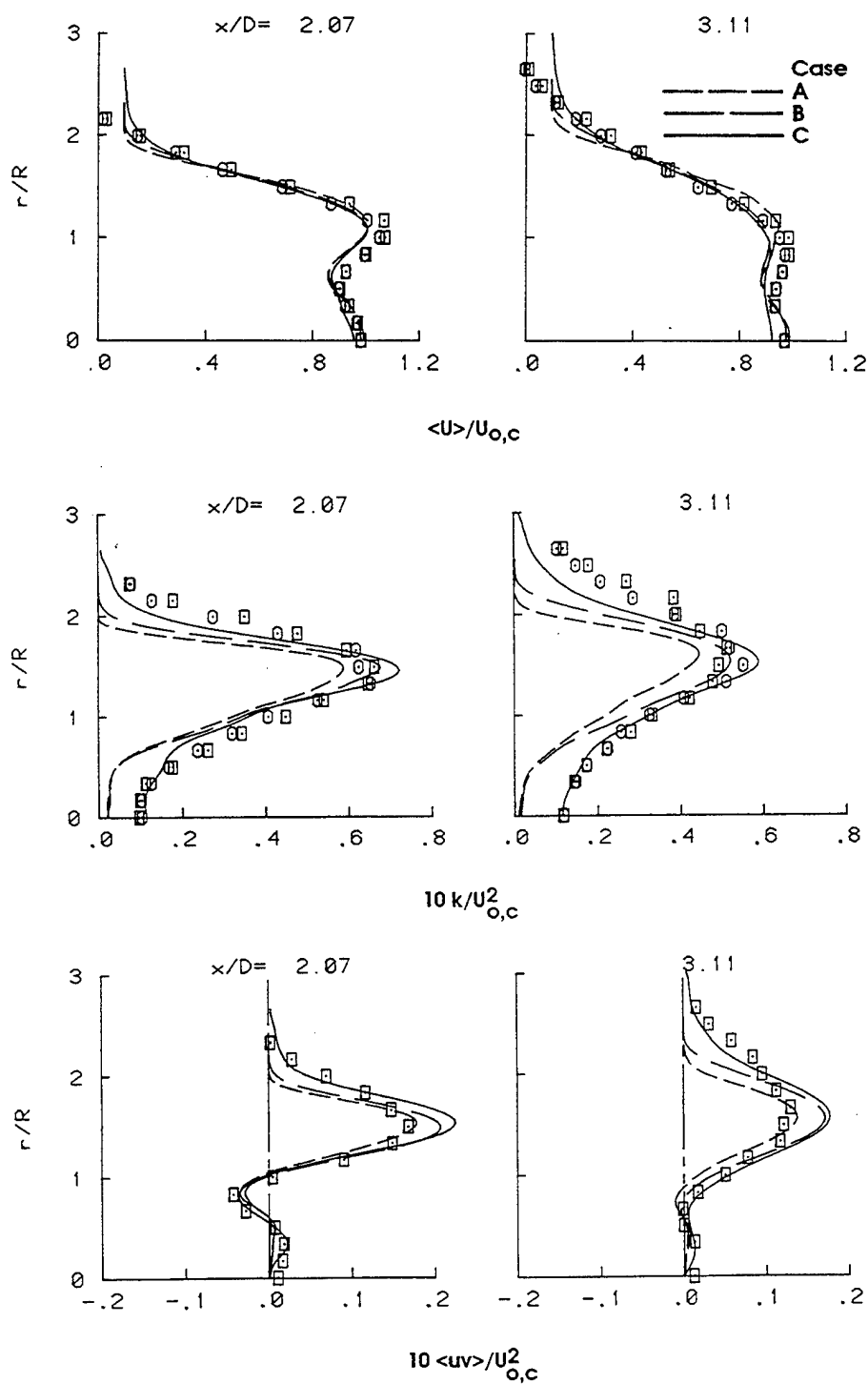


Figure 6-3. Comparison of results for cases (A) with conditional modeling and uniform $\langle \omega \rangle$, (B) without conditional modeling and uniform $\langle \omega \rangle$, and (C) without conditional modeling and nonuniform $\langle \omega \rangle$, at two axial stations. Symbols represent experimental data.

This is because a higher value of $\langle \omega \rangle$ for Cases A and B than for Case C in these regions (Figures 6-2 and 6-6) implies a higher ratio of dissipation to kinetic energy for the former cases.

Based on these results, the modeling strategy adopted for the rest of the study is to solve the full transport equation for $\langle \omega \rangle$ and not to use conditional modeling as in Case C. Detailed results for Case C and comparison with data are presented in Figures 6-4 and 6-5 at various axial stations up to $x/D=12.4$ (Results and data for $\langle w^2 \rangle$ are qualitatively and quantitatively similar to those for $\langle v^2 \rangle$.) The computed results are generally in good agreement with data. The calculated mean

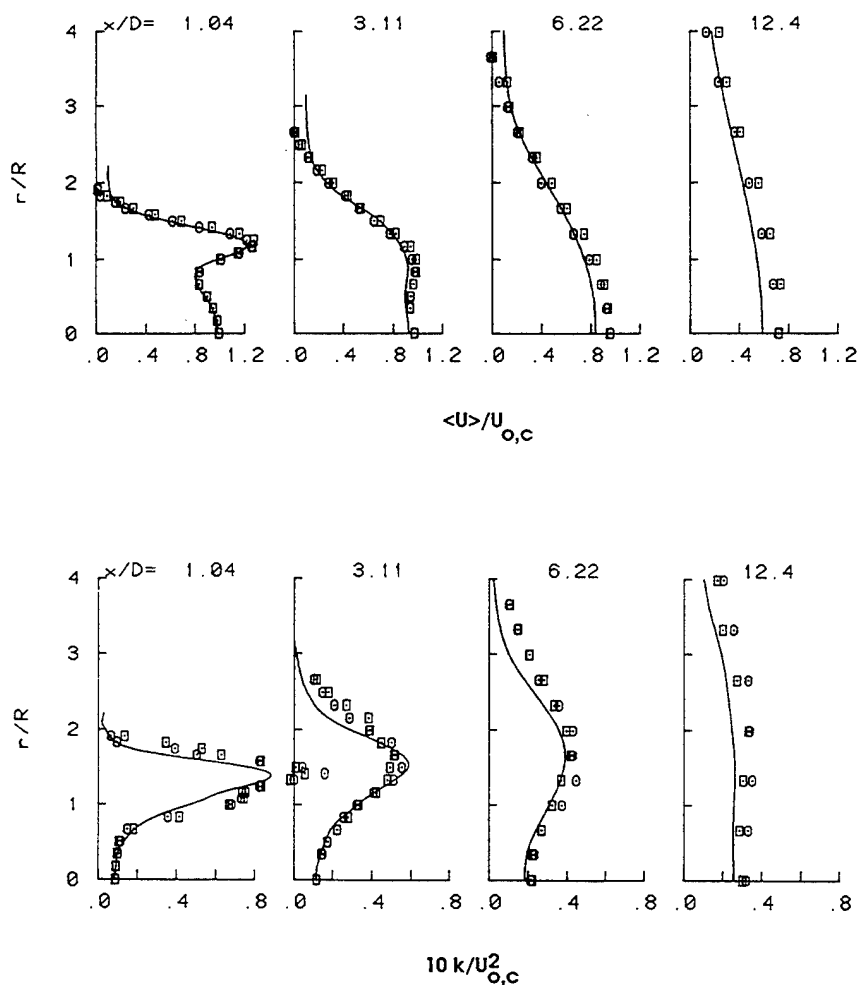


Figure 6-4. Computed (Case C) radial profiles of normalized mean axial velocity and turbulent kinetic energy compared against experimental data at various axial stations.

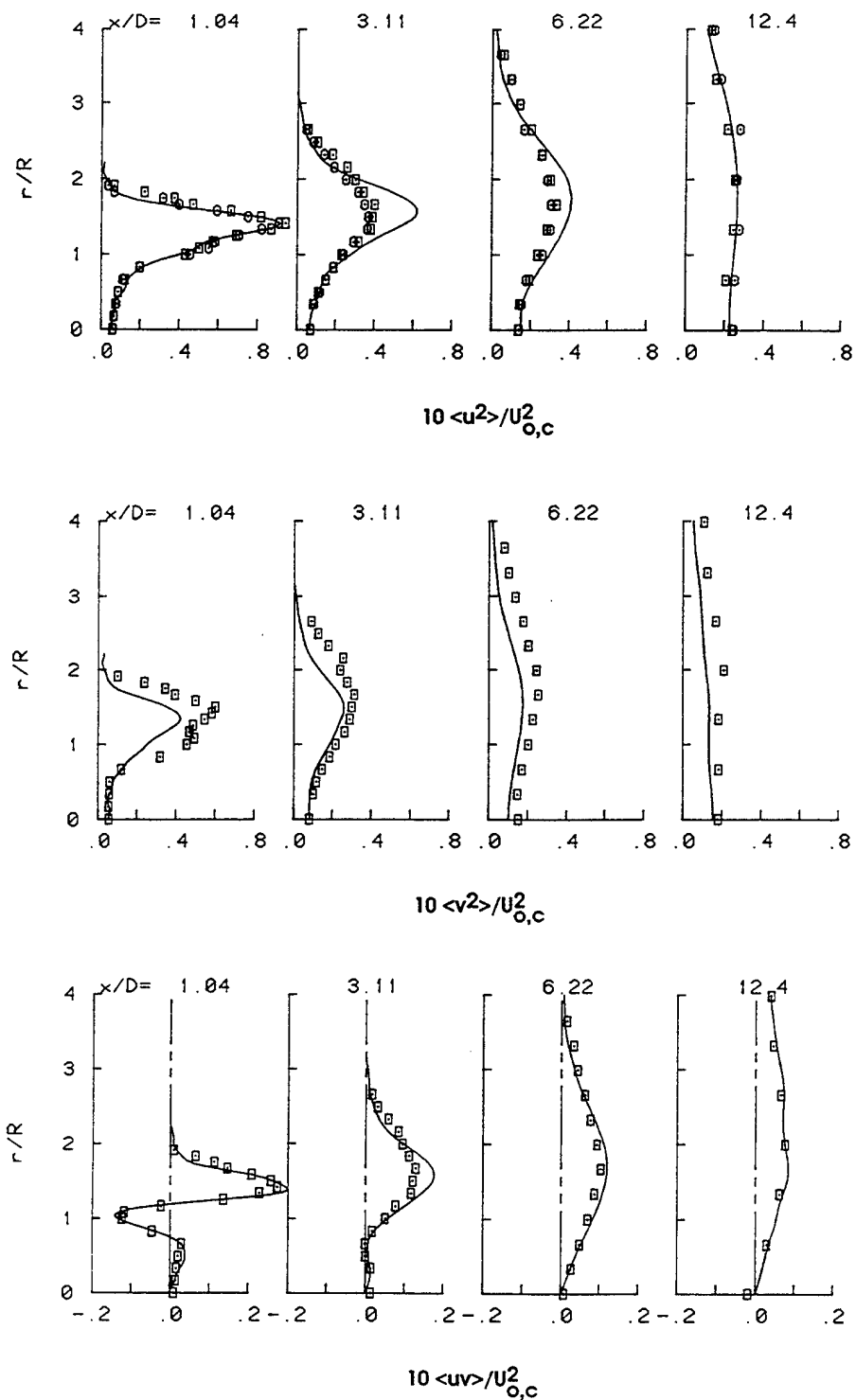


Figure 6-5. Computed (Case C) radial profiles of normalized Reynolds stresses compared against experimental data at various axial stations.

axial velocity profiles and the spreading of the jet are well predicted, although the mean axial velocity in the central region of the jet decays slightly faster than indicated by the data. The shear stress profiles are in good agreement with the data. Results from normal stresses are discussed later in this section.

The calculated profiles of $\langle \omega \rangle$ for Case C are shown in Figure 6-6. The peak value of $\langle \omega \rangle$ drops dramatically from about 700 s^{-1} at a location less than half a diameter downstream ($x/D=1.04$, Figure 6-6). The $\langle \omega \rangle$ profile becomes progressively flatter and lower in magnitude further downstream.

The effect of the value of σ_ω in the MFM model (Eq. 3.1) is now investigated. Also shown in Figure 6-6 are $\langle \omega \rangle$ profiles with $\sigma_\omega=0.7$ and $\sigma_\omega=1.3$, as well as the values of uniform $\langle \omega \rangle$ calculated in Case B. Over most of the radius, the calculated uniform values of $\langle \omega \rangle$ are much higher than those calculated in Case C. It is also apparent that the value of σ_ω has little effect on the results. This indicates that the diffusion term in the $\langle \omega \rangle$ -equation (Eq. 7) is small compared to the other terms in the equation for the flow being studied. The improvement in the results for Case C over Case B comes not from just including the diffusion terms, but more due to the fact that a local value of $\langle \omega \rangle$ is calculated rather than using a uniform integral value.

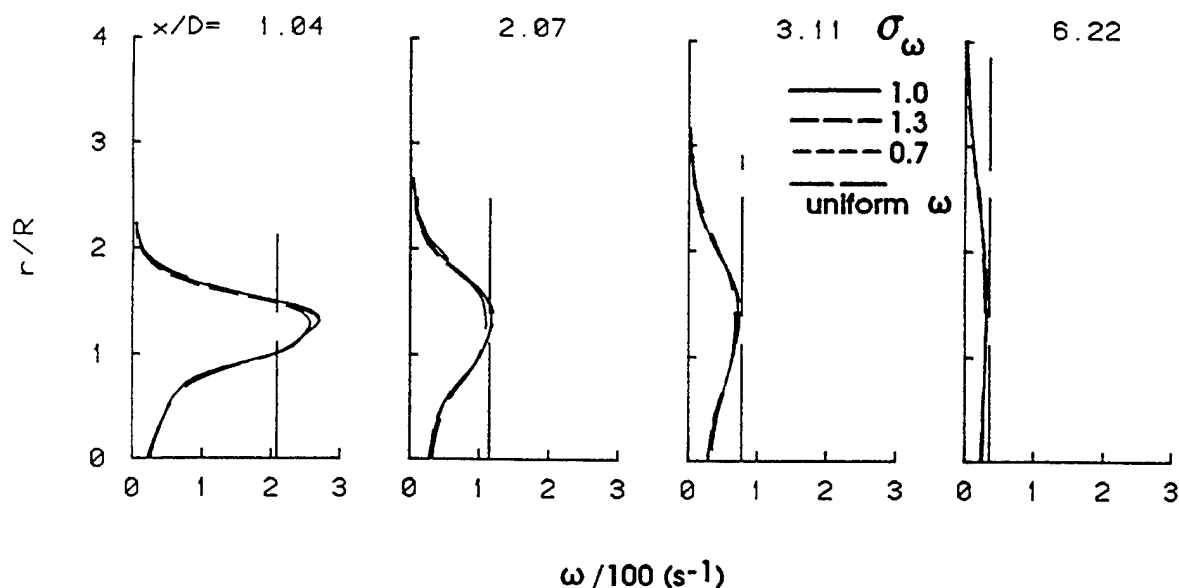


Figure 6-6. Computed radial profiles of $\langle \omega \rangle$ for Case C ($\sigma_\omega = 1.0$), Case B (uniform $\langle \omega \rangle$), and the two other values of σ_ω compared at different axial stations.

A discussion of the calculated kinetic energy and velocity variances is now presented. Figures 6-4 and 6-5 show that while the k profiles are in good agreement with the data, $\langle u^2 \rangle$ is overestimated, while $\langle v^2 \rangle$ (and $\langle w^2 \rangle$) are underestimated, especially at the near-inlet stations. Since the redistribution of k is influenced by C_0 , calculations were performed with different values of C_0 in the range 2.1 to 3.5. A larger value of C_0 is expected to increase, as one of its effects, the tendency towards isotropy of normal stresses. Results show that as C_0 is increased up to 3.0, the agreement of $\langle u^2 \rangle$, $\langle v^2 \rangle$, and $\langle w^2 \rangle$ with data does not improve up to $x/D=3.11$. At $x/D=6.11$ and beyond, the results are independent of C_0 . Also the results at all x/D are nearly identical for $C_0=3.0$ and $C_0=3.5$. Overall, the effect of varying C_0 is not significant enough to warrant a revision of the value $C_0=2.1$ used in this and previous studies. It should be mentioned that the more complicated generalized Langevin model [6-5], which explicitly incorporates Reynolds stresses and mean velocity gradients in the model, may be more accurate in calculating the relative magnitudes of the normal stresses than the simplified model used here.

Lastly, the effect of the assumed coflow is investigated. Figure 6-7 shows the mean axial velocity profiles for three cases with values of U_b equal to 0.4, 0.6, and 0.8 m/s. It is seen that the velocity profiles are nearly identical except near the edge of the flow. The value of U_b had no significant effects on the turbulent stresses. Thus, over the domain of interest in the present flow, the value of U_b has little effect on the computed results.

The improvement in the results seen with nonuniform $\langle \omega \rangle$ in the present study can be viewed from another perspective. With similar modeling but uniform $\langle \omega \rangle$, Haworth and Pope [6-7] found that the boundary-layer algorithm was increasingly inaccurate and the spreading rates were significantly underestimated for values of the low-speed to the high-speed velocity ratio less than 0.3. The results in the present study with a velocity ratio of 0.066 indicate that the range of applicability, in terms of the velocity ratio, is extended for the boundary-layer algorithm when the local value of $\langle \omega \rangle$ is used instead of an integral value.

An additional advantage derived in solving for nonuniform $\langle \omega \rangle$ has to do with the computational time required. The distance that the solution can be marched on each step (Δx) is determined primarily by the local turbulent time scale. The average Δt^* for particles is limited to a fraction of the local value of τ (or $1/\langle \omega \rangle$). From Eq. 1, it can then be seen that Δx is proportional to the minimum value of $\langle U \rangle / \langle \omega \rangle$. For the cases in the present study with nonuniform $\langle \omega \rangle$, regions of low $\langle U \rangle$ have low values of $\langle \omega \rangle$ also, while for the uniform cases,

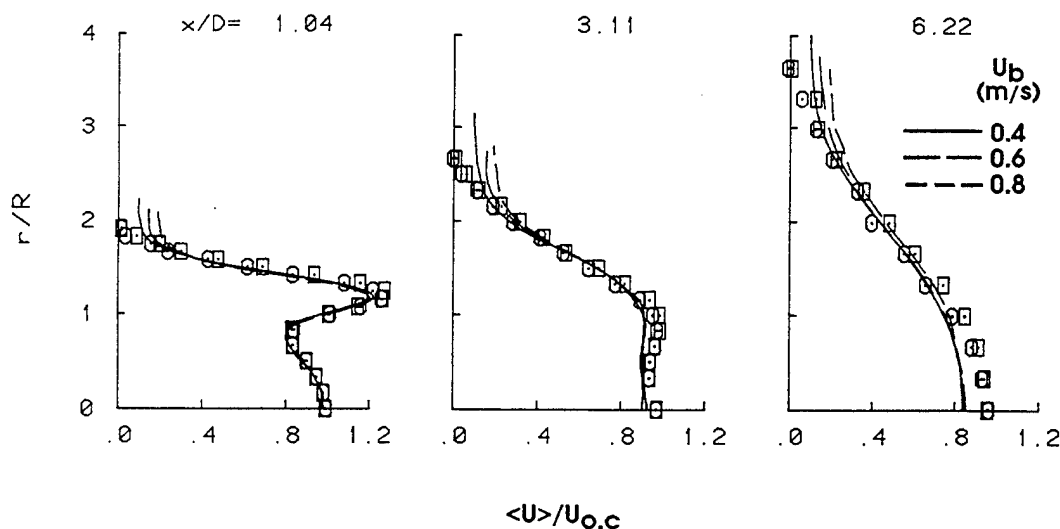


Figure 6-7. Mean axial velocity profiles from calculations with three different values of coflow velocity U_b .

the value of $\langle \omega \rangle$ is significantly higher in these regions. Hence, the allowable Δx for each step is lower for the uniform- $\langle \omega \rangle$ cases than for the nonuniform cases. The computations were performed on an AMDAHL 5890 mainframe. For the nonuniform $\langle \omega \rangle$ cases, 330 steps (5.8 min of CPU time) are typically needed for the calculations from $x/D=0.62$ to $x/D=12.4$. The cases with uniform $\langle \omega \rangle$ required nearly 60% more steps and CPU time.

6.6 Summarizing Remarks

A detailed modeling study of coaxial jets issuing into stagnant surroundings is reported. A modeled transport equation for the turbulence frequency ($\langle \omega \rangle$) is proposed and solved to obtain the local turbulent time scale. The results of these calculations are in better agreement with the data than with the assumption of a uniform $\langle \omega \rangle$ across the flow. The former calculations also require significantly less computational time than the latter to advance the solution by the same axial distance. The simplified Langevin model with the value of the Kolmogorov constant $C_0=2.1$ was found to be satisfactory, although increasing C_0 produced better results in a limited

sense. The modeling of intermittency was found to be deficient. The assumed coflow needed for the simulations had little effect on the results.

Some of the modeling issues raised in the present study will be addressed by the new velocity-frequency models described in sections 3-3 through 3-6. With these models, the turbulent frequency is also considered a random variable similar to the velocities and is solved as a part of the pdf solution. Calculations using these models are described in the following chapters.

REFERENCES

- 6-1. V. G. McDonnel, C. P. Wood, and G. S. Samuelsen, Combustion Laboratory Report ARTR 87-1, Dept. Mech. Eng., University of California, Irvine, 1987.
- 6-2. M. S. Anand, S.B. Pope and H.C. Mongia (1989) "Calculations of Axisymmetric Turbulent Jets by the PDF Method," Seventh Symposium on Turbulent Shear Flows, Stanford University, Stanford, pp. 3.3.1-3.3.6.
- 6-3. M. S. Anand, S. B. Pope, and H. C. Mongia, "A PDF Method for Turbulent Recirculating Flows," U.S.-France Joint Workshop on Turbulent Reactive Flows, Rouen, France, 6-10 July 1987. Also in *Turbulent Reactive Flows*, Lecture Notes in Engineering, **40**, Springer-Verlag, pp 672-693, 1989.
- 6-4. M. S. Anand and S. B. Pope, "Diffusion Behind a Line Source in Grid Turbulence," Turbulent Shear Flows 4, Eds. L.J.S. Bradbury et al., Springer Verlag, 1985, pp. 46-61.
- 6-5. D. C. Haworth, and S. B. Pope, Physics of Fluids, **29**, 1986, pp 387-405.
- 6-6. D. C. Haworth, and S. B. Pope, Physics of Fluids. Fluids, **30**, 1987, pp 1026-1044.
- 6-7. D. C. Haworth, and S. B. Pope, Journal of Computational Physics, **72**, No. 2, 1987, pp. 311-346.
- 6-8. D. C. Haworth, M. C. Drake, R. J. Blint and S. B. Pope, Twenty-Second Symposium (International) on Combustion, The Combustion Institute, Pittsburg, 1989.
- 6-9. S. B. Pope and S. M. Correa, Twenty-Second Symposium (International) on Combustion, The Combustion Institute, Pittsburg, 1989.

7. CONSTANT-DENSITY SWIRLING JET FLOWS

7.1 Overview

There are three aspects to the study presented in this chapter: i) swirling flows, an essential ingredient in practical combustion devices, had not been studied previously with the pdf method. In the present study, the pdf method is extended and applied to a coaxial swirling jet flow and the results are compared with detailed experimental data; ii) the newly developed stochastic frequency model (SFM I, section 3.3), initially developed and validated for homogeneous turbulence and self-similar flows [7-1, 7-2], is applied to and validated in conjunction with the refined Langevin model (RLM) for a general developing shear flow as represented by the coaxial swirling jet flow considered. The results are also compared against computations using the MFM and SLM I models (see Chapter 3); iii) detailed velocity statistics, conditional upon the jet from which the fluid originated, are calculated and compared against measurements, demonstrating that, in addition to other advantages, the pdf method can provide considerably more description of the flow than conventional models, and yet is computationally tractable. The results are in very good agreement with data. The experiments were jointly designed by Allison, UDRI and WPAFB personnel. The experiments were set up and conducted by UDRI personnel at WPAFB. A detailed account of the study presented in this chapter can be found in Ref. 7-2.

7.2 Background

Swirling flows (flows with appreciable bulk swirl) are an essential feature in many practical combustors such as gas turbine combustors. Swirling flows had not been studied previously with the pdf method, although there are no theoretical restrictions for applying the pdf method for such flows. For elliptic flow calculations, the treatment of swirl is automatically included as long as no assumption is made that the mean swirl velocity is zero and all the terms involving the mean swirl velocity are retained. In the present study, the necessary extensions to the boundary layer solution algorithm are made to include the treatment of swirl (see section 5.1). A salient feature of this extension is the inclusion of the mean axial pressure gradient in the calculations.

It is well known that the $k-\epsilon$ model, which is the most widely used turbulence model, is unsatisfactory for swirling flows due to effects of streamline curvature, although the model performs reasonably well for nonswirling jet flows. Several modifications to the $k-\epsilon$ model to

account for curvature effects, through corrections based on the Richardson number, have been investigated and reported in the literature. The corrections are typically made through the equation for mean dissipation as a means of correcting the turbulent transport. However, these modifications have not proved to be uniformly successful over a range of swirling flows. In this context, it is necessary to verify the performance of the pdf method for swirling flows.

The stochastic frequency model is used for the computations. This represents the one of the first applications of the joint-velocity-frequency-scalar approach for a general inhomogeneous flow. In addition to effecting complete closure of the joint pdf equation, the inclusion of the instantaneous frequency in the joint pdf leads to more realistic modeling. For example, as discussed in section 3.3, the model allows for multiple time scales rather than a single mean time scale, accounts for internal intermittency, has potential to account for large scale structures, and better accounts for the influence of the origin and history of the fluid particles on the local turbulent structure.

The pdf calculations are validated against benchmark quality data of Takahashi et al. [7-4] for a coaxial swirling jet flow. A unique feature of the laser Doppler velocimeter (LDV) measurements of Takahashi et al. [7-4] is that conditional velocity statistics are measured by seeding individual jets one at a time. This eliminates issues of velocity bias in the measurements. Conditional turbulent correlations up to fourth order have been reported. These conditional correlations are easily computed in the pdf method, and the comparisons against data serve to verify that turbulent transport is indeed accurately calculated in the pdf method.

7.3 The Joint PDF Method and Models Used

The boundary-layer algorithm described in section 5.1 with the extension for swirling flows is used. Both the mean and stochastic frequency models (MFM and SFM I) are used. The corresponding velocity models (SLM I and RLM) are used. (See Chapter 3 for details of the models.) The MFM model is also referred to as the $\langle\omega\rangle$ -model in discussions in the present chapter.

7.4 Flow Description and Computational Details

7.4.1 Flow Description

The flow considered has a central nonswirling jet of diameter $D = 9.45$ mm, a concentric annular swirling jet of diameter $D_a = 26.92$ mm surrounded by a low velocity coflow in a test section of 150 mm diameter. A schematic of the swirling jet diffusion flames set up and details of the diagnostics used are presented in the next chapter. For the experiments used in this chapter, all the jets are of air. The bulk-averaged axial velocities for the central jet, annulus, and coflow are 100, 20, and 4 m/s, respectively. The Reynolds number for the central jet is approximately 21,400.

The swirl in the annular jet is produced by a vaned swirler with a vane helix angle of 30 deg, located 96 mm upstream of the nozzle exit. The swirl number for the annular jet, S_a , calculated from measured data 1.5 mm downstream of the nozzles, is 0.41. However, the overall swirl number S_{ov} , based on the central and annular jets (not including the coflow) is 0.09 due to the large bulk axial velocity of the central jet. Since the overall swirl number is low, the inclusion of the axial pressure gradient in the boundary-layer algorithm did not have a significant effect on the results. However, with another test problem [7-5] with an overall swirl number of approximately 0.4, the inclusion of the axial pressure gradient was necessary to obtain the correct (measured) spreading of the mean axial velocity profile. The latter results are not shown here, but are reported in Ref. 7-6.

7.4.2 Initial Conditions

Initial conditions for the computations are prescribed from experimental data. The first measurement station $x = 1.5$ mm ($x/D = 0.16$) is taken as the initial plane for the calculations. The initial velocity pdf is prescribed to be joint normal with the mean and covariances taken from linearly interpolated experimental data. The initial pdf of frequency for the stochastic model is taken to be log-normal, in accordance with the construction of the model. The specification of the initial $\langle \omega \rangle$ profile for the stochastic model is discussed later in this section.

The initial profile of $\langle \omega \rangle$ for the $\langle \omega \rangle$ -model is derived from experimental data using the expression based on the k - ϵ model:

$$\langle \omega \rangle = -C_\mu \frac{k}{\langle uv \rangle_{eq}} \left(\frac{\partial \langle U \rangle}{\partial r} \right)_{eq} \quad (7.1)$$

where the equivalent velocity gradient and shear stress are given by:

$$\left(\frac{\partial \langle U \rangle}{\partial r} \right)_{eq} = \left[\left(\frac{\partial \langle U \rangle}{\partial r} \right)^2 + \left(\frac{\partial \langle W \rangle}{\partial r} - \frac{\langle W \rangle}{r} \right)^2 \right]^{1/2} \quad (7.2)$$

and

$$\langle uv \rangle_{eq} = (\langle uv \rangle^2 + \langle uw \rangle^2)^{1/2}. \quad (7.3)$$

The initial $\langle \omega \rangle$ profile was also specified from Eq. 7.1 with the assumption of local equilibrium of turbulence energy in the shear layer that yields $\langle uv \rangle_{eq} = C_\mu^{1/2} k$ so that:

$$\langle \omega \rangle = \sqrt{C_\mu} \left| \left(\frac{\partial \langle U \rangle}{\partial r} \right)_{eq} \right| \quad (7.4)$$

Although Eqs. 7.1 and 7.4 result in slightly differing profiles of initial $\langle \omega \rangle$, both specifications produced nearly the same results at the downstream stations. For the results with the $\langle \omega \rangle$ -model reported here, the specification in Eq. 7.4 was used.

The specification of $\langle \omega \rangle$ for the stochastic model needs some clarification. The production of $\langle \omega \rangle$ in the stochastic model, controlled by $C_{\omega 1}$ ($= 0.04$) (see Eq. 3.3), is only 40% of the production with the $\langle \omega \rangle$ model [Eq. 3.1, $C_1 = 0.1$]. The dissipation of $\langle \omega \rangle$ is also lower in the stochastic model, but is about 80% of that with the $\langle \omega \rangle$ -model [$C_{\omega 2} = 0.70$ versus $C_2 = 0.88$]. Hence, with the two models producing nearly the same velocity statistics, the stochastic model will yield lower values of $\langle \omega \rangle$, especially in the near-nozzle region where production is dominant due to large velocity gradients. This fact is borne out by the results presented in the next section. With the specification of the same inlet $\langle \omega \rangle$ for both the models, the stochastic model yielded lower $\langle \omega \rangle$ (by about 30%) than the $\langle \omega \rangle$ -model at the downstream locations ($x/D = 0.5$ to 10 approximately). The agreement with data of the turbulent correlations close to the nozzle ($x/D = 1.06$ and 2.65 stations) was poorer. In particular the turbulent kinetic energy was lower than in the experiments in this region. This would have an effect on the results downstream, especially the spreading rate. The results suggested that the appropriate value of inlet $\langle \omega \rangle$ for the stochastic model is about 70% of the value used for the $\langle \omega \rangle$ model, keeping in

mind that the stochastic model has fluctuations in ω and noting the differences in the velocity models discussed previously. Hence the inlet $\langle\omega\rangle$ for the stochastic model is specified to be 0.7 times the value obtained from Eq. 7.4. Again, the alternative specification of 0.7 times the value obtained from Eq. 7.4 produced nearly the same results.

To utilize the opportunity provided by the stochastic model to specify additional initial conditions based on joint velocity-relaxation rate statistics, initial conditions on $\langle v \omega \rangle$ were specified such that the correlation coefficient for $\langle v \omega \rangle$ is the negative (from wall boundary-layer considerations) of that of $\langle uv \rangle$. Although, this specification did not have a major effect on the results, it underscores the fact that more information is contained in and can be supplied to the stochastic model.

7.4.3 Conditional Statistics

As mentioned previously, LDV measurements for the flow were made by seeding individual jets one at a time. The complete flow field would be mapped by seeding a particular jet and the procedure would be repeated for the remaining jets. The experiments were shown to be repeatable. This technique measures the conditional pdfs (i.e., conditional upon the jet of origin) and avoids errors due to velocity bias that will be significant due to the large differences in the bulk velocity among the jets. However, the unconditional pdf cannot be deduced from these measurements without the additional measurement of the fraction of time the fluid from each jet spends within the sample volume. The advantage with the pdf method is that the conditional pdfs are easily calculated in addition to the unconditional pdf. Conventional turbulence models can only calculate (a limited number of) unconditional correlations and cannot calculate conditional quantities without requiring additional modeling.

The comparison between conditional measurements and calculations sheds valuable light on the detailed performance on the model and on the dynamics of individual jets. In the present study, good agreement between calculated and measured conditional quantities also implies that the calculated unconditional quantities are correct since no additional modeling is required to derive the conditional quantities.

In the calculations, the particles are tagged at the initial plane by assigning the value of c^* to be 1, 2, or 3 depending on their jet of origin. The value of c^* does not change throughout the calculation. Conditional quantities are computed for output by forming sums over particles with the same value of c^* within a spatial cell and fitting B-splines to these sums.

7.4.4 Computational Parameters

The total number of particles used in the simulations is 150,000. A large number is used to reduce statistical error especially in the calculation of the third and fourth order moments (mean and second order quantities can be calculated to within a few percent accuracy with as few as 25,000 particles). The number of cells used for forming sums is 44 and the number of basis functions used for B-splines is 20.

The stochastic model calculations took approximately 38 minutes of CPU time to march from $x/D = 1.06$ to $x/D = 26.5$ (in about 540 steps) on a CRAY YMP. The $\langle\omega\rangle$ -model took about 28 minutes and 470 steps. No significant effort has been made to optimize the computer code for speed. The storage required was about 7 megawords.

7.5 Results and Discussion

The measured mean axial velocity on the centerline of the jet at the $x = 1.5$ mm station, $\langle U \rangle_{oc}$ ($=129.7$ m/s), is used for normalizing all the velocity statistics presented. The radial distance is normalized by the radius of the central jet (R) and the axial distance is normalized by the central jet diameter (D).

Measurements [7-4] were taken across the diameter of the flow. However, in the figures presented here, the data on either side of the centerline are shown on the same side. This gives an indication of the symmetry of the flow and the amount of scatter in the data. Measurements have been reported for $x/D = 0.16$ (initial plane), 1.06, 2.65, 5.29, 7.94, 15.9, and 26.5. Figure 7-1 shows the conditional mean axial velocities from the stochastic model at four different axial stations. The calculations are in very good agreement with data. The conditional velocities show the momentum transfer between the jets as they mix. The annular jet axial velocity is accelerated as the annular fluid moves towards the centerline and the central jet decelerates. Similarly, the coflow fluid accelerates as it moves in. The conditional velocities differ significantly from each other in the developing region, and these differences become insignificant far downstream ($x/D = 26.5$).

The corresponding mean axial velocity profiles from the $\langle\omega\rangle$ -model are shown in Figure 7-2. The profiles from the $\langle\omega\rangle$ -model show greater decay of the centerline velocity than those shown by the stochastic model and data. However, the conditional velocities show the same relative trends and the agreement with data over most of the radius is quite good. The spreading rate

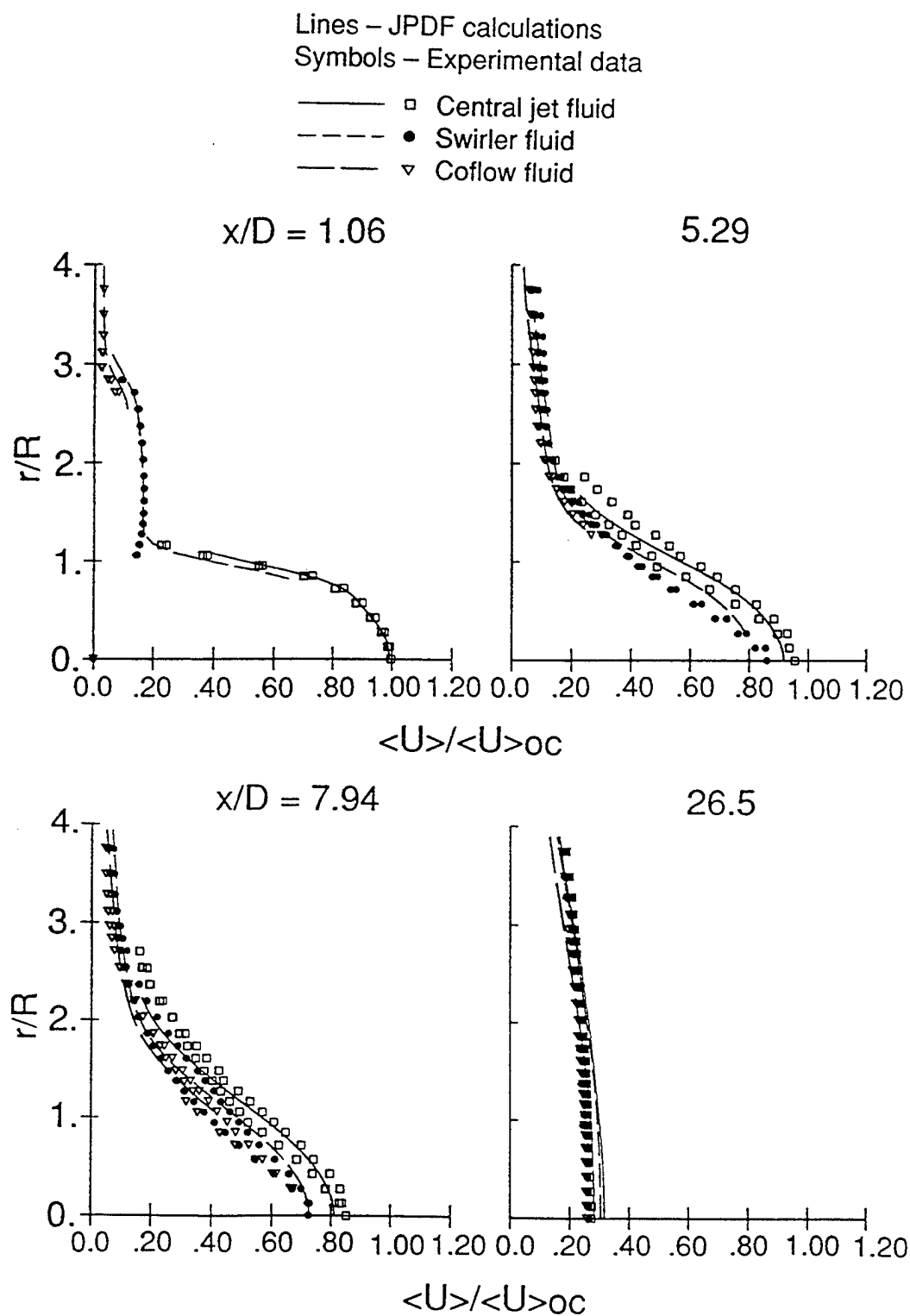


Figure 7-1. Radial profiles of conditional mean axial velocity from pdf (stochastic velocity-frequency model) calculations compared against data at various axial stations.

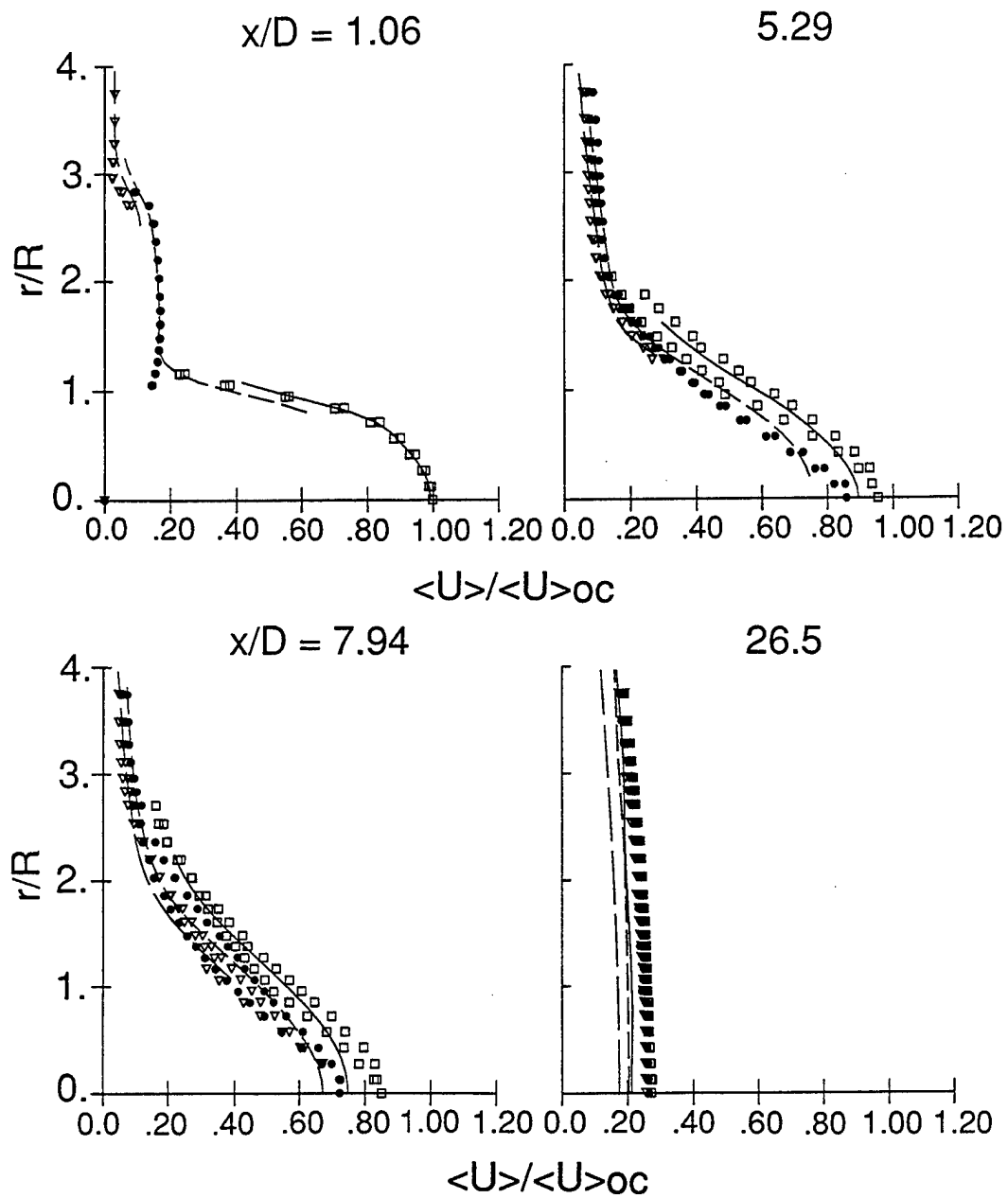


Figure 7-2. Radial profiles of conditional mean axial velocity from pdf ($\langle \omega \rangle$ -model) calculations compared against data at various axial stations (see Figure 7-1 for legend).

(and the centerline velocity decay) can be adjusted by changing the values of C_1 and C_2 . However, tests indicated that changing the constants to get a better agreement on the spreading rate would also lower the turbulent kinetic energy (i.e., $\langle u^2 \rangle$, $\langle v^2 \rangle$, and $\langle w^2 \rangle$) and results in a poorer agreement with data for those and other turbulent correlations.

The profiles of $\langle \omega \rangle$ obtained from the stochastic and $\langle \omega \rangle$ -model are shown in Figure 7-3. As explained earlier, the $\langle \omega \rangle$ profiles, especially the peak values, from the stochastic model are considerably lower than those from the $\langle \omega \rangle$ -model in the developing region ($x/D < 7.94$). In this region the production of $\langle \omega \rangle$ plays a major role due to the large mean velocity gradients. The production is lower in the stochastic model due to the choice of the constants. Further downstream, production is less and the dissipation of $\langle \omega \rangle$ plays a significant role. Since the dissipation is lower in the stochastic model than in the $\langle \omega \rangle$ -model it can be seen that the $\langle \omega \rangle$ values are higher for the stochastic model at $x/D = 26.5$. In fact, the two profiles crossover at about $x/D = 16$.

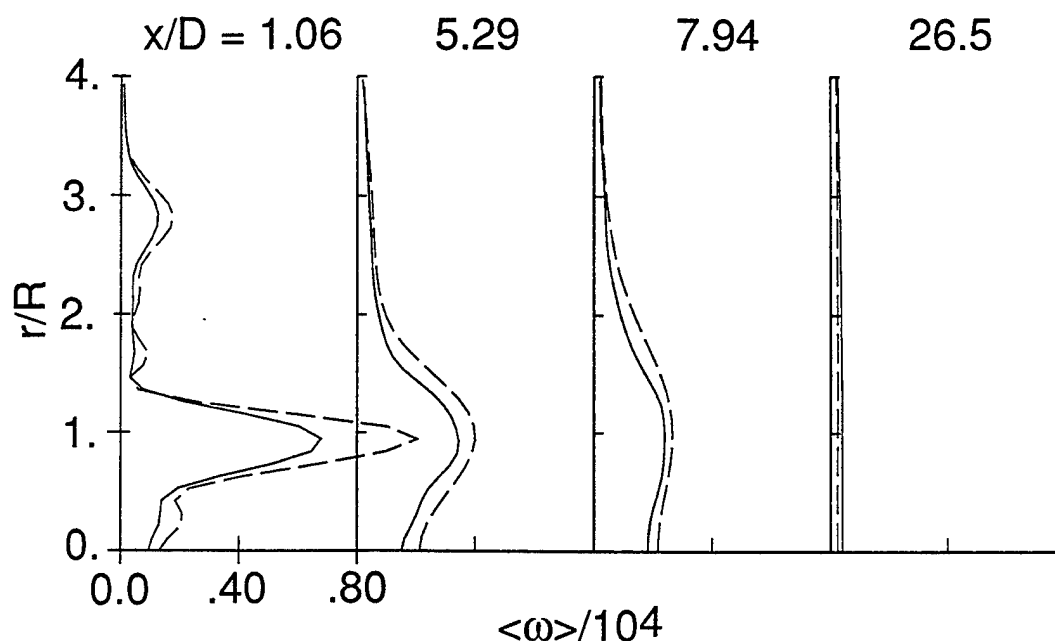


Figure 7-3. Profiles of mean relaxation rate $\langle \omega \rangle$ from stochastic model calculations (solid lines) compared with those from $\langle \omega \rangle$ -model calculations (dashed lines) at various axial stations.

The profiles of the mean swirl velocity are shown in Figure 7-4. The decay of the swirl velocity is well predicted at all stations including the downstream stations not shown here. The increase in swirl velocity of the central jet and coflow fluids as they move towards the annular swirling jet is clearly depicted by both the measured and calculated profiles. The profiles of $\langle W \rangle$ calculated by the $\langle \omega \rangle$ -model are also in good agreement with data. The negative values of $\langle W \rangle$ shown by data at $x/D = 5.29$ and 7.94 are nonphysical and indicative of some experimental error

Since most significant differences among the conditional quantities exist in the near nozzle region, $x/D < 7.94$, only selected stations in this region are shown, in the interest of clarity, in the figures to follow. The results are in good agreement with data at all stations. The profiles of turbulent kinetic energy from the stochastic model are shown in Figure 7-5 for $x/D = 5.29$ and 7.94 .

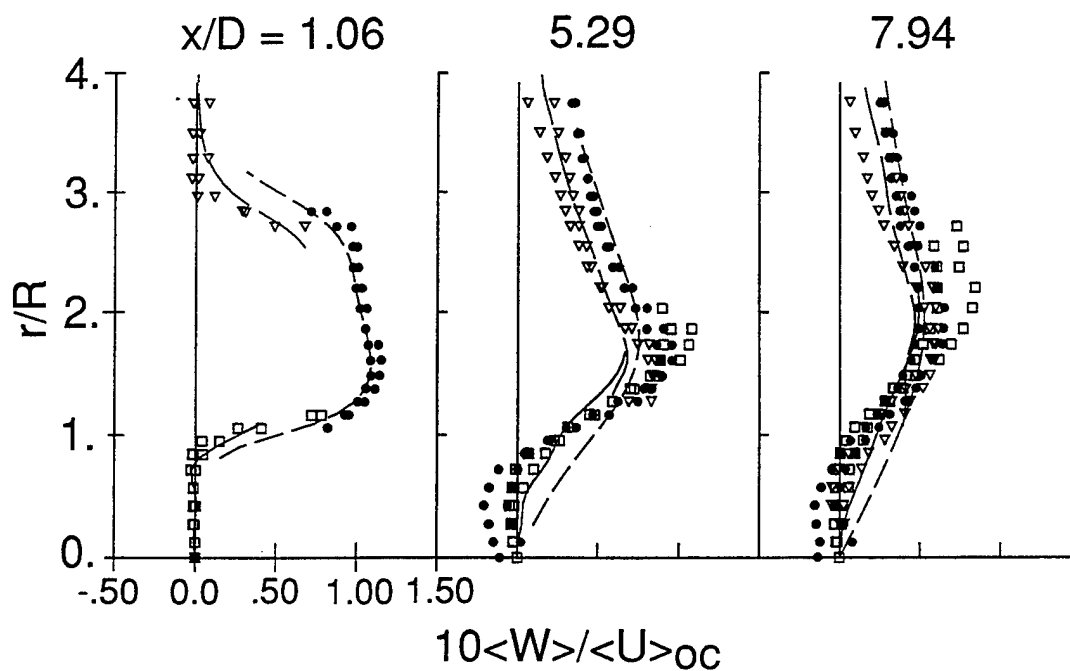


Figure 7-4. Profiles of conditional mean swirl velocity $\langle W \rangle$ from stochastic model calculations compared against data (see Figure 7-1 for legend).

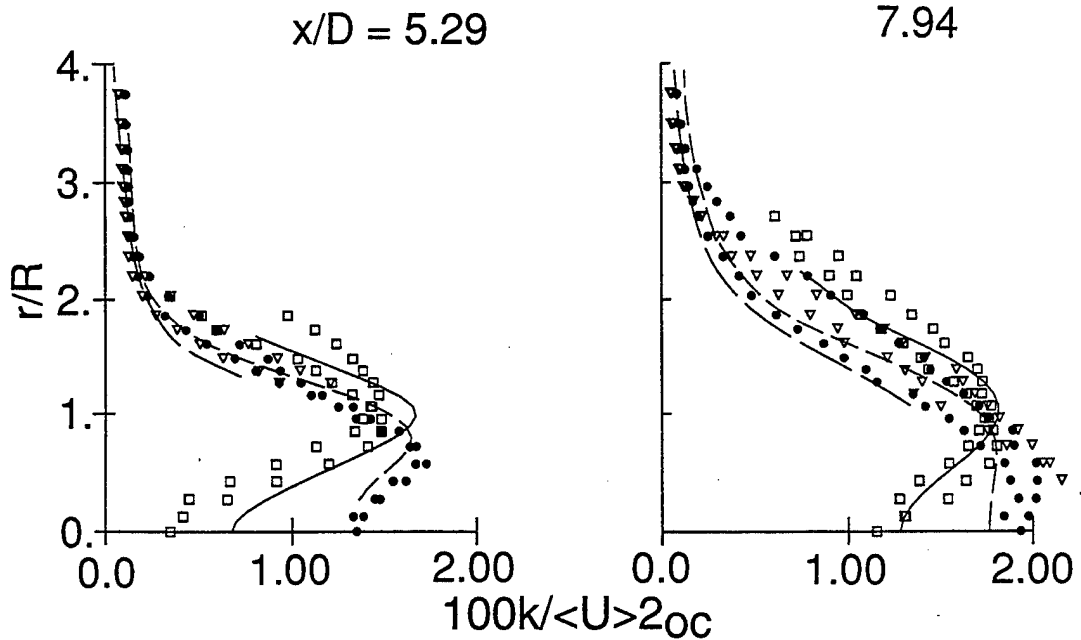


Figure 7-5. Profiles of conditional turbulent kinetic energy from stochastic model calculations compared against data (see Figure 7-1 for legend).

Figure 7-6 shows the unconditional and conditional mean axial velocity and turbulent kinetic energy at $x/D = 5.29$. The unconditional mean velocity lies within the conditional velocities at any given radius since:

$$\langle U \rangle = \gamma_j \langle U \rangle_j + \gamma_a \langle U \rangle_a + \gamma_c \langle U \rangle_c \quad (7.5)$$

where the subscripts j , a , and c denote the central jet, annular jet, and coflow, respectively, and γ is the fraction of the time that the fluid from the particular jet is found at the measurement location (note that γ 's are less than unity and add up to unity). However, the unconditional turbulent correlations, in general, need not lie within the conditional quantities. Expressions similar to Eq. 7.5 can be derived for each of the correlations that will have, in addition to a linear combination of the conditional correlations, terms involving differences between the conditional mean velocities and other conditional quantities. It is easier to visualize that while the conditional fluctuations are calculated from the corresponding conditional mean, the unconditional fluctuations are with respect to the unconditional mean. For example, in a region where the conditional velocities are significantly different, the root mean square (rms) fluctuation about the unconditional mean can be significantly larger than the rms fluctuations about the respective conditional means. This fact is illustrated by the kinetic energy profiles in Figure 7-6.

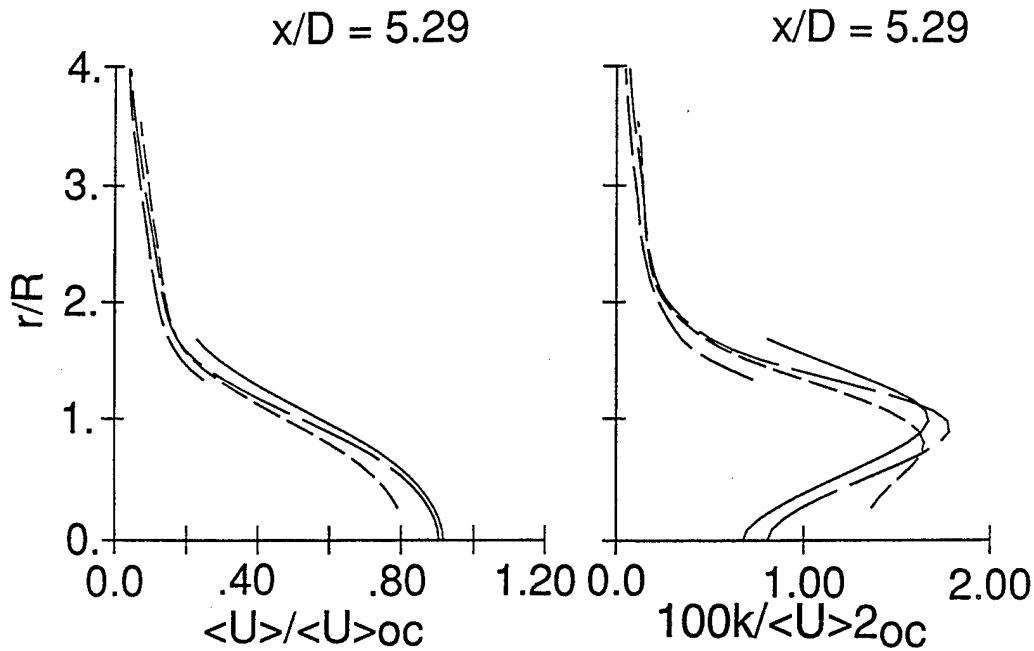


Figure 7-6. Profiles of conditional and unconditional mean axial velocity and turbulent kinetic energy at $x/D = 5.29$ from stochastic model calculations. Solid line - jet fluid; short dashed line - annular jet fluid; long dashed line - coflow; extra long dashed line - unconditional.

The kinetic energy profiles from the $\langle \omega \rangle$ -model (not shown here) are also in good agreement with data, but some differences in the details exist between the results from the two models as illustrated by the next two figures. Figures 7-7 and 7-8 show the conditional axial velocity variance from the stochastic and $\langle \omega \rangle$ -models respectively. Both models produce results that have the same level of agreement with data. However, the shift in the location of the peaks for the central and annular jets is better captured by the stochastic model than the $\langle \omega \rangle$ -model. This may be due to the fact that the turbulent transport of ω is modeled (by gradient diffusion) in the $\langle \omega \rangle$ -model while it need not be modeled with the stochastic model.

This discrepancy in the $\langle u^2 \rangle$ profile is further amplified in the $\langle u^2 v \rangle$ profiles shown in Figures 9 and 10. The quantity $\langle u^2 v \rangle$ can be interpreted as the radial turbulent flux of $\langle u^2 \rangle$. The quantity $\langle u^2 v \rangle$ will have opposite signs on either side of the location (approximately) of the peak of $\langle u^2 \rangle$ since turbulence will disperse the peak in opposite directions from the peak. Figure 7-9 shows that the stochastic model shows good agreement with data while the $\langle \omega \rangle$ -model calculations are not in as good an agreement (Figure 7-10).

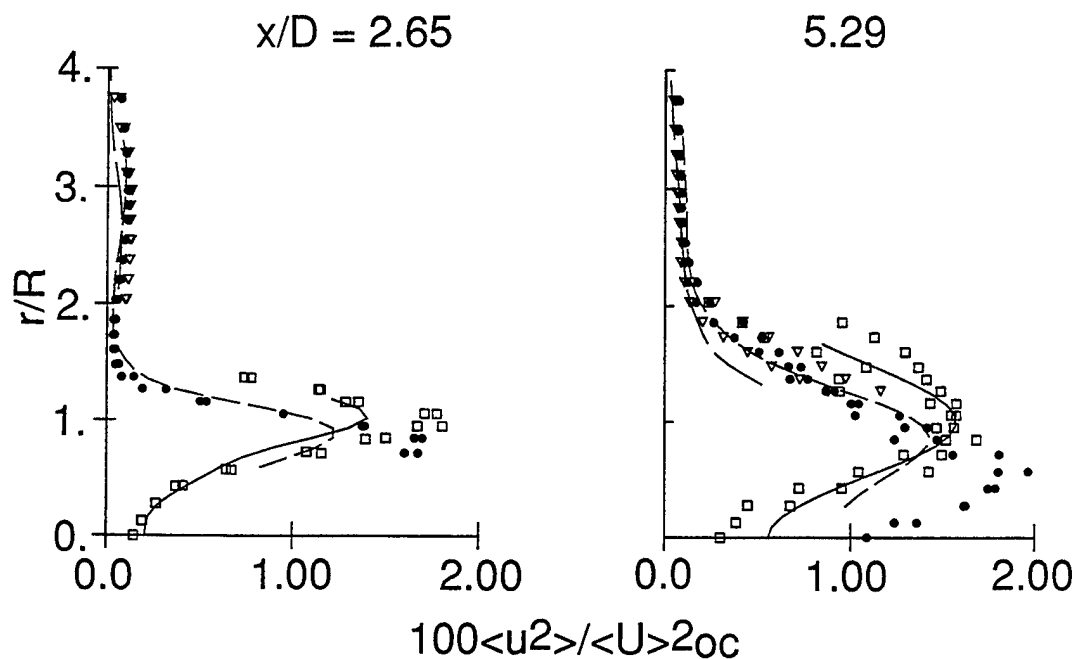


Figure 7-7. Profiles of conditional axial velocity variance from stochastic model calculations compared against data (see Figure 7-1 for legend)..

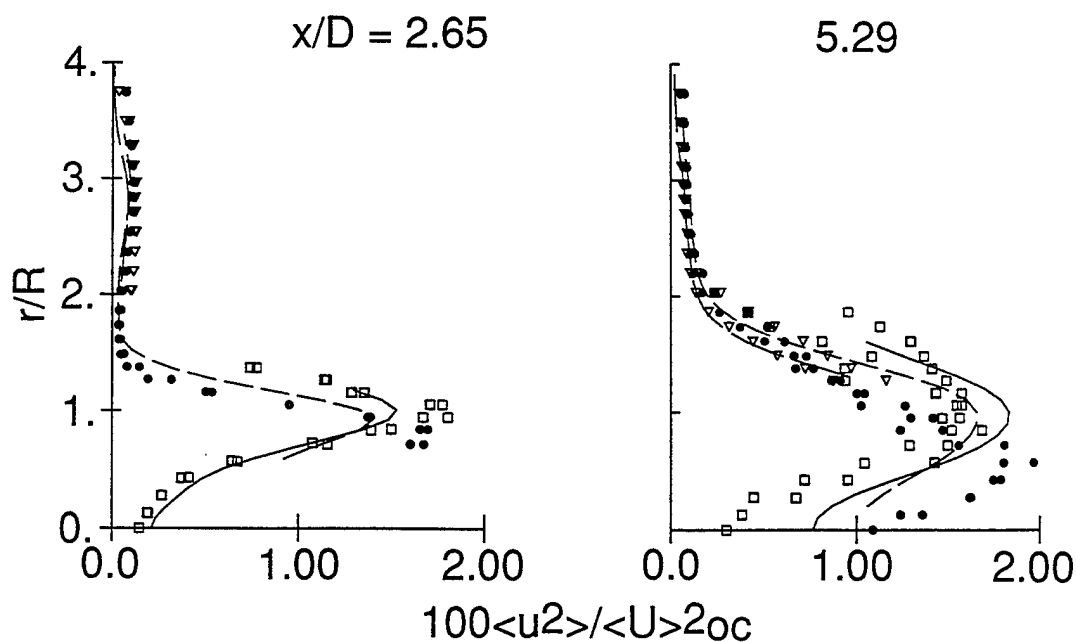


Figure 7-8. Profiles of conditional axial velocity variance from $\langle \omega \rangle$ -model calculations compared against data (see Figure 7-1 for legend)..

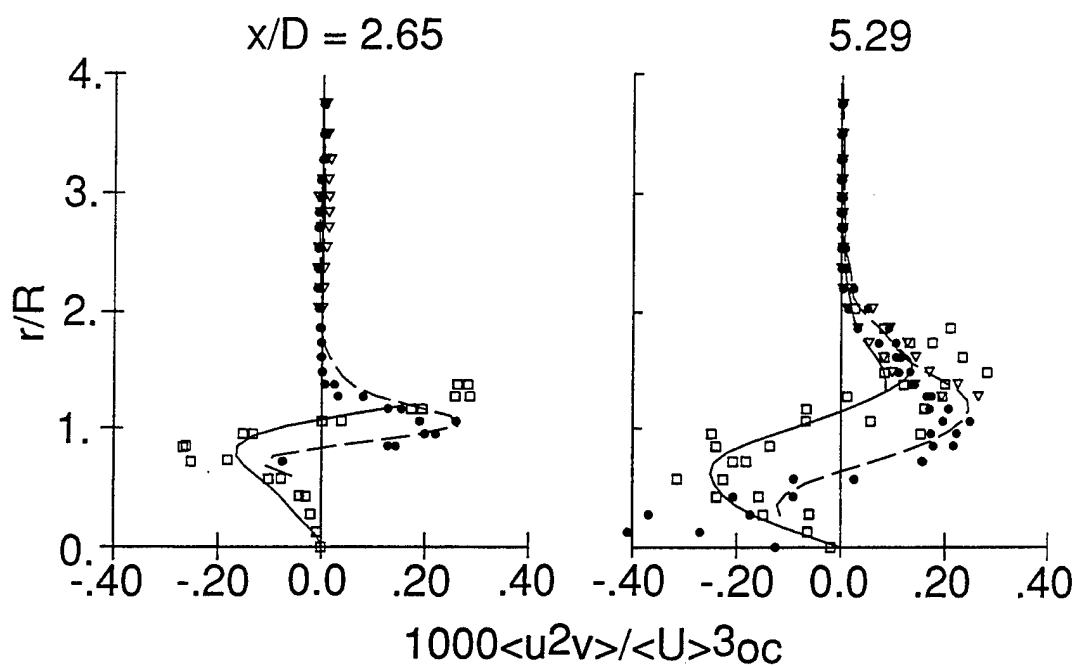


Figure 7-9. Profiles of (conditional) triple correlation $\langle u^2 v \rangle$ from stochastic model calculations compared against data (see Figure 7-1 for legend).

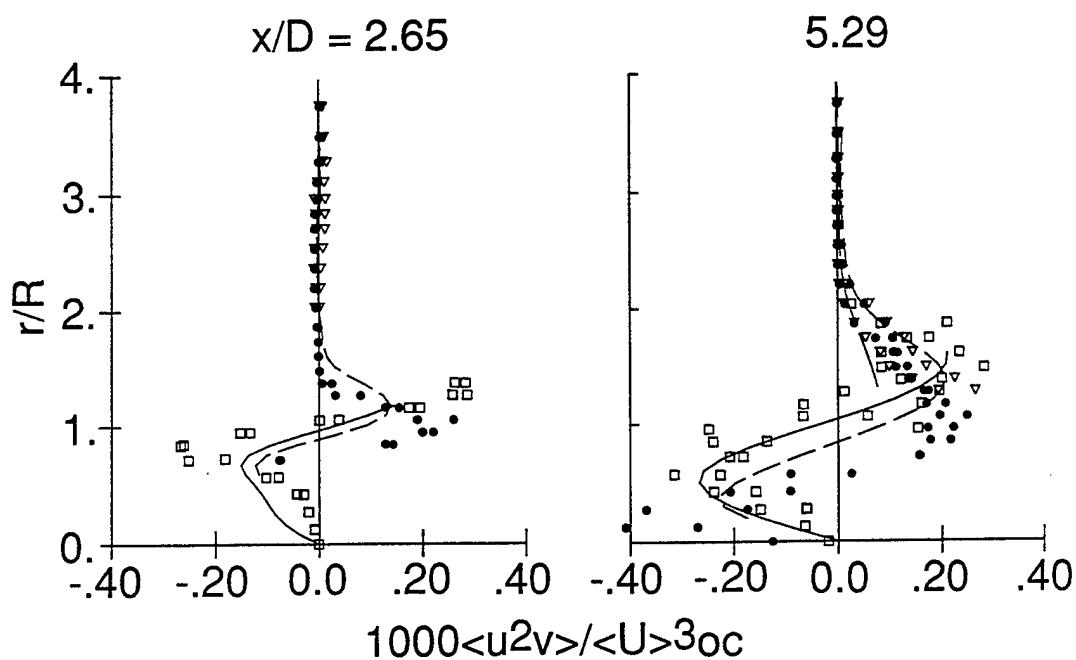


Figure 7-10. Profiles of (conditional) triple correlation $\langle u^2 v \rangle$ from $\langle \omega \rangle$ -model calculations compared against data (see Figure 7-1 for legend).

One can draw an analogy between $\langle u^2 v \rangle$ (the transport of the velocity variance $\langle u^2 \rangle$ in the v -direction) and $\langle \phi^2 v \rangle$ (the transport of $\langle \phi^2 \rangle$, variance of a scalar ϕ in the v -direction). It is important to calculate scalar transport (both mean and fluctuation of the scalar) accurately, especially in reacting flows, since it significantly affects local heat release rates and pollutant formation. It is even more critical when there is mixing between different streams (such as fuel and oxidizer in diffusion flames).

In Reynolds-stress closures, all third-order correlations (such as $\langle u^2 v \rangle$) are modeled, usually by gradient diffusion. In the present study, the flow under consideration was calculated using the RSM of Daly and Harlow [7-7] that is widely used. The details of the code and models used are presented in Ref. 7-8. The model for $\langle u^2 v \rangle$ is:

$$\langle u^2 v \rangle = -C_s \frac{k}{\langle \epsilon \rangle} \langle v^2 \rangle \frac{\partial \langle U \rangle}{\partial r} \quad (7.6)$$

where $C_s = 0.22$. The profile of (unconditional) $\langle u^2 v \rangle$ calculated from Eq. 7.6 with the right-hand side quantities taken from the Reynolds-stress calculations (short dashed line) is compared against the unconditional $\langle u^2 v \rangle$ profile from the stochastic model calculations (solid line) in Figure 7-11. The comparison shows that the RSM calculations severely underpredict the transport of $\langle u^2 \rangle$ especially at the stations close to the nozzle. The magnitude of $\langle u^2 v \rangle$ is lower because the RSM calculations also grossly underpredict $\langle u^2 \rangle$ in this region. In addition the $\langle u^2 v \rangle$ profiles from the RSM calculations change sign at a different radial location than the pdf calculations since the peaks of $\langle u^2 \rangle$ are also shifted in the RSM calculations. These differences get larger further downstream. A better test of the gradient diffusion hypothesis would be to use the pdf results for the right-hand side in Eq. 7.6. These profiles (long dashed lines in Figure 7-11) also show differences both in magnitude and the location where the profiles change sign. Though these discrepancies are not dramatic for the flow considered here, they underscore the fact that the gradient diffusion hypothesis could lead to different results and in the case of reacting flows where counter-gradient diffusion has been demonstrated the results would be erroneous.

It should be noted that even with the scalar pdf method in which the joint pdf of scalars only is considered, the turbulent flux of the scalar pdf is modeled by gradient-diffusion. While the scalar-pdf method is a useful tool for the development of reduced reaction mechanisms, since reaction still appears in closed form in the method, the full potential of the pdf method can only be realized by the velocity-scalar joint pdf method.

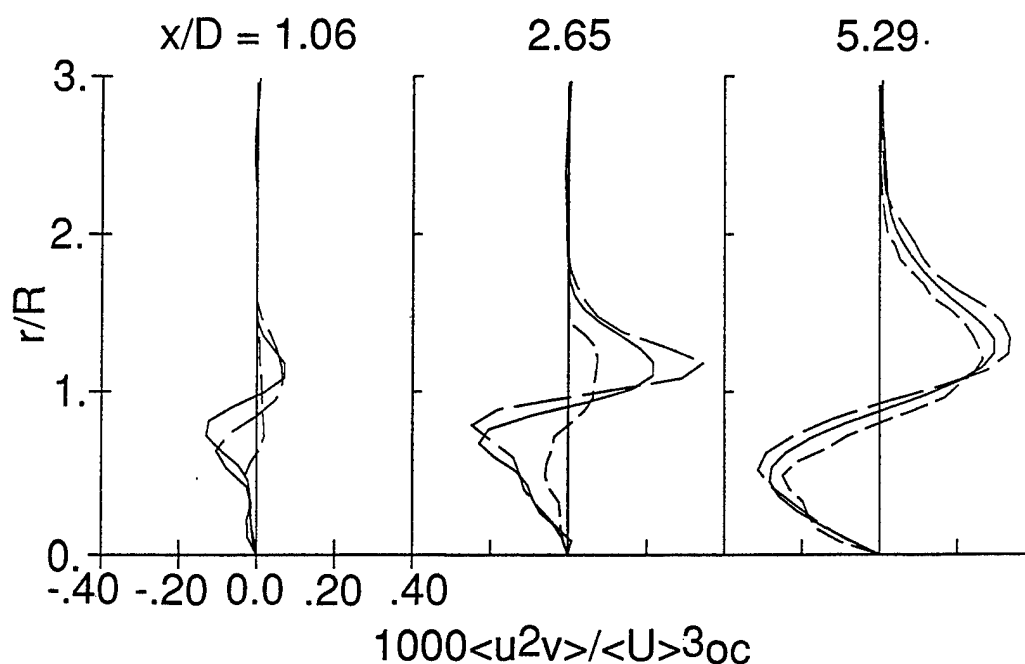


Figure 7-11. Profiles of (unconditional) triple correlation $\langle u^2 v \rangle$ from stochastic model calculations (solid line); from Reynolds-stress model (Eq. 7.6) using results from Reynolds-stress closure calculations (short dashed line); and from model (Eq. 7.6) using results from stochastic model calculations (long dashed line).

Figure 7-12 shows the conditional $\langle u^3 \rangle$ profiles at $x/D = 2.65$ and 5.29 . The dramatic differences between the conditional quantities is well predicted by the calculations. The results from the $\langle \omega \rangle$ -model show similar discrepancies as seen for $\langle u^2 v \rangle$. Figure 7-13 shows the (conditional) fourth order correlation $\langle w^4 \rangle$ from the stochastic model at $x/D = 5.29$ and 7.94 . Considering that fourth order conditional statistics are being measured and computed, the results are in very good agreement with data. The corresponding profiles for the $\langle \omega \rangle$ -model are shown in Figure 7-14. These profiles are also in good agreement with data. However the radial separation between the peak locations for the central jet and annulus at $x/D = 5.29$ are better predicted by the stochastic model.

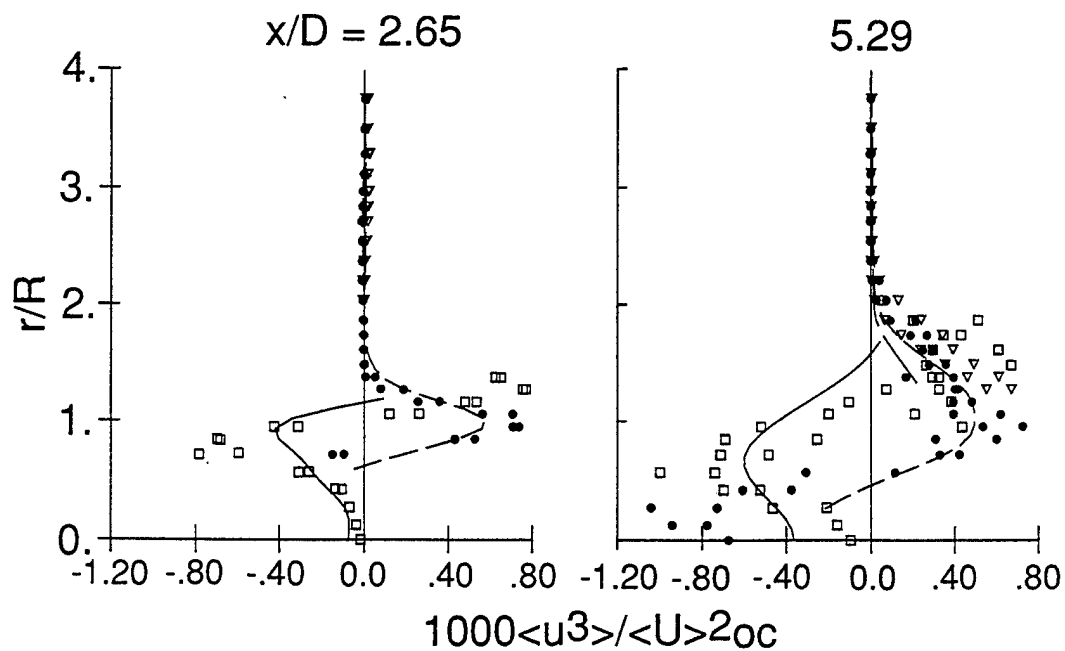


Figure 7-12. Profiles of conditional $\langle u^3 \rangle$ from stochastic model compared against data (see Figure 7-1 for legend)

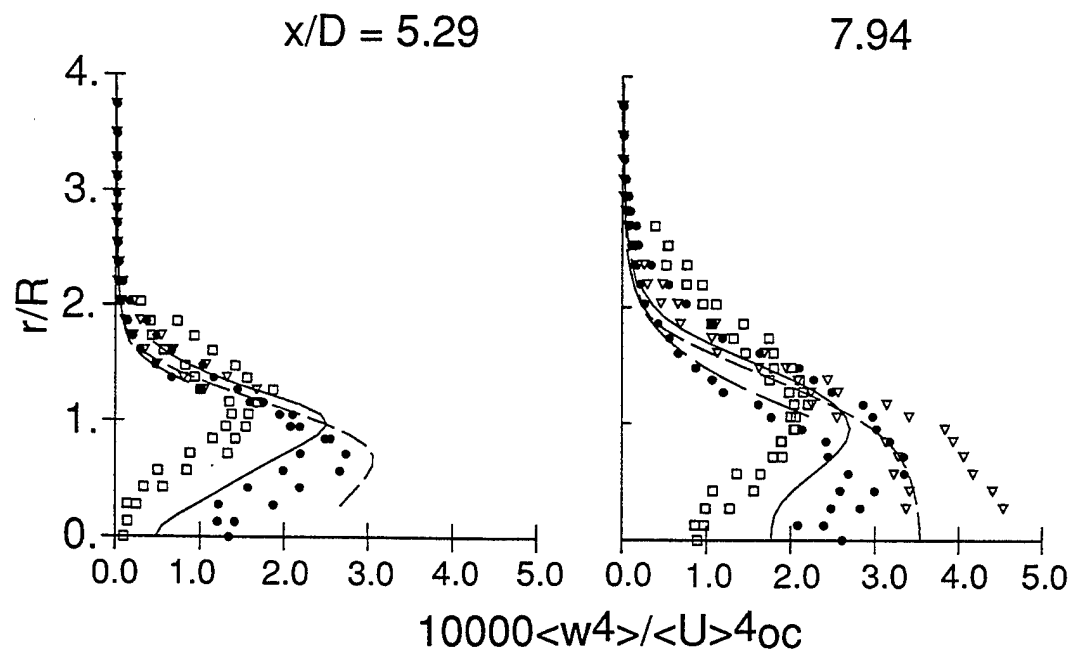


Figure 7-13. Profiles of (conditional) fourth-order correlation $\langle w^4 \rangle$ from stochastic model calculations compared against data (see Figure 7-1 for legend).

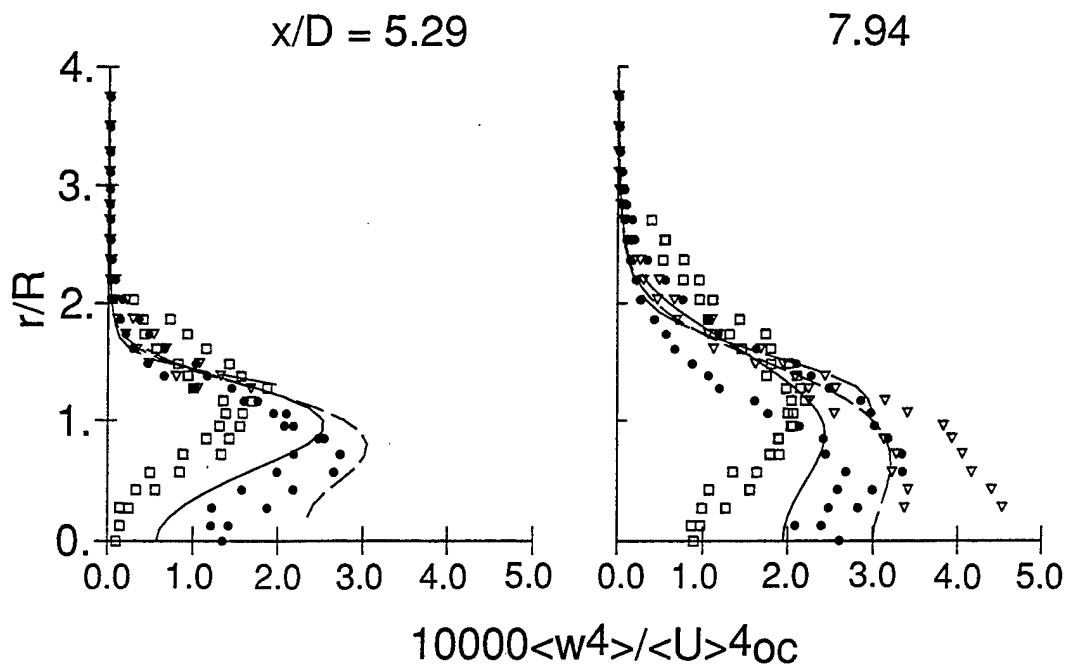


Figure 7-14. Profiles of (conditional) fourth order correlation $\langle w^4 \rangle$ from $\langle \omega \rangle$ -model compared against data (see Figure 7-1 for legend).

7.6 Summarizing Remarks

Swirling flow calculations have been made with the pdf method. The newly developed stochastic frequency and velocity models (SFM I and RLM respectively) have been validated against benchmark quality data for a coaxial swirling jet flow. Detailed comparisons between measured and calculated conditional means and correlations up to fourth order have been made. The calculations are in very good agreement with data. The present study suggests the values $C_{\omega 1} = 0.04$ and $C_{\omega 2} = 0.7$ for the two constants that significantly affect the evolution of the mean frequency $\langle \omega \rangle$ in the SFM I model.

Swirling flows were calculated for the first time using the pdf method. While extensions to the algorithm were made to include the axial pressure gradient and additional terms due to nonzero mean swirl velocity, no specific modifications were made to the SFM and RLM models or elsewhere on account of swirl.

Calculations were also made with the pdf method using a transport model for $\langle \omega \rangle$. These results are also in reasonably good agreement with data, although the stochastic model better predicts some of the details of turbulent transport.

The calculated results from the stochastic model were compared against gradient-diffusion models used by conventional Reynolds-stress closures, and the latter were found to be deficient. By extension, the scalar pdf method is also subject to the same limitations since gradient diffusion modeling is used for turbulent transport of the scalar pdf.

The stochastic frequency model provides complete closure for the joint pdf method and eliminates the need to supply a time scale for the solution of the pdf transport equation. The stochastic model also contains more information than that based on $\langle\omega\rangle$, and allows the flexibility to build in more information than currently used in further developing the model. The application of the SFM I and RLM models to swirling jet diffusion flames is reported in the next section.

REFERENCES

- 7-1. S. B. Pope and Y. L. Chen, "The Velocity-Dissipation Probability Density Function Model for Turbulent Flows," Physics of Fluids A, 2, No. 8, 1990, pp 1437-1449.
- 7-2. S. B. Pope, Physics of Fluids A, 3, No. 8, 1991. (See also Erratum, S. B. Pope, Physics of Fluids A, 4, No. 5, 1992)
- 7-3. M. S. Anand, S.B. Pope and H.C. Mongia (1993) "PDF Calculations for Swirling Flows," AIAA 93-0106. To be published AIAA Journal.
- 7-4. F. Takahashi, M. D. Vangsness, and V. M. Belovich, AIAA-92-0580.
- 7-5. J. P. Sislian and R. A. Cusworth, UTIAS Report No. 281, University of Toronto, Toronto, 1984.
- 7-6. M. S. Anand, S. B. Pope, and H. C. Mongia, "Combustor Design Model Evaluation," Quarterly Report No. 9, EDR 13417H, Allison Gas Turbine Division, GMC, Indianapolis, January 1990.
- 7-7. B. J. Daly and H. F. Harlow, Physics of Fluids, 13, 1970.
- 7-8. M. Nikjooy and H. C. Mongia, International Journal of Heat and Fluid Flow, 12, No. 1, 1991.

8. SWIRLING JET DIFFUSION FLAMES

8.1 Overview

Computations using the joint velocity-frequency-scalar pdf method as well as benchmark quality experimental data for swirling and nonswirling hydrogen jet diffusion flames are reported in this chapter. Previous studies of diffusion flames reported in literature have been limited to nonswirling flames and have had no detailed velocity data reported in the developing (near-nozzle) region of the flames. The measurements and computations reported herein include velocities (mean and higher moments up to fourth order) and temperature (mean and variance) near the burner exit and downstream locations up to 26.5 jet diameters. The computed results are in good agreement with data. This study serves to further validate the joint velocity-frequency-composition pdf method for reacting flows as well as present data that can be used for validation of other reacting flow models as well.

8.2 Background

Although jet diffusion flames have been studied extensively and reported in the literature, there are voids with respect to two key aspects. First, there are no detailed measurements, especially velocity measurements, in the developing regions of the flames, and second, the flames have been predominantly nonswirling. Swirl is widely used in practical combustion systems such as gas turbine combustors for flame stabilization and enhancing fuel-air mixing and combustion intensity. It is necessary that the turbulent combustion models be validated in detail in simpler flames incorporating the essential features of practical flows before they can be used with confidence to design practical combustion systems. In the present study detailed velocity and temperature measurements are presented for swirling and nonswirling hydrogen jet diffusion flames in the developing region of the flames (<30 jet diameters in axial distance), and the measurements are used to further validate the joint pdf method.

The present computations of diffusion flames with the pdf method differ from previous computations in that for the first time a) swirling diffusion flames are being computed and b) detailed comparison with data is made in the developing region of the flame. As explained in the previous chapter, notable feature of the measurements reported in this study is that the velocity

correlations are conditional upon the fluid originating from a given inlet stream. As a result errors due to velocity bias are avoided. These conditional quantities are readily computed in the pdf method without need for additional modeling, and serve as severe tests for the method's ability to predict the details of the individual streams and the transport processes between the streams.

The experiments were conducted by Takahashi et al. (UDRI) at WPAFB's Fuels Laboratory. The study is reported in detail in Ref. 8-1.

8.3 Experimental Setup and Techniques

Figure 8-1 shows a schematic of the combustor system used. It consists of a central fuel tube (9.45 mm inner diameter [D], 0.2 mm lip thickness, 806 mm length) and a concentric annulus-air tube (26.92 mm inner diameter) centered in a vertical test section (150 x 150 mm square cross section with rounded corners, 486 mm length) through which external air is supplied. The test section is sided with four quartz windows for optical observations and diagnostics. A helical vane swirler unit can be placed in the annulus channel 96 mm upstream from the jet exit. Swirlers of vane angles 0 deg, 30 deg, and 45 deg were used in the present study.

The three-component LDV system, described in detail in Takahashi et al. [8-2], consists of the two segments of three-beam two-channel optics and two-beam one-channel optics. The former utilizes a 514.5 nm line of an argon-ion laser (Spectra Physics 171; 15W nominal output) and measures the velocity components in the directions of ± 45 deg off the jet axis. The latter utilizes a 488.0 nm line of the laser and measures the tangential velocity component. The overlapping probe volume is approximately a 100 μm diameter sphere. The calculated fringe spacing is approximately 3.6 mm. Submicron-size zirconia (ZrO_2) particles (97%, $<1 \mu\text{m}$) are used as the seed particles. A portion of the data was filtered out by the so-called $n\text{-}\sigma$ method (i.e., velocities whose deviation from the mean exceeded n times the standard deviation [σ] are eliminated). The coefficient $n = 4$ was employed because preliminary processing tests showed that $n = 3$ cut off some valid data and altered high moments considerably.

LDV measurements were made by seeding one stream at a time and completing all the axial and radial scans before seeding the next stream and repeating the scans. All the LDV measurements reported are conditional upon the fluid originating from either the jet annulus or the coflow.

The CARS system, described in detail in Takahashi et al. [8-3], consists of a pulsed Nd:YAG laser (Quanta Ray DCR-2A, 10 ns pulse width, 10 Hz repetition rate), dye laser optics, incident

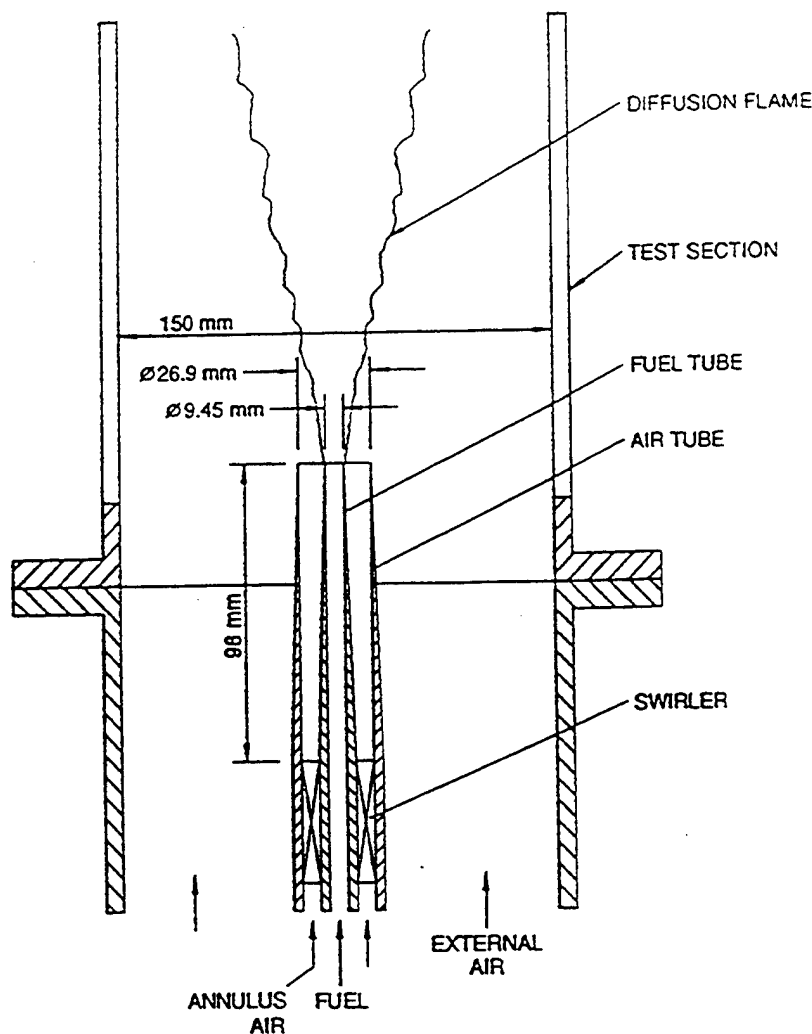


Figure 8-1. Schematic of the Swirling Jet Diffusion Flame Combustor test section.

and collection optics, a 3/4 m grating spectrometer, and an intensified charge-coupled device (CCD) camera (Princeton Instruments). The output from the laser is frequency-doubled (532 nm, ~150 mJ) and divided into four beams of nearly equal intensity. Two of these serve as the pump beams, while the other two pump a dye laser oscillator and amplifier to provide a broadband Stokes beam centered at 607 nm. The Stokes beam and the two pump beams are then focused together in a folded BOXCARs configuration. The effective probe volume size is estimated at approximately 25 mm in diameter and 250 mm in length. Typically, 500 CARS signals are acquired at each location and processed by a microcomputer. The CARS measurements are based on nitrogen molecules originated in air. Unlike seed particles which

follow fluid elements, molecules diffuse among different species. Therefore, the CARS data are unconditional upon the origin of the fluid if they are mixed. In the jet-to-annulus fluid boundary zone near the jet exit, the determination of CARS temperature becomes difficult due to the interference by nonresonant background emission from hydrogen molecules. The accuracy of the temperature measurements is estimated to range between 10% near room temperature and 5% near the flame temperature, with the largest contribution to uncertainty from shot-to-shot variation in the Stokes-laser spectral distribution.

8.4 Computations

8.4.1 The Joint PDF Method and Models Used

The pdf method used in the present study is the same as that used for the constant-density swirling flow study reported in the previous chapter, except for the addition of the thermochemistry and molecular diffusion due to mean scalar gradient described later and, obviously, the variability of density. The SFM I and RLM models are used for the frequency and velocity respectively (see sections 3.3 and 3.4).

The boundary-layer (parabolic) algorithm is used here. At the axial position x , each computational particle has the position $x^*(x)$, velocity $U^*(x)$, the relaxation rate or frequency $\omega^*(x)$, and four scalar values $\phi^*(x)$, $\rho^*(\phi^*)$, $T^*(\phi^*)$ and $c^*(x)$. The scalar ϕ^* is the mixture fraction (conserved scalar) used to model the thermochemistry. Its value changes due to turbulent and molecular mixing and molecular diffusion. The scalars ρ^* and T^* are density and temperature, respectively, and are derived from ϕ^* based on the thermochemistry used. The scalar c^* is a passive scalar with no source terms (i.e., c^* is held constant), and is used to tag particles by their jet of origin.

The turbulent mixing (i.e. turbulent convection) of the mixture fraction (ϕ^*) is in closed form and need not be modeled. The molecular mixing is modeled using the improved mixing model (IMM) with the standard model constant $C_\phi = 2.0$. The molecular diffusion process is represented by Fick's Law. Typically, although it is in closed form, molecular diffusion due to mean scalar gradient is not explicitly included in the computations for high Reynolds number turbulent flows since turbulent mixing is dominant. However, in the present study, molecular diffusion is explicitly included since the stoichiometric surface lies at the outer edge of the shear layer (for most diffusion flames and especially for hydrogen flames due to the low value of the stoichiometric mixture fraction and the high diffusivity of hydrogen). In this region, the

turbulent intensity is low and molecular diffusion plays an important role in the radial spread of the flame. The change in ϕ^* over the particle time-step Δt^* due to molecular diffusion is given by:

$$\Delta\phi^* = \frac{\Delta t^*}{\rho^*} \frac{\partial}{\partial r} \left(r \langle \rho \rangle D_\phi \frac{\partial \langle \phi \rangle}{\partial r} \right), \quad (8.1)$$

where $\langle \rho \rangle$ and $\langle \phi \rangle$ are the mean density and mixture fraction respectively, and D_ϕ is the diffusivity taken as a function of $\langle \phi \rangle$ from Bilger [8-4]:

$$D_\phi = 0.26 + 257 \langle \phi \rangle + 3.5 \times 10^8 \langle \phi \rangle^5 \text{ (cm}^2\text{/s) for } 0 \leq \langle \phi \rangle \leq 0.0325; \text{ and}$$

$$D_\phi = 3.8 - 3.03 \langle \phi \rangle + 27.5 (1.0001 - \langle \phi \rangle)^{10} \text{ (cm}^2\text{/s) for } 0.0325 < \langle \phi \rangle \leq 1.0.$$

Means and other correlations are extracted from the solution at any desired axial station x by forming sums of particle properties within spatial bins in the lateral direction (r -direction) and fitting cubic B-splines to these sums. Typically density-weighted (Favre) means are calculated as is appropriate for reacting flows; however, means weighted by any desired quantity can be computed.

8.4.2 Thermochemistry

Due to the highly reactive nature of the fuel used, namely hydrogen, the thermochemistry in the present study is described using a fast one-step reaction in equilibrium. This allows the modeling of the diffusion flame using a single conserved scalar, the mixture fraction which is unity in the hydrogen stream and zero in the air streams. The reaction is completely described by the evolution of the mixture fraction. The temperature and density are then functions of mixture fraction alone and are determined from the equilibrium composition at the given value of ϕ , using the heat of combustion, the specific heat at constant pressure (C_p) of the mixture as a function of temperature, and the ideal gas law. In the present study the equilibrium calculations were performed at different values of ϕ prior to the pdf calculations and the values of specific volume (inverse of density) and temperature were tabulated for use (through linear interpolation) in the pdf calculations. The tables consisted of 21 points between $\phi = 0$ and the stoichiometric value $\phi_{st} = 0.0282$ and 51 points between ϕ_{st} and $\phi = 1$ to provide sufficient accuracy for the pdf calculations.

8.4.3 Initial Conditions

Initial conditions for the computations are prescribed from experimental data. The first measurement station $x = 1.5$ mm ($x/D = 0.16$) is taken as the initial plane for the calculations. The initial velocity pdf is prescribed to be joint normal with the mean and covariances taken from linearly interpolated experimental data. The initial pdf of turbulence frequency is taken to be log-normal, i.e., $\ln(\omega^*/\langle\omega\rangle)$ has a normal distribution with mean and variance $-1/2$ and 1 , respectively, in accordance with the construction of the model. The initial profile of $\langle\omega\rangle$ is derived from experimental data using the following expression, as described in the previous chapter.

The initial profiles of the mean mixture fraction and its variance $\langle\phi'^2\rangle$ are deduced from the measured mean and variance of temperature at the $x = 1.5$ mm location. The value of $\langle\phi\rangle$ is deduced from the tabulated values of temperature versus mixture fraction and the value of $\langle\phi'^2\rangle$ is estimated by

$$\langle\phi'^2\rangle = \frac{\overline{T'^2}}{T_{st}} \phi_{st}, \quad (8.2)$$

where $\overline{T'^2}$ is the measured variance of temperature, and T_{st} ($= 2377\text{K}$) is the temperature at the stoichiometric mixture fraction ϕ_{st} . The pdf of ϕ is prescribed to be Gaussian with $\langle\phi\rangle$ and variance $\langle\phi'^2\rangle$.

8.5 Results and Discussion

Experiments and computations were performed for the four cases listed in Table 8-1. The velocities U_j , U_a , and U_e are the nominal bulk-averaged axial velocities of the fuel jet, annular air jet, and the coflowing air stream, respectively. Two of the cases are nonswirling and two are swirling. For Case 2, the high-velocity nonswirling case, the lip thickness of the fuel tube used was 1.2 mm in order to anchor the flame and keep it from lifting. For all other cases, the tube walls were chamfered to form knife edges at the exit.

TABLE 8-1.
FLOW CONDITIONS

<u>Case No.</u>	<u>U_j - m/s</u>	<u>U_a - m/s</u>	<u>U_e - m/s</u>	<u>Swirler Angle - deg</u>
1	25	4	1	0
2	100	20	4	0
3	100	20	4	30
4	100	20	4	45

The nominal Reynolds number for the hydrogen jet based on U_j and the jet diameter (D) is 2208 for Case 1 and 8830 for the others, and the nominal Reynolds number for the annular air jet based on U_a and its hydraulic diameter is 8400 for Case 1 and 33,600 for the others. The swirl numbers for the annular jet, calculated from the measured axial and tangential velocities at the initial plane, are 0.382 for Case 3 and 0.516 for Case 4.

To be concise, only sample results from a nonswirling case (Case 2) and the two swirling cases in Table 8-1 will be presented here. Case 2 was selected to allow a more direct comparison between the nonswirling and swirling cases. Detailed tables and plots of the measured data for the four cases are reported in Takahashi et al. [8-2, 8-3, 8-5 through 8-8], and the tabulated data are available on diskettes. Measurements have been made at axial stations $x/D = 0.16$ (initial plane), 1.06, 2.65, 5.29, 7.94, 15.9, and 26.5. Radial profiles of conditional mean velocities and velocity correlations up to fourth order as well as unconditional mean and variance of temperature have been reported.

The notation used to present the results for the velocity components is $\underline{U} \equiv (U, V, W) \equiv (\langle U \rangle + u, \langle V \rangle + v, \langle W \rangle + w)$. The notation for the temperature results are presented later. The measured mean axial velocity on the centerline at $x/D = 0.16$ denoted as $\langle U \rangle_{oc}$ is used to normalize the velocities and the temperature at the stoichiometric mixture fraction, T_{st} ($= 2377K$), is used to normalize temperatures. The values of $\langle U \rangle_{oc}$ are 132.8 m/s, 130.3 m/s, and 130.0 m/s for Cases 2, 3, and 4, respectively. The radial distance is normalized by the fuel jet radius R ($= D/2$).

Figure 8-2 shows the computed conditional and unconditional mean axial velocity profiles for the nonswirling case (Case 2) compared against measurements at various axial stations. The calculations are in good agreement with data. There are differences in the velocities of the fluids originating from the different streams as expected. The annulus air increases its axial velocity as

it moves towards the central jet, but its axial velocity remains lower than that of the central jet. As the jets spread, the profiles become flatter and the differences get smaller at the downstream locations $x/D = 15.9$ and $x/D = 26.5$ (not shown). While the unconditional data cannot be deduced from the conditional data without additional measurement of the intermittency factor for the different streams, unconditional and conditional quantities of any order can be extracted from the pdf solution. The unconditional mean axial velocity in Figure 8-2 lies between the conditional values as expected.

Figure 8-3 shows the computed profiles of mean temperature for Case 2 compared against data. Both the Favre-averaged (density-weighted) mean temperature $\langle T \rangle$ as well as the Reynolds-averaged (volume-weighted or spatially averaged) mean temperature denoted by \bar{T} are shown. The Favre average is lower in the flame's outer radial region, where there is significant probability of hot products and cold air since the cold air is an order of magnitude denser (1.17 kg/m^3 at the inlet temperature of 298K) and contributes more to the average than the hot rarer air (0.125 kg/m^3 at T_{st}), whereas on the inside of the flame the difference is negligible since the densities of cold unburnt hydrogen (0.082 kg/m^3 at the inlet temperature of 298K) and the burnt products are of the same order of magnitude. Clearly, the spatial mean is much closer to the measured data, illustrating that the CARS measurement represents a spatial average and is not weighted by the mass flow into the measurement volume. This is an important observation and draws attention to the fact that although Favre averages are conventionally used in the computations of variable-density flows, one has to be careful to use the appropriate averaging while comparing with measurements. On the other hand, if the seeding of the flow is uniform, LDV measurements represent Favre means, and hence the Favre means are used while comparing velocity data. However, the velocity statistics computed using Reynolds averaging were nearly identical to those computed using Favre-averaging. This indicates that the velocity distribution of the high and low density fluids in the mixture are nearly identical at any point in the flow.

The calculated profiles of (volume averaged) temperature in Figure 8-3 show the locations of the temperature peaks are well predicted; however, the peak values are lower than the measured values in the region between $x/D = 2.65$ and $x/D = 7.94$. At the further downstream locations $x/D = 15.9$ and $x/D = 26.5$, the calculated temperature is higher than the data at the outer radial locations.

Figure 8-4 shows the temperature variance for the nonswirling case (Case 2). Again, the Reynolds-averaged variance is in much better agreement with the data than the Favre average. The second peak of temperature variance on the inside (i.e., towards the centerline) seen in the

calculations corresponds to the inner gradient of the temperature peak. Obviously, this is the region which lacks nitrogen and the CARS data are either not available or the measured temperature variance is expected to be low in this region.

The data as well as the computations in Figures 8-2, 8-3, and 8-4 show that the flame lies at the outside edge of the shear layer between the fuel jet and the annulus jet as expected due to the low value of ϕ_{st} .

Results for the 30 deg swirl case (Case 3) will now be presented. Figure 8-5 shows the radial profiles of mean conditional axial velocity at different downstream stations in the developing region. For clarity of the figure, the calculated unconditional velocity is omitted. The spreading of the jet is much faster than in Case 2 as a result of the enhanced mixing due to swirl in Case 3. The location of the shear layer is at a larger radial distance and the width of the shear layer is also larger than for the nonswirling case (Figure 8-2), for example at $x/D = 7.94$. Differences between the conditional means from the three streams are evident.

Overall, the computations are in good agreement with the data in terms of the trends, locations, and magnitudes of the conditional velocities; however, some differences exist. The computations show a slightly slower rate of spreading of the hydrogen jet than the data. Although the spreading rate in the computations could be adjusted by adjusting the constants in the Langevin equation and the turbulent frequency equation, the differences are not significant enough to undertake such an exercise; hence, the constants used in previous study (Chapter 7) were retained. The data, especially at $x/D = 2.65$ and 5.29 , indicate the outer edge of the hydrogen jet spreads especially faster than the bulk of the jet. The differences between the conditional velocities and the differences between the computations and the data diminish at the downstream locations $x/D = 15.9$ and 26.5 (not shown here).

Figure 8-6 shows the conditional mean tangential (or swirl) velocities for Case 2. The development and decay of the swirl in the three streams is well predicted, although the computations show larger differences between the swirl velocities of the different streams than indicated by the data. The computations show that the swirl velocities for the initially nonswirling hydrogen jet and coflowing stream lag behind those for the annular swirling jet as one may expect.

The calculated Reynolds-averaged mean temperatures \bar{T} are compared against data in Figure 8-7. The agreement between the computations and the data is better than in Case 2 in terms of the magnitude and shape of the temperature peaks. For the swirling case (Case 3), the measured

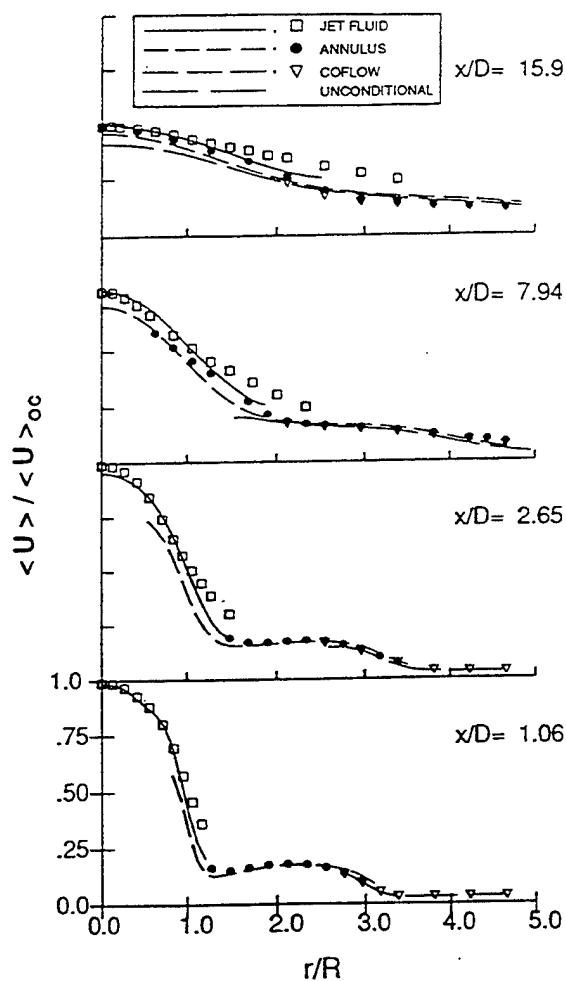


Figure 8-2. Radial profiles of computed conditional and unconditional mean axial velocity (lines) compared against data (symbols) for the nonswirling case (Case 2).

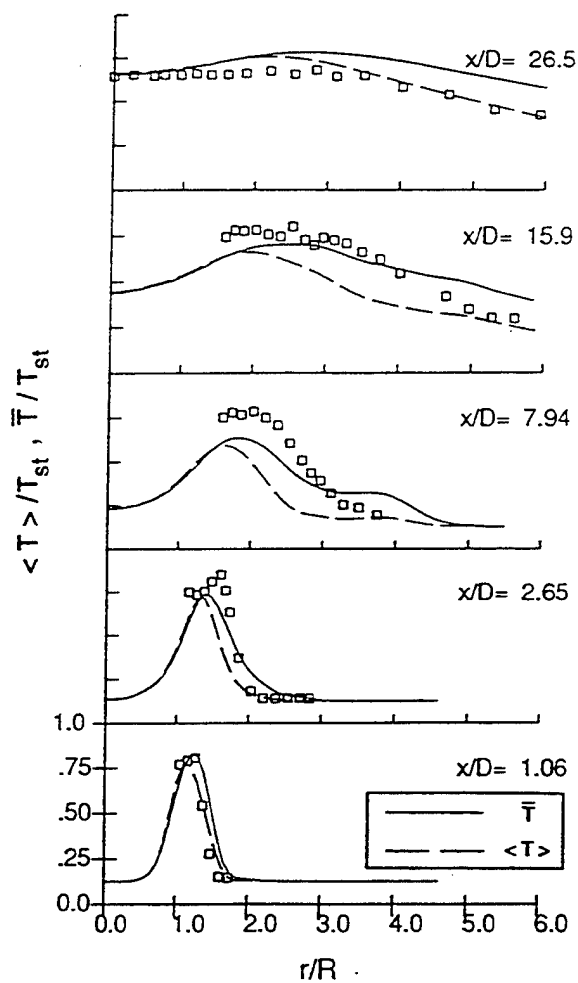


Figure 8-3. Computed profiles of Favre-averaged mean temperature ($\langle T \rangle$) and Reynolds-averaged mean temperature (\bar{T}) compared against data (symbols) for the nonswirling case (Case 2).

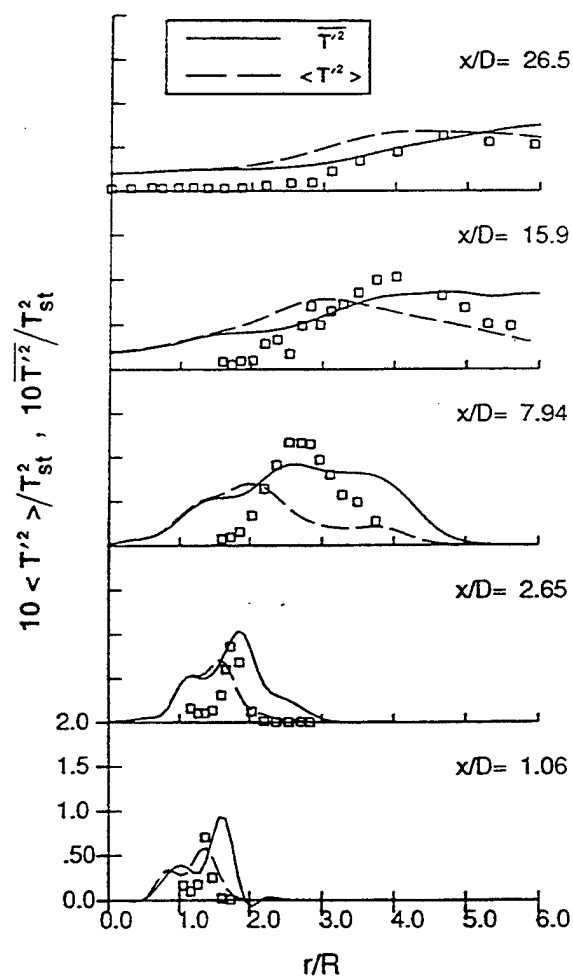


Figure 8-4. Computed profiles of Favre-averaged temperature variance ($<T'^2>$) and Reynolds-averaged temperature variance ($\overline{T'^2}$) compared against data (symbols) for the nonswirling case (Case 2).

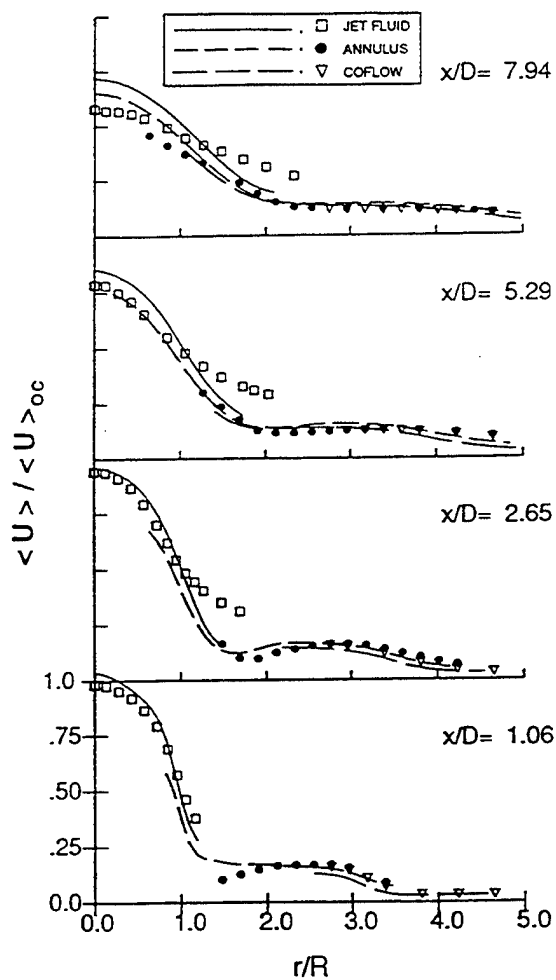


Figure 8-5. Radial profiles of computed conditional mean axial velocity (lines) compared against data (symbols) for the 30 degree swirl case (Case 3).

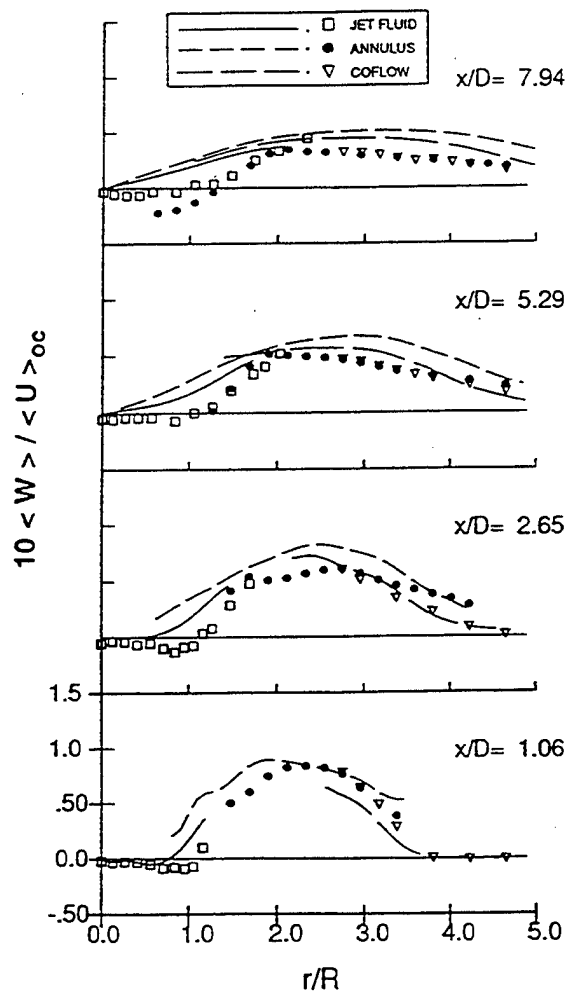


Figure 8-6. Radial profiles of computed conditional mean tangential velocity (lines) compared against data (symbols) for the 30 degree swirl case (Case 3).

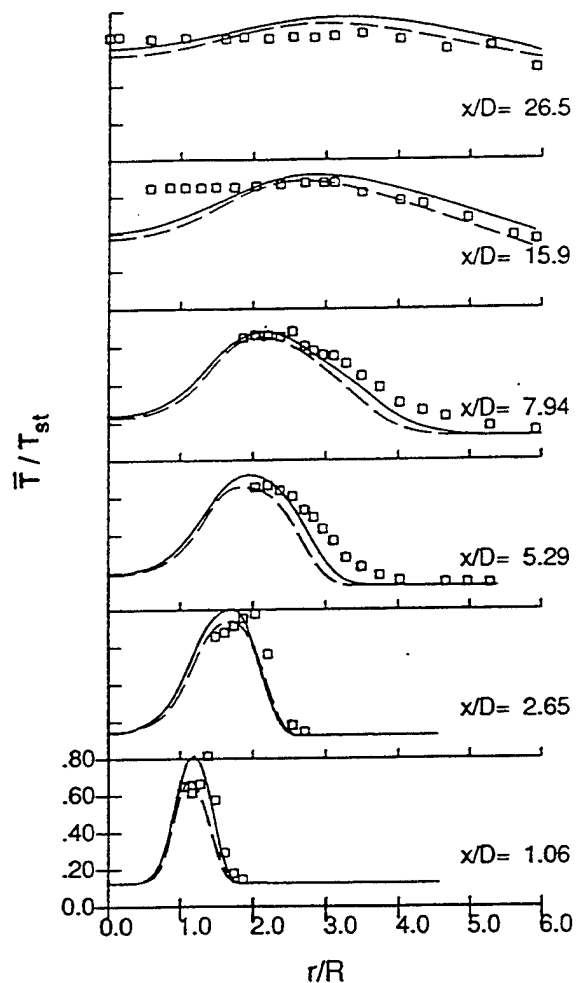


Figure 8-7. Computed profiles of Reynolds-averaged mean temperature with (solid lines) and without (dotted lines) the inclusion of molecular diffusion compared against data (symbols) for the 30 degree swirl case (Case 3).

temperature peaks are lower at corresponding axial stations than in Case 2 (see Figure 8-3) and the profiles show more spreading indicative of enhanced turbulent mixing due to swirl. Also, at the corresponding axial stations the peaks are located at a slightly larger radial distance for Case 3 than for Case 2 due to the centrifugal action of the swirl. These observations are consistent with the observations made for the mean axial velocity profiles shown in Figure 8-5.

Figure 8-7 also includes the calculated profiles of \bar{T} without the explicit inclusion of molecular diffusion in the computations. Overall, the inclusion of molecular diffusion improves the agreement of the computations with the data. It is interesting to note that the computed mean and other velocity statistics were nearly the same with or without the inclusion of molecular diffusion although the mean temperature profiles (and other scalar statistics) changed. This indicates that small changes in the local heat release rate do not have a very strong influence on the hydrodynamics of the flames studied.

The measured and calculated temperature variances are shown in Figure 8-8. The comments regarding the inner peak in the computations made in conjunction with Figure 8-4 are more clearly illustrated in this figure. The magnitudes and shapes of the outer peaks are well predicted, although the predictions are slightly higher for the downstream locations $x/D = 7.94$.

Figures 8-5 through 8-8 show that the peak temperature (i.e., the flame) still lies at the outer edge of the shear layer between the jet and the annulus flows, but the broadening of the temperature peaks show that the flame is spreading into the shear layer more than in the nonswirling case. Overall, the computations and data (Figures 8-5 through 8-8) show enhanced mixing and spreading of the flame due to swirl compared to Case 2. The computed velocity and temperature statistics are in good agreement with the data, and the spreading and decay of the mean and swirl velocities are well predicted.

Figures 8-9, 8-10, and 8-11 show the conditional mean axial and swirl velocities and the unconditional Reynolds-averaged temperature, respectively at two axial stations for the 45 deg swirl case (Case 4). The axial and swirl velocity data indicate much higher mixing and spreading than the 30 deg swirl case (Case 3) as expected. The location of the peak temperature (see data in Figure 8-11) at $x/D = 2.65$ is at a significantly larger distance for Case 4 ($r/R \sim 2.5$) than for Case 3 ($r/R \sim 2.0$), while at $x/D = 7.94$ the peak temperature is located at nearly the same location ($r/R \sim 2.15$) for both cases. This indicates that the peak flame location expands to a larger radius in the near nozzle region for the 45 deg swirl case, but moves back (indeed contracts) to about the same location as for the 30 deg swirl case, at the downstream locations. This expansion near the nozzle is due to the larger centrifugal force in the higher swirl case

forcing both the annular swirling air and the hydrogen jet to a larger radius (the volume expansion of the annulus air due to combustion induces a radial velocity in the annular jet for all the cases). Indeed, the data for mean radial velocities at the initial plane (presented in Refs. 8-7 and 8-8) show that the outer edge of the hydrogen jet and the bulk of the annulus air have outward mean radial velocities of approximately 5 m/s for Case 4 and about 2 m/s for Case 3. Evidence of this movement can be seen in the apparent radial shift in the corresponding radial profiles of the mean axial and tangential velocities at $x/D = 2.65$ in Figures 8-9 and 8-10.

The centrifugal motion, coupled with the volume expansion of the annular air in the flame zone, causes the data rate for the annulus air seed to be low enough that data cannot be collected in a region between the hydrogen jet and the annulus air near the nozzle exit. These voids in the data can be noticed in Figures 8-9 and 8-10 (up to $x/D = 2.65$ for Case 4) and in Figures 8-5 and 8-6 (up to $x/D = 1.06$ for Case 3). The radial velocities in the bulk of the annular swirling jet in the nonreacting cases were less than 2 m/s and directed inward [8-6, 8-9] and hence did not cause such a problem for LDV measurements.

Another interesting observation is that although the initial swirl velocity is higher for Case 4 than Case 3, the peak swirl velocity of the annular air is approximately the same for the two cases at $x/D = 2.65$ as dictated by the conservation of angular momentum, due to the larger radial movement of the annular air in the former case.

The computations for Case 4 (Figures 8-9, 8-10, and 8-11) are in good agreement with data and predict the jet spreading, the decay of the swirl, and the temperature profile well for $x/D = 7.94$ and beyond. There are some significant discrepancies between the data and the computations, especially in the mean temperature profile for $x/D = 2.65$. The preceding discussion of the strong swirl and radial velocity and the suggestion by the data in Figure 8-9 that the flow is tending towards recirculation indicate that the boundary layer assumptions are seriously violated in the near-nozzle region and, hence, the calculated radial and mean pressure gradients are in error. Therefore, it is not reasonable to expect that the boundary layer algorithm will accurately calculate the flow in this region. Some evidence of this is also seen in Figures 8-5 and 8-6 at $x/D = 1.06$, but the problem is more severe for the 45 deg swirl case. The large density ratio between the fuel/burnt gas and the cold air also compounds the problem. It is emphasized that the shortcoming is not that of the pdf method, but rather it is due to the fact that the boundary layer assumptions are not valid under the conditions encountered in this region. Elliptic flow calculations with the pdf method, to be presented in the subsequent chapters, is expected to give a better agreement in the near-nozzle region. Indeed, the recomputation of the swirling jet hydrogen flames using the elliptic pdf method presented in chapter 10 shows better agreement with data in the near-nozzle region.

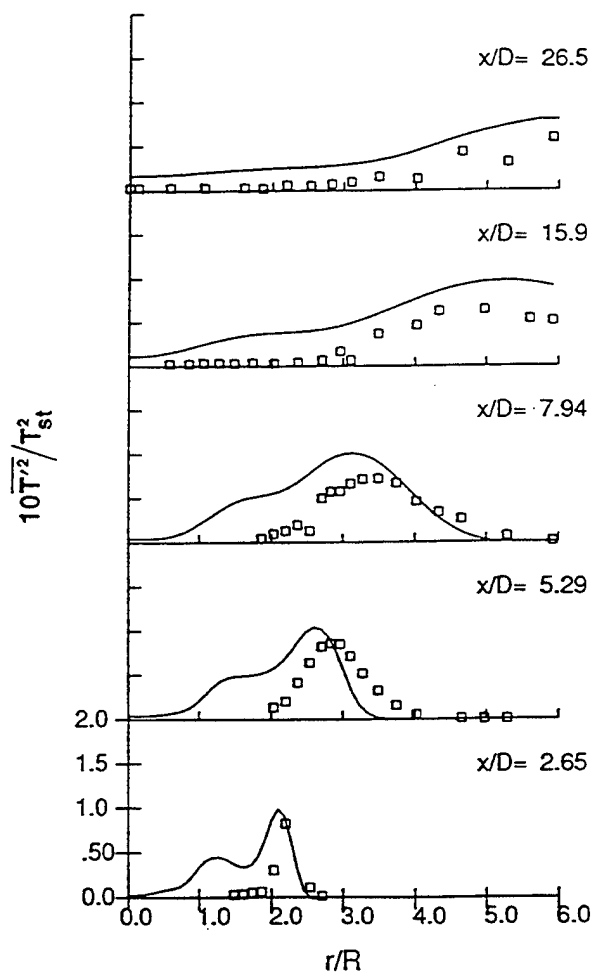


Figure 8-8. Computed profiles of Reynolds-averaged temperature variance (lines) compared against data (symbols) for the 30 degree swirl case (Case 3).

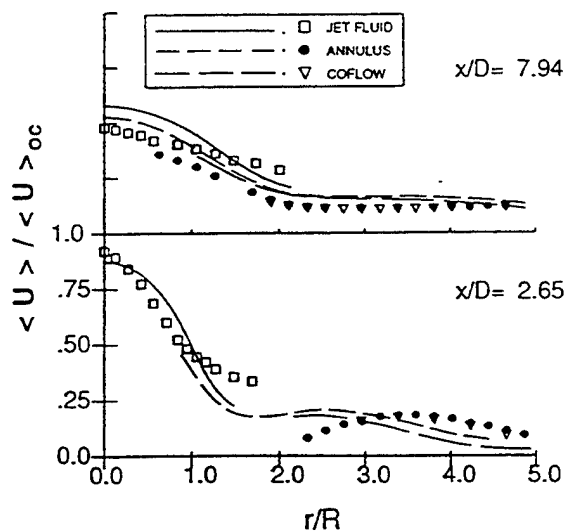


Figure 8-9. Radial profiles of computed conditional mean axial velocity (lines) compared against data (symbols) for the 45 degree swirl case (Case 4).

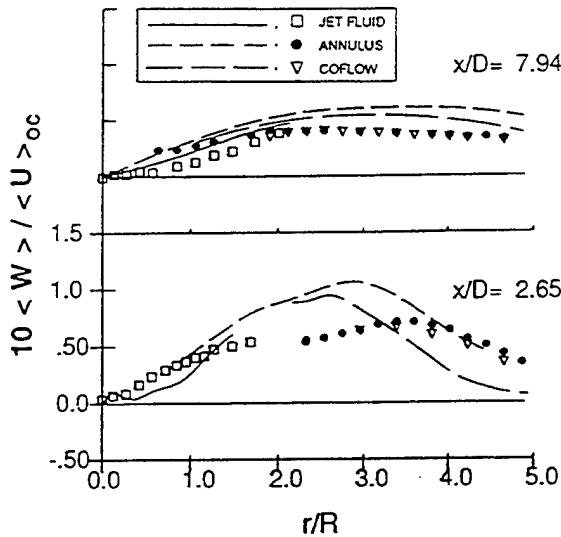


Figure 8-10. Radial profiles of computed conditional mean tangential velocity (lines) compared against data (symbols) for the 45 degree swirl case (Case 4).

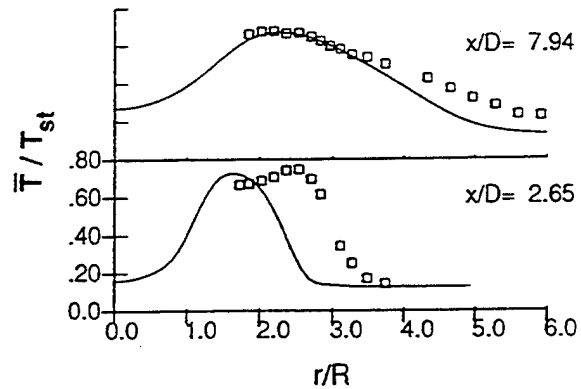


Figure 8-11. Computed profiles of Reynolds-averaged mean temperature (lines) compared against data (symbols) for the 45 degree swirl case (Case 4).

The temperature and velocity profiles for Case 4 again indicate that the peak temperature location falls at the outer edge of the shear layer between the jet and the annulus; however, it is more into the shear layer and spreads faster into the shear layer than in the two cases presented previously (compare velocity and temperature profiles at $x/D = 7.94$ for example).

Higher order turbulence correlations are now presented to compare the details of the structure of turbulence computed by the pdf method against the data. Correlations of any order, including velocity-scalar correlations (not presented here), can be extracted from the pdf solution just as velocity correlations of any order can be extracted from the LDV data. Figures 8-12 through 8-15 present sample higher order correlations in the developing region of the flame for the 30 deg swirl case (Case 2). The correlations presented are the turbulent kinetic energy (k), the turbulent shear stress ($\langle uv \rangle$), the triple correlation ($\langle u^2 v \rangle$), and the fourth-order correlation ($\langle v^4 \rangle$), respectively. The correlations are in very good agreement with the data in terms of

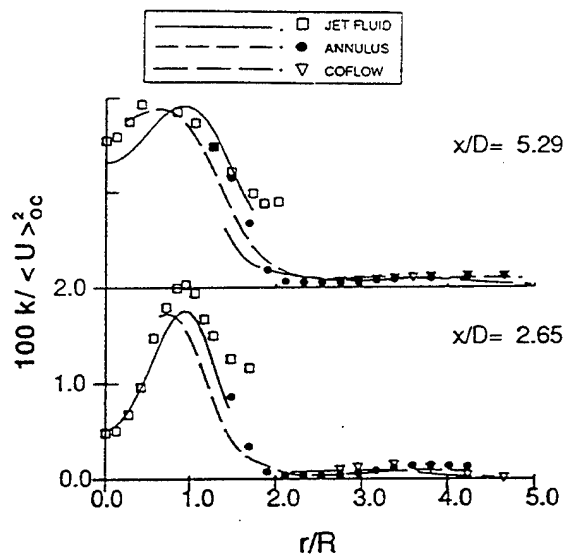


Figure 8-12. Radial profiles of computed conditional turbulent kinetic energy (lines) compare against data (symbols) for the 30 degree swirl case (Case 3).

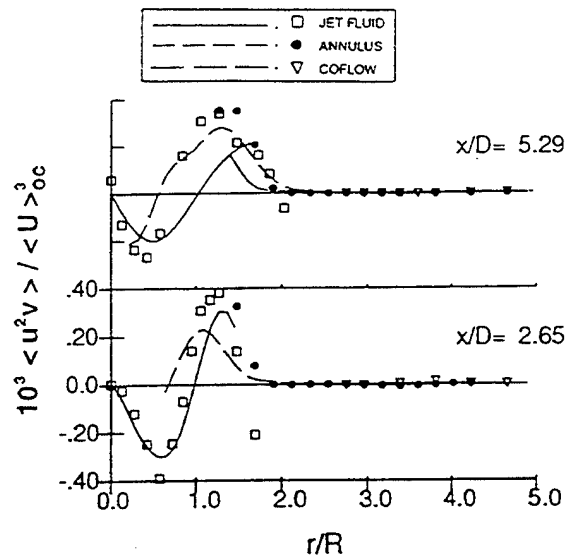


Figure 8-13. Radial profiles of computed conditional turbulent shear stress (lines) compared against data (symbols) for the 30 degree swirl case (Case 3).

magnitudes and trends, and, as in the nonreacting case, show significant differences between the statistics of the fluids originating from different streams, especially between the jet and the annulus fluids. These differences diminish as the flow proceeds downstream and the streams mix. It should be noted that the conventional second-order closure models compute only up to the second-order correlations and the third-order correlations are modeled. Given that the higher order correlations are both difficult to measure and compute to a high level of accuracy, the good agreement between the data and computations observed for all quantities validate the computations and the data.

The cases took from approximately 15 minutes (for Case 2) to 23 minutes (for Case 4) of CPU time on an IBM RS6000/370 workstation. The nominal number of particles used in the simulations were 110,000 and the number of spatial bins used (for averaging) was 110. Calculations with 300,000 particles yielded nearly identical results. The number of basis functions used for the spline fits was 20.

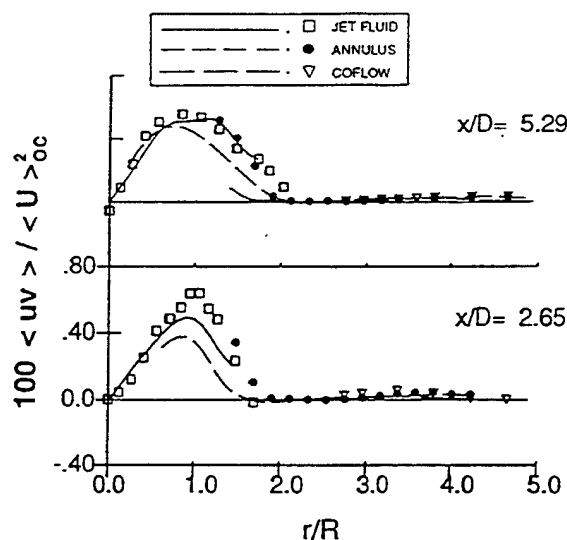


Figure 8-14. Radial profiles of computed conditional triple correlation $\langle u^2 v \rangle$ (lines) compared against data (symbols) for the 30 degree swirl case (Case 3).

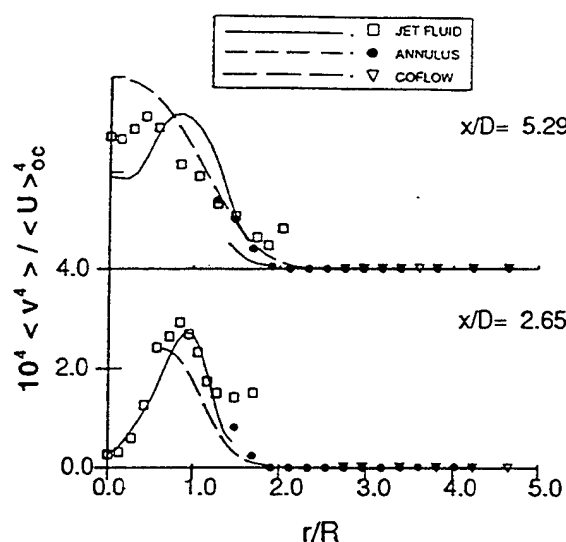


Figure 8-15. Radial profiles of computed conditional fourth moment $\langle v^4 \rangle$ (lines) compared against data (symbols) for the 30 degree swirl case (Case 3).

8.7 Summarizing Remarks

Computations using the joint velocity-frequency-scalar pdf method as well as detailed benchmark quality measurements have been presented for nonswirling and, for the first time, swirling hydrogen jet diffusion flames. The measurements and computations reported include velocities (mean and higher moments up to fourth order) conditional upon the jet of origin of the fluid and temperature (mean and variance) near the burner exit and downstream locations up to 26.5 jet diameters. The velocities were measured with a three-component LDV and the temperature was measured using CARS.

The hydrogen flame, due to the low value of the stoichiometric mixture fraction for hydrogen/air combustion, is stabilized at the outer edge of the shear layer between the hydrogen and the surrounding air jet as expected. As the swirl in the air jet increases, the location of the peak temperature moves radially outward along with the shear layer but still remaining at the outer

edge of the shear layer. The flame broadens and spreads more into the shear layer due to enhanced mixing due to swirl. Other relative features of the flames have been studied and discussed in detail.

The computations are in good agreement with data including those for fourth-order turbulent correlations, demonstrating and further validating the ability of the pdf method to accurately compute the details of the flow and the local turbulence structure. An important finding is that although Favre (density-weighted) averages are recommended and typically used in the computation of reacting flows, the conventional Reynolds average is the appropriate average to compare against temperature data from CARS.

A relatively simple boundary-layer algorithm with a relatively simple model for thermochemistry used for the computations provided a remarkably good agreement with velocity and temperature data, except very close to the nozzle for the high swirl case where the boundary-layer assumptions are not likely to be valid. Given the current agreement with the data, further complexities in the modeling of the thermochemistry such as multistep chemistry, differential diffusion of species, and nonunity Lewis number effects may not be warranted for the flames studied. The computations took a maximum of 23 minutes on an IBM RS6000/370 workstation.

REFERENCES

- 8-1. Anand M. S, Takahashi, F., Vangsness, M. D., Durbin, M. D., Schmoll, W. J., "An Experimental and Computational Study of Swirling Hydrogen Jet Diffusion Flames," ASME Paper 95-GT-307. To be published in the Transactions of the ASME.
- 8-2. Takahashi, F., Durbin, M. D., Schmoll, W. J., and Vangsness, M. D., 1994, Report UDR-TR-94-115, University of Dayton, Dayton, Ohio.
- 8-3. Takahashi, F., Vangsness, M. D., Schmoll, W. J., and Durbin, M. D., 1994, Report UDR-TR-94-89, University of Dayton, Dayton, Ohio.
- 8-4. Bilger, R. W., 1982, AIAA Journal, 20, No. 7.
- 8-5. Takahashi, F., Durbin, M. D., and Vangsness, M. D., 1993, Report UDR-TR-93-88, University of Dayton, Dayton, Ohio.
- 8-6. Takahashi, F., Vangsness, M. D., and Durbin, M. D., 1993, Report UDR-TR-93-22, University of Dayton, Dayton, Ohio.
- 8-7. Takahashi, F., Durbin, M. D., Schmoll, W. J., and Vangsness, M. D., 1994, Report UDR-TR-94-116, University of Dayton, Dayton, Ohio.

- 8-8. Takahashi, F., Durbin, M. D., Schmoll, W. J., and Vangsness, M. D., 1994, Report UDR-TR-94-117, University of Dayton, Dayton, Ohio.
- 8-9. Takahashi, F., Vangsness, M. D., and Belovich, V. M., 1992, AIAA-92-0580.

9. BACKWARD FACING STEP FLOW

9.1 Overview

The algorithms to determine the mean pressure field for elliptic flow calculations with the pdf method (sections 5.2 and 5.3) are applied and validated. Previous computations of elliptic flows with the pdf method have involved accompanying conventional finite-volume based calculations to provide the mean pressure field. The algorithms developed and here permit the mean pressure field to be determined within the pdf calculations. The pdf method incorporating the pressure algorithm is applied to the flow over a backward-facing step. The results are in very good agreement with data for the reattachment length, mean velocities, and turbulence quantities including triple correlations.

9.2 Background

As discussed in section 2.3. there are no theoretical limitations for applying the pdf method for complex (2-D or 3-D) elliptic flows. However, a suitable algorithm for extracting the mean pressure field within the pdf solution algorithm is needed. A pdf method for elliptic flows was first demonstrated by Anand et al. [9-1]. In this method, the Monte Carlo (MC) calculations for the pdf are combined with conventional finite-volume (FV) calculations for mean fields (Ref. 11). The mean pressure field and the turbulent time scale are supplied to the MC calculations by the FV calculations. In turn, the MC calculations supply to the FV calculations the Reynolds stresses extracted from the pdf solution, thereby avoiding the use of conventional turbulence models. This combined algorithm exploits the advantages of both methods to yield an economical algorithm for pdf calculations of complex elliptic flows. This method was intended to demonstrate the feasibility of pdf calculations for such flows.

However, for more complex flows, especially variable density and reacting flows with fast or finite-rate multi-step chemistry, the coupling between the two methods becomes quite complex and it becomes more difficult to fully exploit the advantages of the pdf method. Therefore, it is desirable to perform pdf calculations independently, without recourse to FV calculations. This chapter describes the application of two algorithms developed through which pdf calculations are performed independently and economically (in terms of computer resources required) for

complex elliptic flows. In addition, the treatment of wall boundaries is included in the calculations. The method is applied to a sample elliptic flow, namely the recirculating flow behind a backward-facing step and compared against data of Pronchick and Kline [9-2].

9.3 Test Case and Initial Conditions

The schematic of the flow is shown in Figure 9-1. The step height is H and the centerline mean axial velocity in the channel is U_{ref} . The fluid used in the experiments was water, and the Reynolds number based on H and U_{ref} was approximately 12,000.

The inlet velocity pdf was prescribed to be joint-normal with the means and covariances of the velocity components being those of fully developed turbulent flow in the inlet channel as calculated by the k-e model. The inlet turbulent kinetic energy k is distributed into the three components according to $k = \langle u^2 \rangle = 2\langle v^2 \rangle = 2\langle w^2 \rangle$. The inlet shear stress $\langle uv \rangle$ is prescribed to be linear with a value of zero at the centerline of the inlet channel and a peak value of $0.03k$ near the wall of the inlet channel. The turbulence levels at the inlet have little effect on the final results since most of the shear and turbulence production occurs in the recirculation zone within the solution domain. The initial pdf in the solution domain was set equal to the inlet pdf and the initial mean pressure was zero everywhere.

Computations were performed using both the elliptic flow pressure algorithms described in Chapter 5. The latest models for velocity and frequency available at the time that these algorithms were developed, were used. Results are presented in the next two subsections.

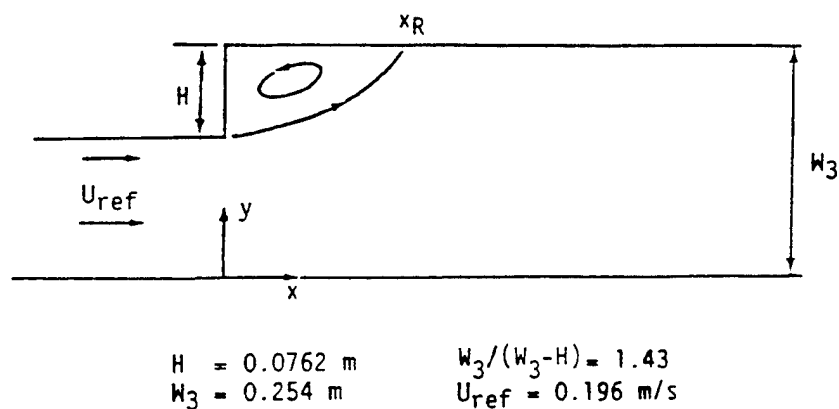


Figure 9-1. Schematic of the flow considered. Backward-facing step studied experimentally by Pronchick and Kline (1983).

9.4 Computations with Pressure Algorithm I

9.4.1 Computational Details

The pressure algorithm described briefly in section 5.2 is applied and validated. There are considerable details in the formulation and implementation of the algorithm. For the sake of brevity they are not presented here. The reader is referred to Anand et al. [9-3] for details.

The simple Langevin model (SLM I) is used for the velocities. The stochastic turbulence frequency models were still being developed at the time the PA I algorithm was developed and applied. Hence the mean turbulence frequency was supplied to the pdf calculations in the following manner. The turbulent frequency ($\langle\omega\rangle = \langle\epsilon\rangle/k$, where $\langle\epsilon\rangle$ is the mean dissipation rate of k) is calculated at each step from the current value of k by

$$\langle\omega\rangle = k0.5/l \quad , \quad (9.1)$$

where the turbulent length scale l is supplied from the k - ϵ solution of Ref. [9-1] (see Eq. 19), and is held constant throughout the calculations:

$$l = k^{1.5}/\langle\epsilon\rangle \quad . \quad (9.2)$$

The choice of supplying l was preferred over the choices of supplying $\langle\omega\rangle$ or $\langle\epsilon\rangle$ from the k - ϵ solution since the profiles of l were nearly uniform across the flow (approximately 0.02 13) except near the walls where the values decrease. This way, the l used in the calculations (Eq. 9.1) would be more consistent with the current values of k .

The number of particles used in the simulation was 60,000. The computations were performed for 250 steps with pressure updates every 20 steps and the pressure relaxation factor of 0.8. The time interval for each step was $0.3 H/U_{\text{ref}}$ (see Figure 9-1 for the definition of H and U_{ref}). This time interval was less than one-tenth of the turbulent time scale over most of the flow domain except for small regions near the wall where it was between one-fifth and one-tenth of the turbulent time scale. The calculations reached a steady-state around the 200th step. The final results shown here (except for mean pressure which is taken from the last step) are calculated from spline-fits to sums formed over 50 steps after steady-state has been reached. This has an effect similar to having 3 million ($60,000 \times 50$) particles in the simulation thereby minimizing the statistical error in the results which is inversely proportional to the square root of the number of particles.

9.4.2 Results and Discussion

The computed reattachment length of 6.5H is in good agreement with the experimentally observed reattachment length (x_{RE}) of 6.75H. It should be noted that this agreement is better than achieved by any finite-volume calculations.

The results for mean velocities and various turbulent quantities are shown in Figure 9-2 through 9-10. The results are shown for different axial stations normalized with respect to the experimental reattachment length:

$$x^* = (x - x_{RE}) / x_{RE} . \quad (9.3)$$

Overall, the results are in excellent agreement with data both in magnitude and qualitative trends. It is noteworthy that the turbulence quantities, especially the third moments (which cannot be calculated with the k- ϵ model, and are modeled in second-moment closures) are in good agreement with data. It is also to be noted that the turbulence quantities are an order of magnitude lower than the reference velocity U_{ref} .

The contours of the calculated mean pressures are shown in Figure 9-11. The magnitudes and shapes of the contours are comparable to those obtained from previous calculations with the k- ϵ model and combined FV/MC pdf method [9-1]. This fact, in conjunction with the accurate prediction of the mean velocity field, shows that the pressure algorithm is working satisfactorily.

Approximately 1.3 Megawords of storage was required for the computations. The total CPU time required for the computations (250 steps) on a CRAY XMP-22 was approximately 11 minutes (about 6 minutes on an IBM RS6000/370 and about 3 minutes on a CRAY C90). This reflects an order of magnitude reduction over the estimated time it would have taken with the initial straight forward implementation of the algorithm. Nearly 55 percent of the computational time is spent in computations related to the pressure algorithm, namely forming sums and splines for pressure updates and velocity corrections, in spite of limiting the frequency of pressure updates and improving the efficiency of the spline-fitting routines. However, the total computational time of approximately 11 minutes and the storage required are still very modest for pdf calculations of an elliptic flow.

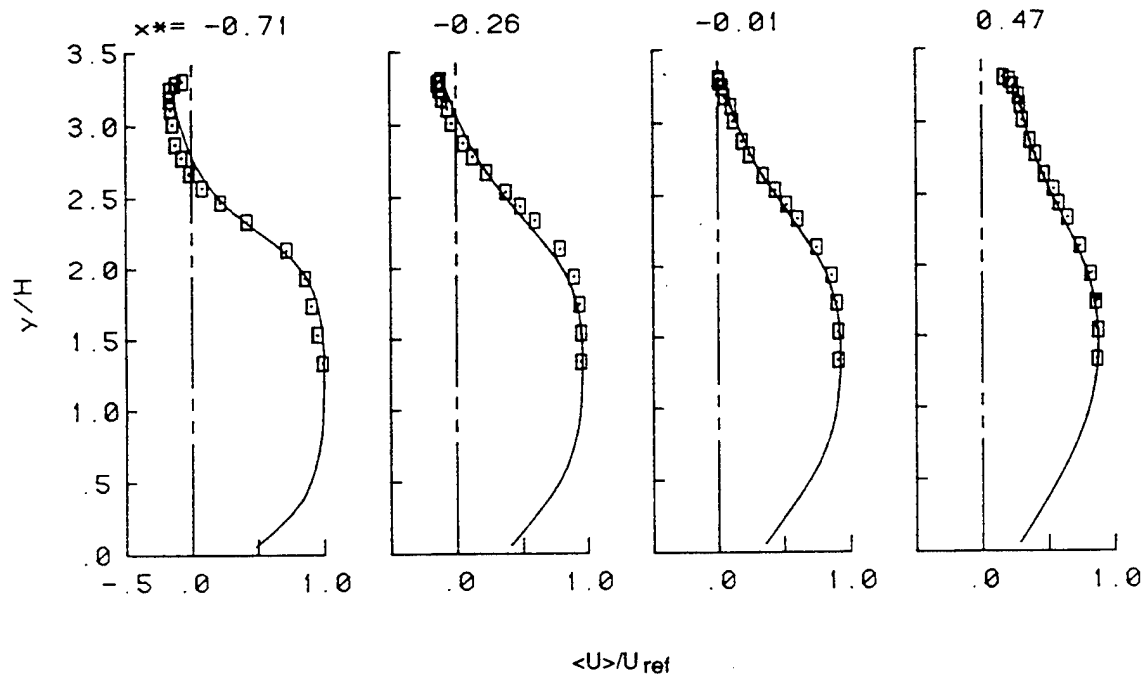


Figure 9-2. Computed mean streamwise velocity profiles (lines) compared against data (symbols).

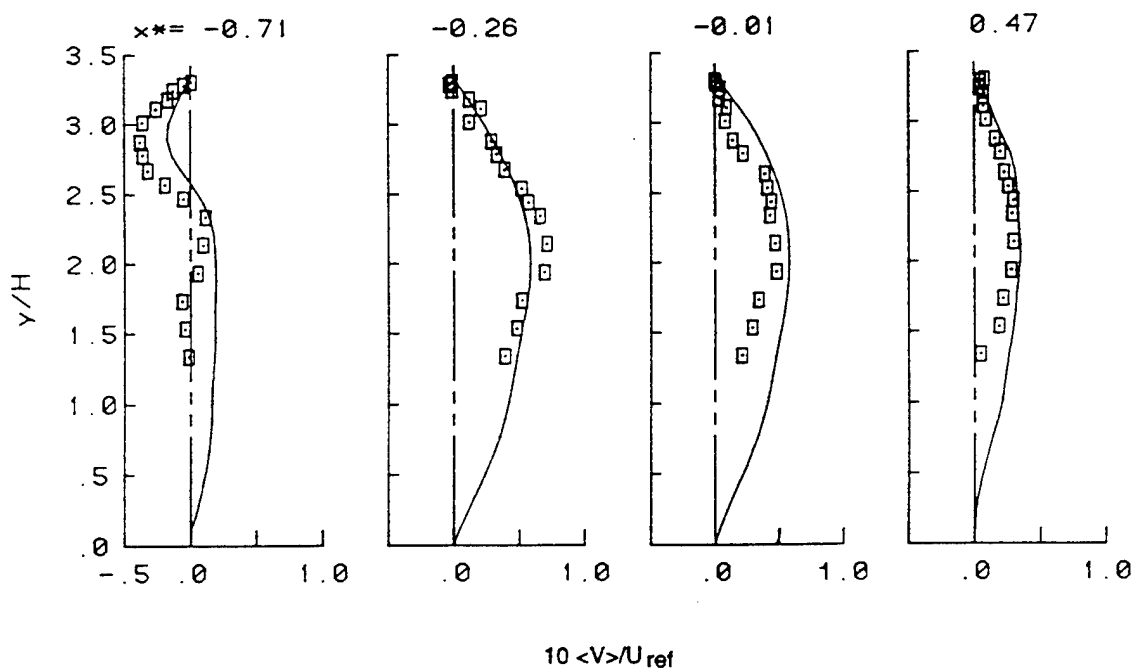


Figure 9-3. Computed mean transverse velocity profiles (lines) compared against data (symbols).

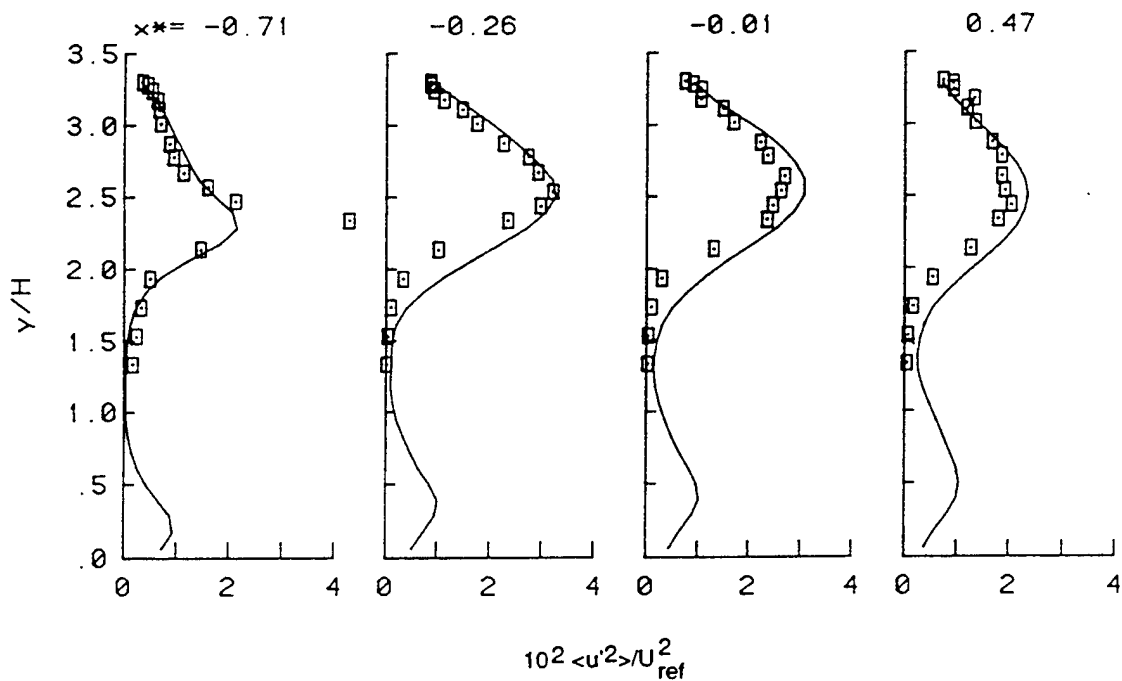


Figure 9-4. Computed streamwise velocity variance profiles (lines) compared against data (symbols).

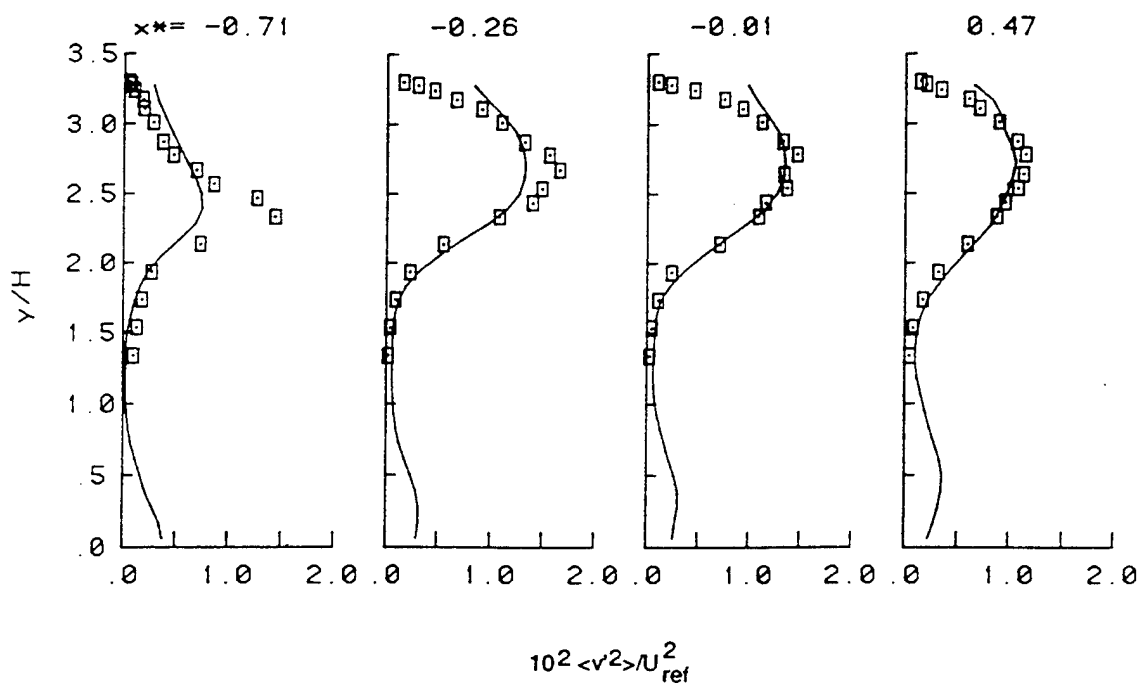


Figure 9-5. Computed transverse velocity variance profiles (lines) compared against data (symbols).

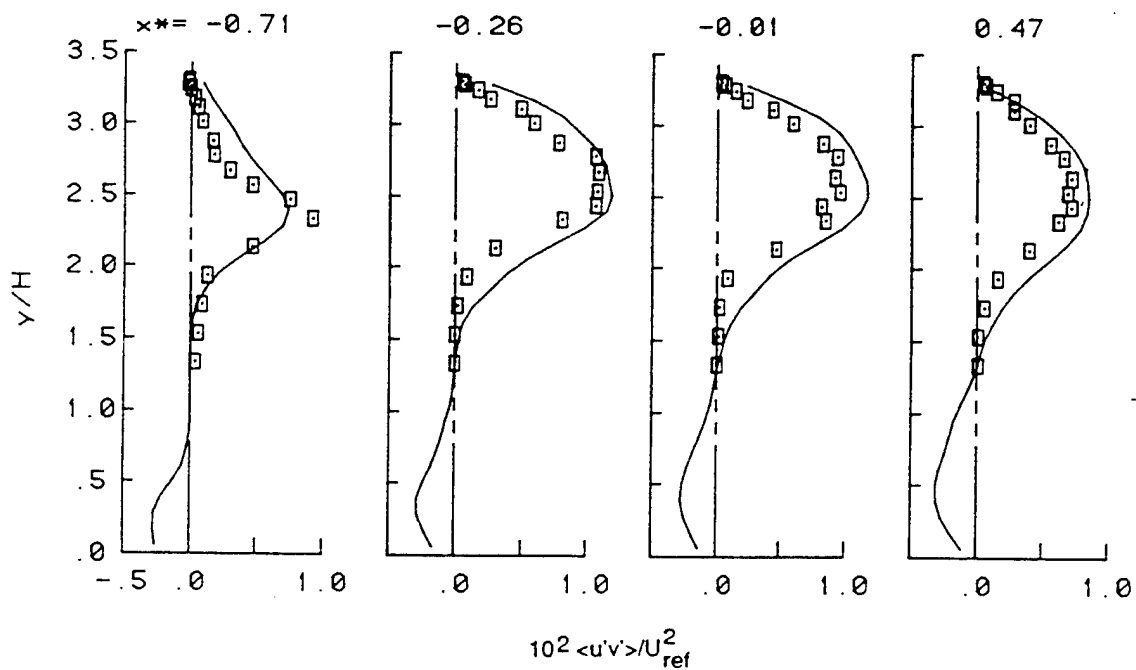


Figure 9-6. Computed shear stress profiles (lines) compared against data (symbols).

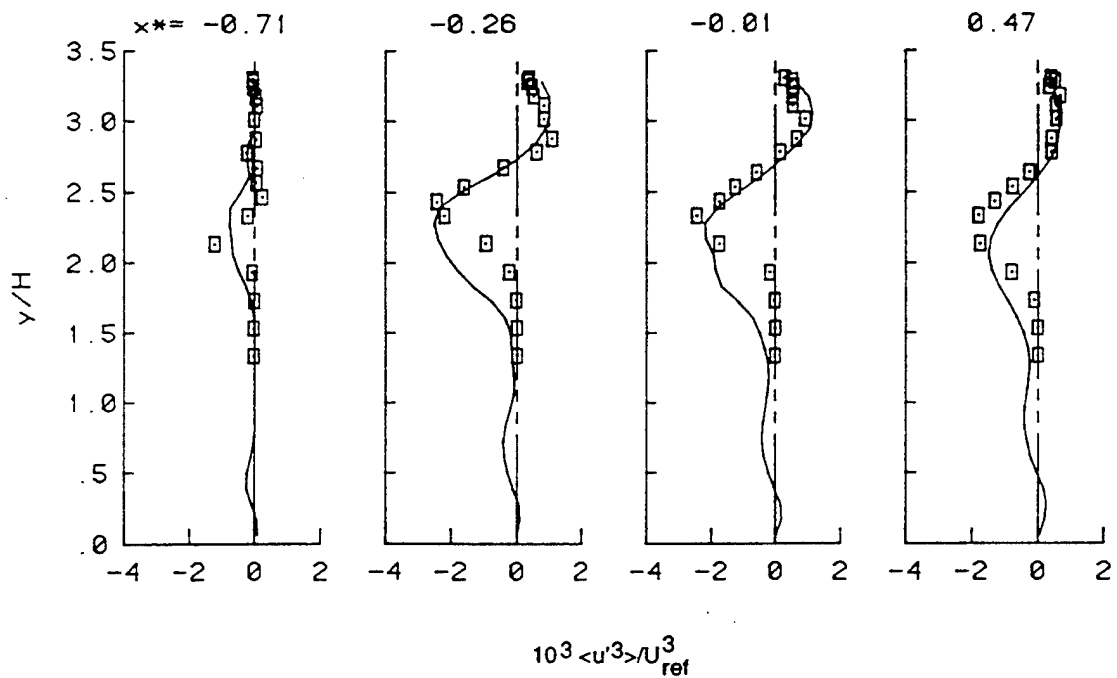


Figure 9-7. Computed $\langle u^3 \rangle$ profiles (lines) compared against data (symbols).

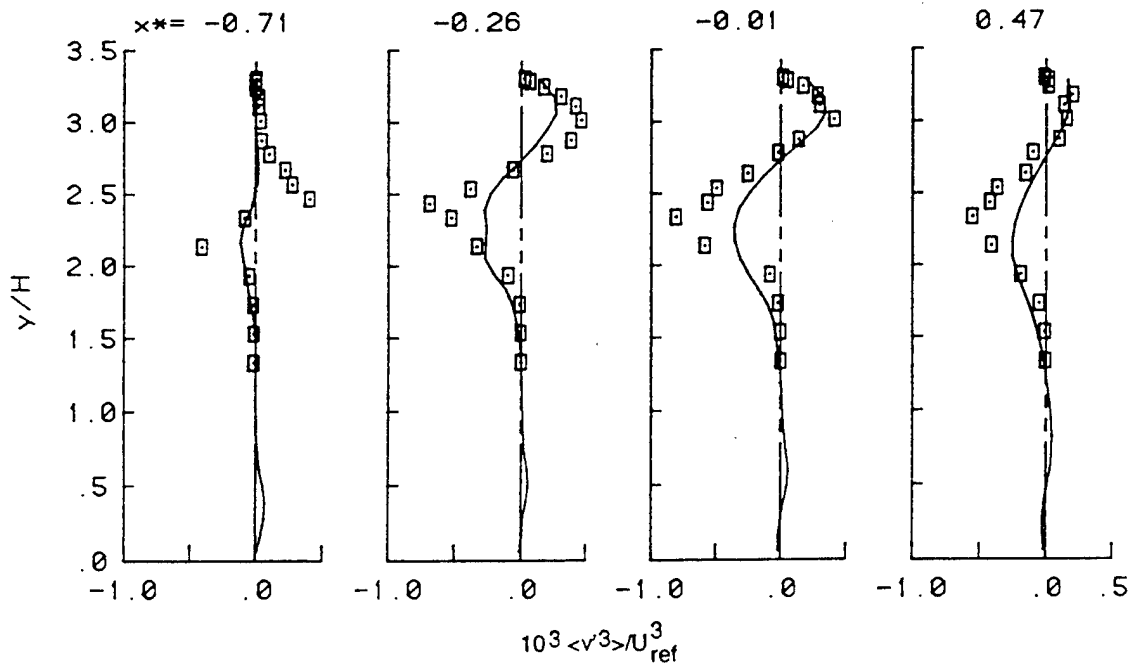


Figure 9-8. Computed $\langle v^3 \rangle$ profiles (lines) compared against data (symbols).

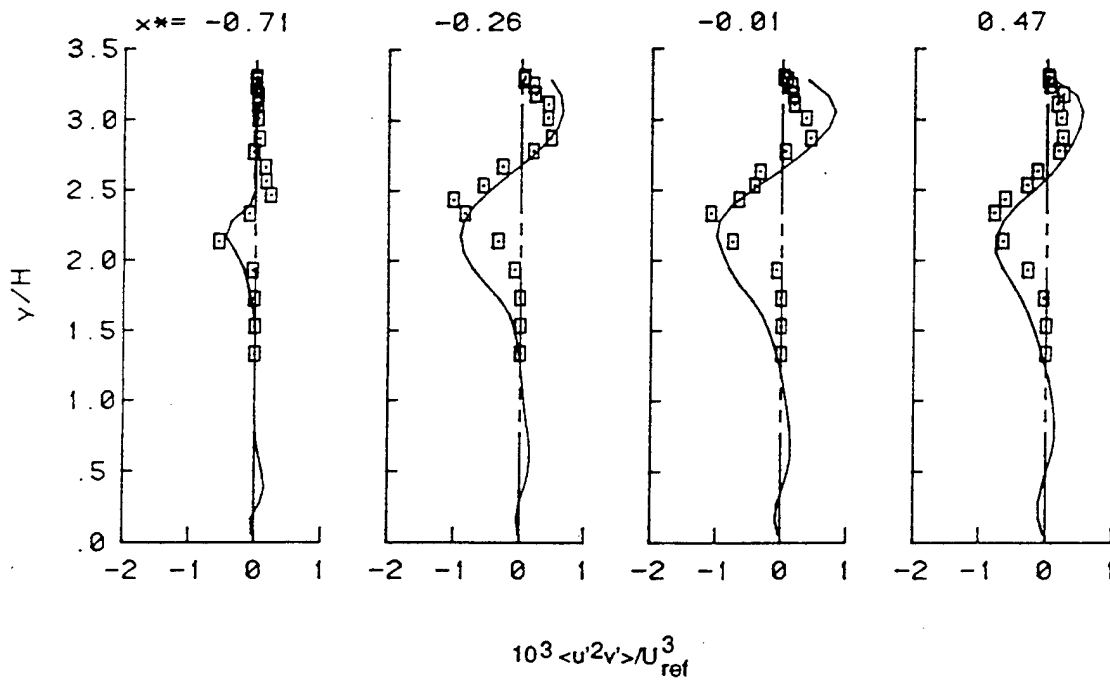


Figure 9-9. Computed $\langle u^2 v \rangle$ profiles (lines) compared against data (symbols).

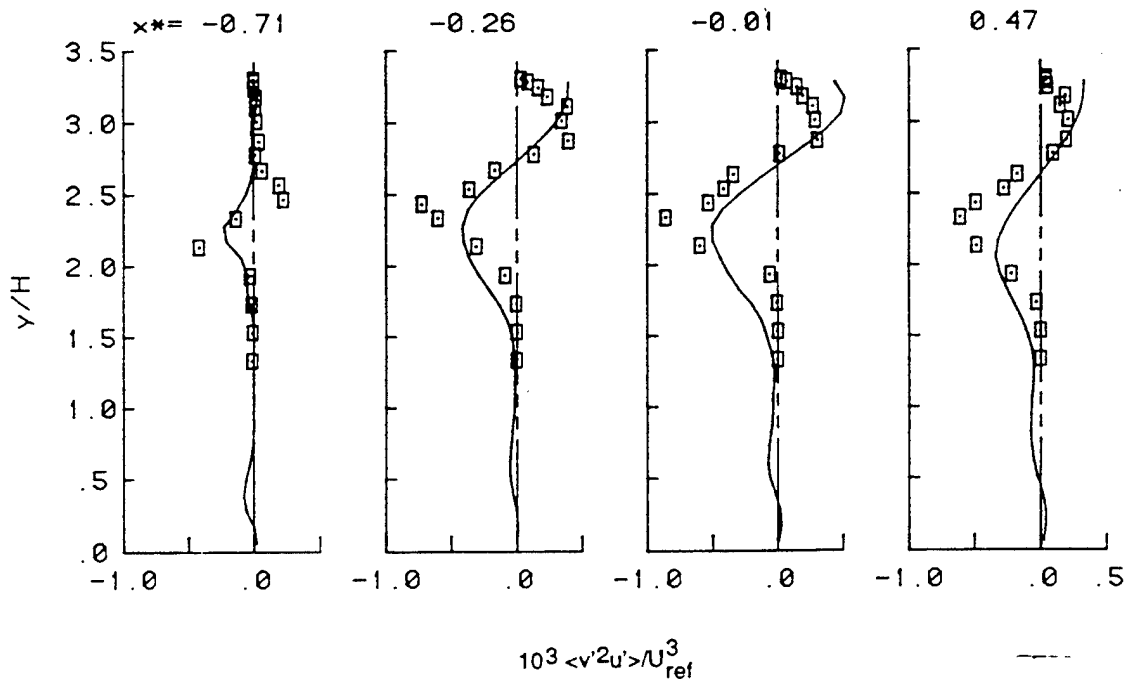


Figure 9-10. Computed $\langle v^2 \rangle$ profiles (lines) compared against data (symbols)

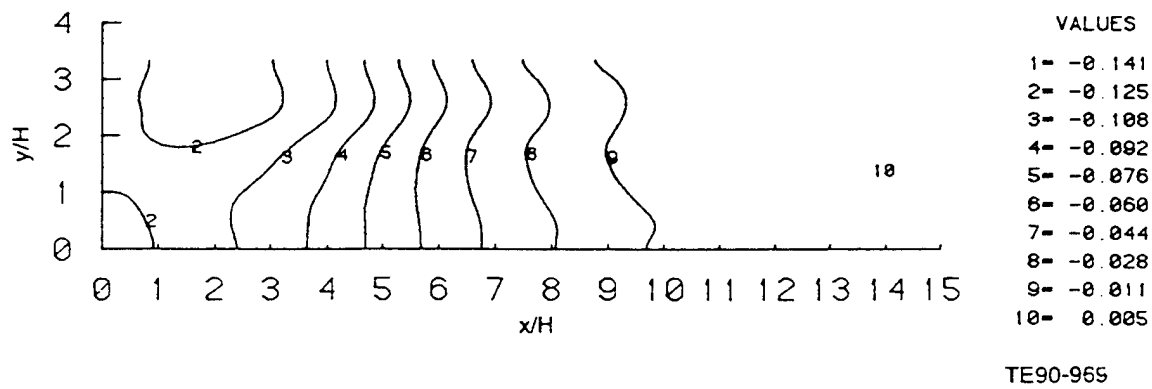


Figure 9-11. Computed contours of mean pressure (normalized by ρU_{ref}^2)

9.4.3 Summarizing Remarks

An algorithm to determine the mean pressure in steady-state constant or variable-density elliptic flow calculations with the pdf method has been developed and implemented economically. The algorithm and the pdf calculations have been tested for a sample recirculating flow; namely the flow behind a backward-facing step.

The computed results are in excellent agreement with data for the mean velocity field and various turbulence quantities including triple corrections. The computed reattachment length is in excellent agreement with the experimental value. These comparisons have served to validate the pressure algorithm and its implementation.

9.5 Computations with Pressure Algorithm II

The backward facing-step flow was also computed using the newer pressure algorithm (PA II, section 5.3). As explained in that section, the newer algorithm is more robust and is easier to extend to complex geometry and body-fitted grids. The models used included the latest frequency model (SFM II) and the corresponding velocity model (SLM II). The results (not shown here) were nearly the same as the results presented in the previous section (Figures 9-2 through 9-11) and they were in excellent agreement with data. The computed reattachment length of $6.77H$ was in excellent agreement with the experimentally observed reattachment length (x_{RE}) of $6.75H$.

These results validate the new pressure algorithm and the models for a constant-density flow. The validation for swirling, recirculating and reacting flows is presented in the next chapter.

REFERENCES

- 9-1. M. S. Anand, S. B. Pope, and H. C. Mongia, "A PDF Method for Turbulent Recirculating Flows," U. S.-France Joint Workshop on Turbulent Reactive Flows, Rouen, France, 6-10 July 1987. Also in *Turbulent Reactive Flows, Lecture Notes in Engineering*, **40**, Springer-Verlag, pp 672-693, 1989.
- 9-2. S. W. Pronchick and S. J. Kline, "An Experimental Investigation of the Structure of Turbulent Reattaching flow Behind a Backward-Facing Step," Report MD-42, Stanford University, Stanford, California, 1983.
- 9-3. M. S. Anand, S.B. Pope and H.C. Mongia, "Pressure Algorithm for Elliptic Flow Calculations with the PDF method," *CFD Symposium on Aeropropulsion*, NASA CP-3078, pp 347-362, 1990.

10. SWIRLING AND RECIRCULATING FLOW COMBUSTORS

10.1 Overview

Calculations are reported for recirculating swirling reacting flows using the joint velocity-frequency-scalar pdf method. The pdf calculations reported here are based on a newly developed solution algorithm for elliptic flows (PA II), and on newly developed models for turbulent frequency and velocity (SFM II and SLM II) that are simpler than the SFM I and RLM models used in some of the calculations reported in the previous chapters. Calculations are performed for two different gas-turbine-like swirl combustor flows for which detailed measurements were made at WPAFB. The computed results are in good agreement with experimental data. More details of the study are presented in Ref. 10-1.

10.2 Background

The present study represents the first fully self-contained pdf calculations for elliptic reacting flows and incorporates the elliptic flow solution algorithm as well as the stochastic frequency model. With a view to making the method more robust, easier to implement and affordable for complex multidimensional flows, a significantly different elliptic flow algorithm (or pressure algorithm) than PA I has been developed and implemented. The models for turbulent frequency, scalar mixing, and velocity have also been considerably simplified. (See chapters 3, 4 and 5.)

The pdf method is validated against benchmark experimental data for two gas-turbine-like swirl combustors and also compared against previous pdf solutions for one of the combustors considered.

10.3 Computational Details

10.3.1 The PDF Method -- Modeling and Solution Algorithm

As mentioned above, the PA II algorithm for pressure, the SFM II model for frequency, the SLM II model for velocity, and the IEM model for scalars are used in the study presented here. One of

of the features of the new algorithm is the use of a different (less computer intensive but more sophisticated) technique for estimating means and smoothing the profiles than the regular ensemble averaging and cubic B-splines used in the boundary-layer and PA I algorithms. In the present study, means of any functions of the independent variables are determined by a sophisticated ensemble averaging procedure (cloud-in-cell estimate using bi-linear basis functions) followed by smoothing using local linear least squares [10-2]. Additionally time-averaging, with a low time constant initially and a higher value near convergence, is used for mean quantities to further reduce the statistical error. The details of the pressure algorithm can be found in Chapter 5.3 and in Ref. [10-3].

The time increment, Δt , for each step is chosen to be a fraction ($=0.1$) of the minimum of a) the inverse of the maximum mean turbulence frequency in the computational domain or b) the minimum characteristic time for any particle to cross a computational cell based on the mean and variance of velocity in the cell. All the particles in the computation are marched with the same time increment. The particle evolution equations are integrated over the time step with an accuracy of second-order or better.

It should be noted that the models described above for velocity, frequency and scalar mixing are all being used in the joint pdf method for the first time to compute general (inhomogeneous, swirling, recirculating) turbulent reacting flows. As such the present study serves to validate the elliptic flow algorithm as well as the models used.

10.3.2 Thermochemistry

Hydrogen and methane flames are studied in the present work. A fast equilibrium chemistry model is used for the hydrogen flame calculations because the time scale for hydrogen-air reaction is very small compared to the turbulent time scale. For the hydrogen case, the only scalar variable in the calculations is the mixture fraction. Temperature is also included but is needed for output only. The mixture fraction is a conserved variable (reaction rate is zero). The density and temperature are determined as equilibrium properties from the mixture fraction.

For methane flame calculations, a general 2-step chemistry by Westbrook and Dryer [10-4] for saturated hydrocarbon fuels is used. The two steps are:





In addition to mixture fraction, two more scalar variables--namely the mass fractions of carbon dioxide and water--are included in the pdf calculations. The temperature and density are determined as functions of these three scalar variables.

For both the fast chemistry and the 2-step chemistry models, lookup tables were created to reduce the CPU requirements of the calculations. In the case of the fast chemistry, a one-dimensional table is created, and for the 2-step chemistry, a three-dimensional table is generated. For the 2-step chemistry calculations, the table is generated for a given specific time increment, Δt , used by the flow calculations ($\Delta t = 2.5 \times 10^{-5}$ s in the present calculations). In the table generation processes, the NASA CEC thermal data were used to calculate the variable specific heats and the temperature.

10.4 Results and Discussion

Results are presented for two laboratory swirl combustor configurations which have the essential flow features of gas turbine combustors, namely swirl, recirculation, large velocity gradients, turbulence and combustion. The experiments were conducted by researchers at the University of Dayton Research Institute at Wright Patterson Air Force Base, Ohio. The velocity measurements were made using a three-component laser Doppler velocimeter (LDV) and temperature measurements were made using coherent anti-Stokes Raman spectroscopy (CARS). (See chapter 8 for more details.)

10.4.1 Swirling Hydrogen Diffusion Flame

Figure 10-1 shows the schematic of the swirling jet diffusion flame combustor configuration. The test case considered had a central fuel (hydrogen) jet bulk velocity of 100 m/s, the swirling air bulk velocity of 20 m/s and the nonswirling coflow air velocity of 4 m/s. The swirler vane angle was 30 deg. and swirl number for the swirling jet, calculated from the measured velocities, was 0.382. Detailed measurements for mean velocities and turbulent correlations up to fourth order are reported (see Ref. 10-5 and references listed therein) at several downstream locations starting from the axial location $x = 1.5$ mm from the nozzle. While no species measurements were made, mean and variance of the temperature are reported at the same locations.

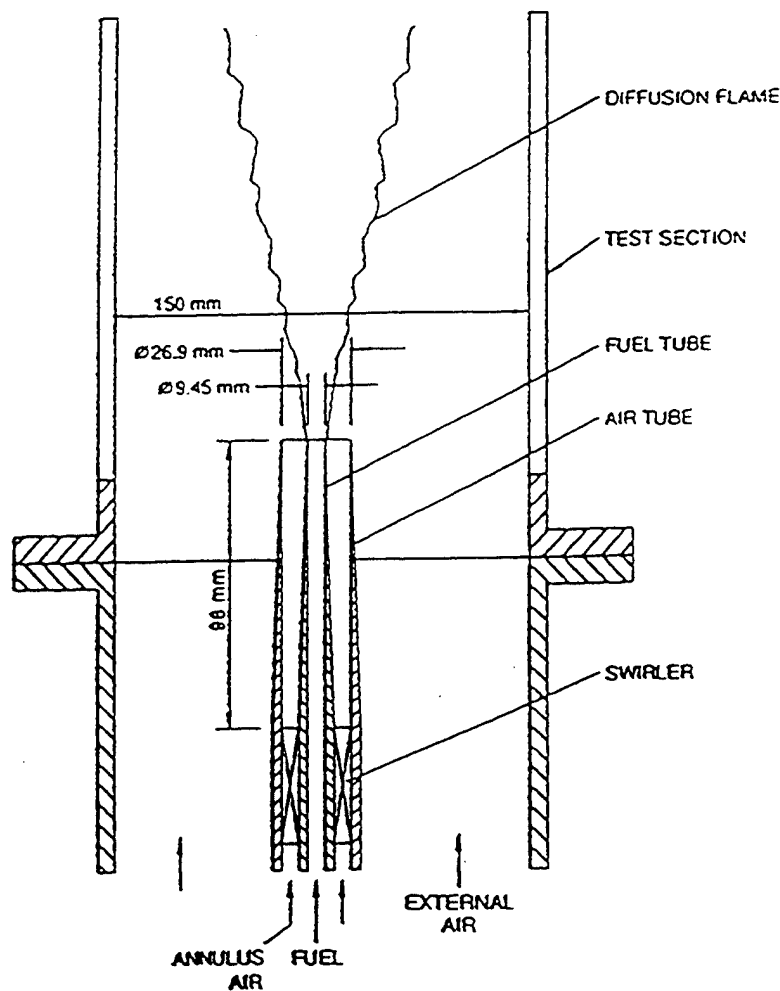


Figure 10-1. Schematic of the hydrogen swirling jet diffusion flame configuration.

The flow was previously calculated by Anand et al. [10-5] using a joint pdf method. (The study is reported in Chapter 8.) Since the flow is primarily parabolic in nature (with no recirculation), the pdf solution algorithm was based on boundary-layer assumptions with extensions for swirling flows. The method also used more sophisticated models, namely the stochastic frequency model SFM I in conjunction with the refined Langevin model RLM for velocity in which the instantaneous particle frequency rather than a mean frequency is used in the random term (see sections 3.3 and 3.4). The reason for calculating the swirling hydrogen flames again with the present method is to not only validate the method and the models but also to assess if the elliptic flow algorithm can better resolve the flow in regions where boundary-layer assumptions (e.g., neglect of axial gradients) are questionable (see discussion in section 8.5).

The present computations were performed, on an IBM RS6000/370, using a nonuniform grid (31 in x by 61 along the radius r) with about 190 particles per cell. Increasing the nominal

number of particles per cell to 290 produced nearly the same results. The inlet boundary conditions were taken from experimental data as described in Ref. 10-5. Calculations were performed for 2000 time steps.

In the figures to be presented for this case the measured mean axial velocity on the centerline at the nozzle exit, $\langle U \rangle_{OC}$, which is 130.3 m/s in this case, is used to normalize the velocity statistics. The axial distances and radius are normalized by the nozzle diameter, D ($= 9.45$ mm) and nozzle radius R ($= D/2$) respectively. The temperature results are normalized by the stoichiometric temperature, T_{St} ($= 2377$ K). For the experimental data presented, the open squares represent data conditioned on the inner fuel jet, the solid circles represent data conditioned on the swirling air jet, and the inverted triangles represent the data conditioned on the outer coflow air.

Figure 10-2 shows the convergence history for the (unnormalized) mean axial and radial velocities at the monitoring location $x/D = 10$ and $r/R = 4$. The figure shows that the solution has converged and a steady-state has been reached. Typically oscillations are seen during the initial (first few hundred) steps before the solution settles down and reaches a steady-state. Also, steady-state and convergence were usually achieved by about 1500 steps for both the cases presented here.

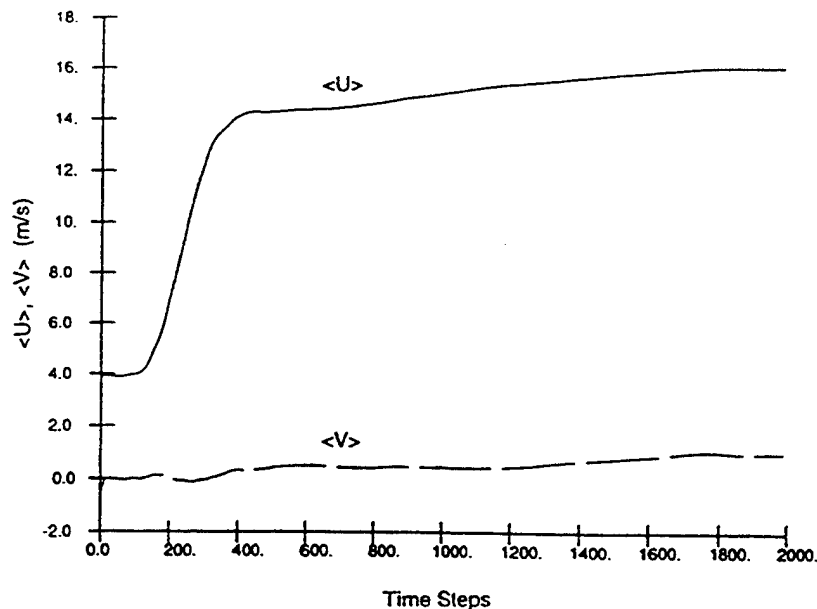


Figure 10-2. Convergence history for the mean axial and radial velocities for the hydrogen flame computations.

Figure 10-3 shows the radial profiles of normalized mean axial velocity $\langle U \rangle$ at different downstream locations compared against data. The measurements are conditional on the origin of the fluid and are made by seeding (for LDV) each of the jets (fuel, annulus and coflow) individually. Differences in the velocity statistics for each of the jets can be seen in the data. The pdf method can calculate these conditional values without requiring additional modeling, and such calculations have been presented in previous chapters. However, in the present study, only the unconditional quantities are calculated and compared against data. The present results (solid lines) are also compared against results from the boundary-layer (b-l) algorithm (dashed line). Figure 10-3 shows that the present results are in excellent agreement with data at all stations. Also, the present calculations are in better agreement with data than the b-l results not only with respect to the overall spreading but also in the near-nozzle region ($x/D = 1.06$ and 2.65) where the flow is tending toward recirculation (near $r/R = 1.5$) and the b-l approximations are inaccurate.

Similar observations can be made for the swirl velocity results presented in Figure 10-4. Although the b-l calculations are in good agreement with data, the present calculations show a better agreement.

The profiles of mean (Reynolds-averaged) temperature, \bar{T} , presented in Figure 10-5 show that the transport and mixing of the fuel is well calculated in the present study, resulting in a very good agreement with the temperature data. (Note that CARS measurements are closer to Reynolds-averaged values than density-weighted values as discussed in section 8.5.) The present results are better than the b-l results at the downstream locations, but near the nozzle (e.g., $x/D = 2.65$) the present results show a lower peak and a greater spread than the data and the b-l results show. Results for the temperature variance from both the methods (not shown here) were overall in good agreement with data although some differences consistent with their mean temperature profiles were observed.

Profiles for turbulent kinetic energy presented in Figure 10-6 show that both the calculations are in good agreement with data in the region up to $x/D = 5.29$ while the b-l calculations overpredict the kinetic energy at downstream locations which is consistent with the lack of spreading in the mean velocity profiles. Sample results from the present calculations for third and fourth order turbulent correlations presented in Figure 10-7 are in good agreement with data.

Overall, the results are in very good agreement with data, and are as good or better than those obtained with the boundary-layer calculations.

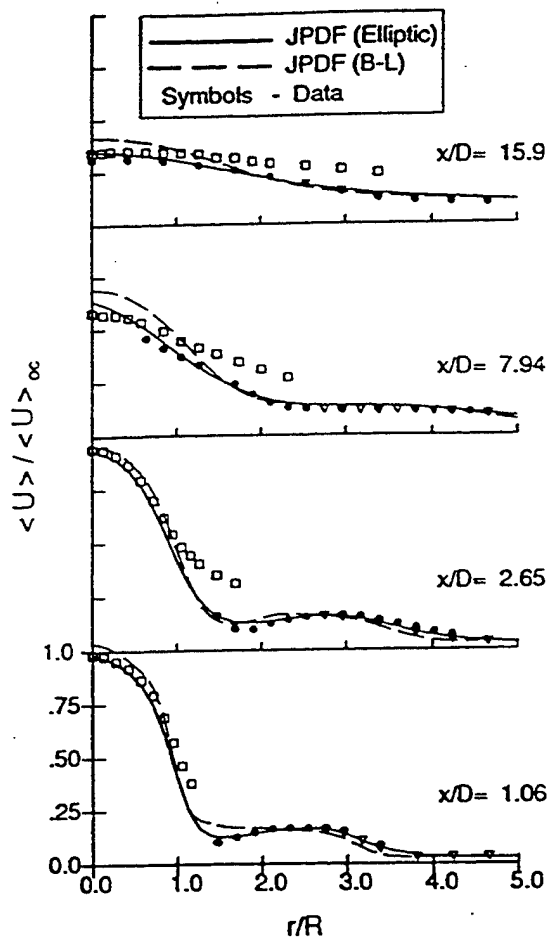


Figure 10-3: Computed mean axial velocity profiles compared against data for the hydrogen flame.

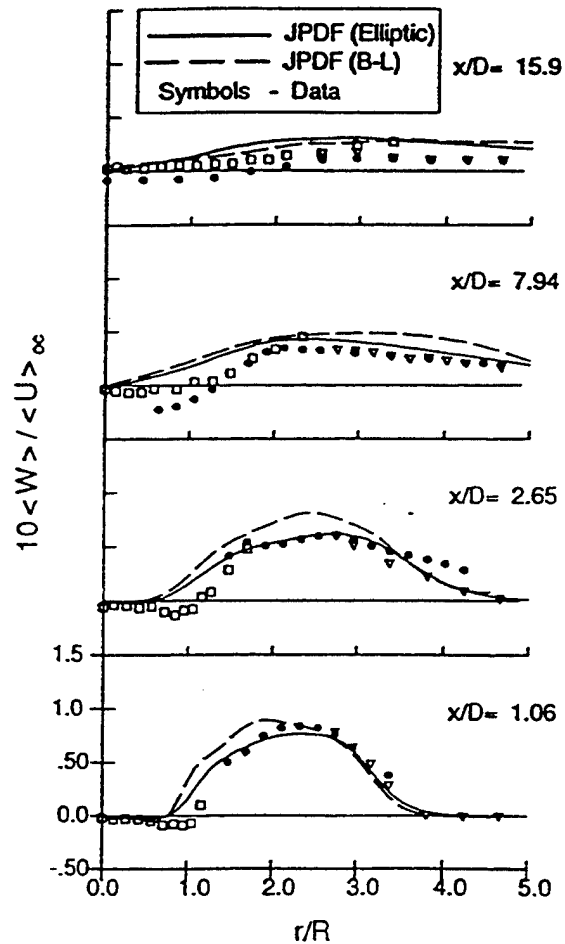


Figure 10-4: Computed mean swirl velocity profiles compared against data for the hydrogen flame.

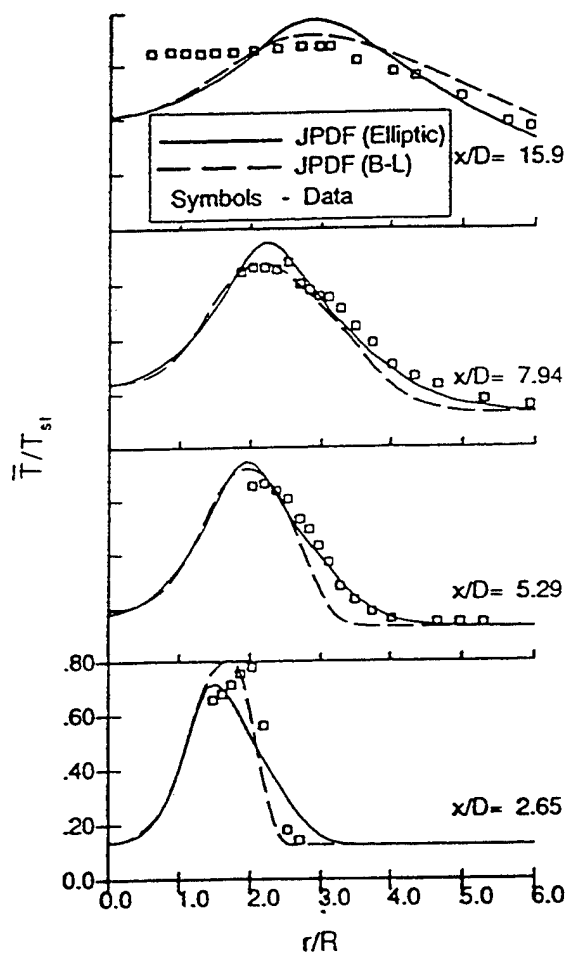


Figure 10-5: Computed mean temperature profiles compared against data for the hydrogen flame.

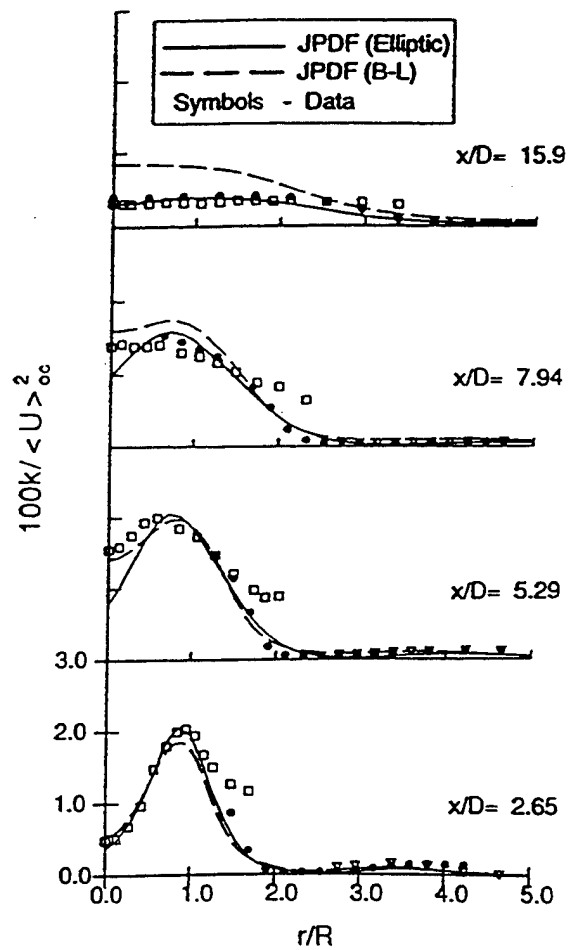


Figure 10-6: Computed turbulent kinetic energy profiles compared against data for the hydrogen flame..

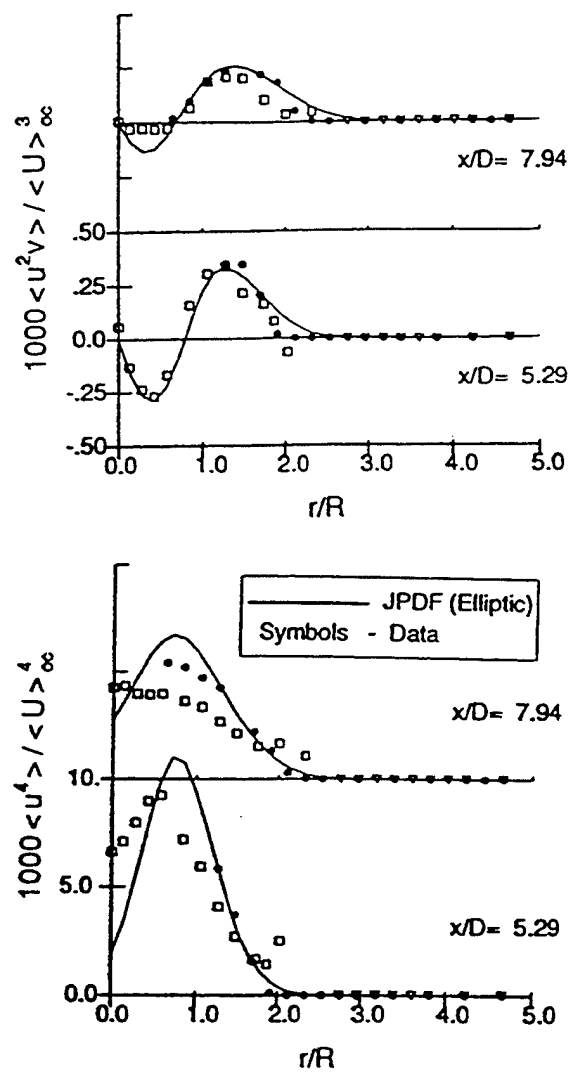


Figure 10-7: Computed profiles of higher-order turbulent correlations compared against data for the hydrogen flame.

10.4.2 Methane Step-Swirl Combustor

The step-swirl combustor shown in Figure 10-8 is an extension of the jet diffusion flame combustor (Figure 10-1), and is closer to a practical gas turbine combustor. It consists of a central air jet (20 mm diameter) surrounded by an annular fuel tube (29 mm o. d.) which is again surrounded by a swirling air jet (40 mm o. d. taken to be the characteristic diameter D). Measurements for this case are reported in Ref. [10-6]. For the case considered here the inner air jet was nonswirling and the outer air had a 30 deg. vane-angle swirler. The bulk velocity for the inner air, fuel and outer air jets are 14.4, 2.5, and 8.6 m/s, respectively.

The velocity data reported for this combustor are also conditional velocities. Unfortunately, the authors [10-6] were unable to measure the velocities conditional on the outer air jet due to practical difficulties such as the LDV seed particles striking the optical windows and clogging

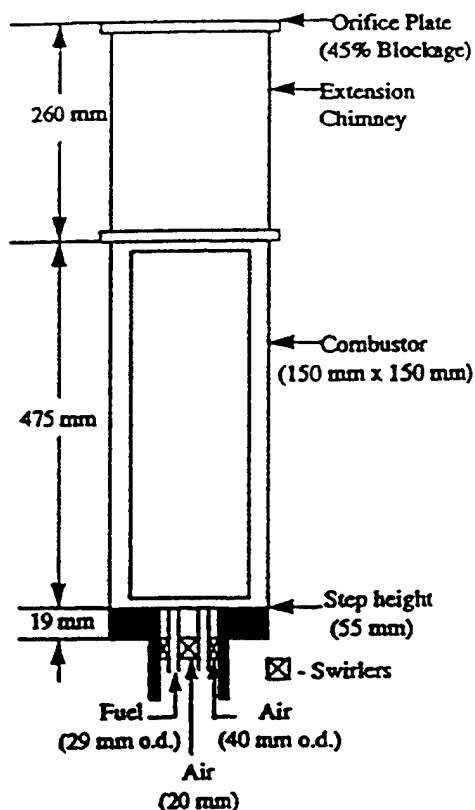


Figure 10-8. Schematic of the step-swirl combustor. The fuel used is methane.

them up. The outer swirling flow has a major effect on the development of the flow and it is crucial to have accurate inlet conditions to accurately simulate the flow. The computations also show high sensitivity to the inlet profiles, especially since the comparison with data is made in the region $x/D < 2$ up to which measurements were made. In the present study the inflow velocity profiles had to be reconstructed based on existing experimental data and the overall mass flow rates through the different streams.

The computations were performed using a nonuniform 41×41 grid using 200 particles per cell. The computations were made for 2000 steps with convergence achieved in most of the flow field by about 1500 steps. The results are presented in Figures 10-9 through 10-14. The values used for normalization in the figures are $\langle U \rangle_{oc} = 21.6$ m/s, $T_{st} = 2272$ K, $D = 40$ mm, and $R = D/2$. For the experimental data presented, the solid symbols represent data conditioned on the inner air jet and the open symbols represent data conditioned on the fuel jet.

The profiles of mean axial velocity, $\langle U \rangle$, presented in Figure 10-9 show the calculations capture the overall flow features well. Although the recirculation is well predicted, the location and radial extent of the recirculation zone which are very sensitive to the inlet mean radial and swirl velocities assumed for the outer swirling jet, are underpredicted.

The profiles of mean radial velocity, $\langle V \rangle$, in Figure 10-10 show the expected trends although data are not available in the critical regions where the largest radial velocities are present. Note that computed results are unconditional and are expected to be lower than the fuel conditioned radial velocity at the outer edge of the fuel jet as seen at $x/D = 0.5$. Figure 10-11 shows that the mean swirl (or tangential) velocity, $\langle W \rangle$, is well predicted both in terms of the peak location and the decay downstream.

The mean temperature profiles presented in Figure 10-12 predict the shapes of the measured profiles well and for the most part agree in magnitude with the data. The profile of the fuel mass fraction at the inlet significantly influences the temperature distribution at the near-nozzle locations at which comparisons are being made. Although the fuel tube only supplies fuel, considerable mixing takes place even as the fuel is leaving the fuel tube, and an assumption of a plug flow profile leads to a much worse comparison with temperature than with a smooth but sharply peaked profile assumed for the computations shown.

The profiles of turbulent kinetic energy and a fourth order turbulent correlation shown in Figures 10-13 and 10-14, respectively, are in reasonably good agreement with data. Overall, the results are in good agreement with data for all the quantities considering the uncertainty in the inlet conditions.

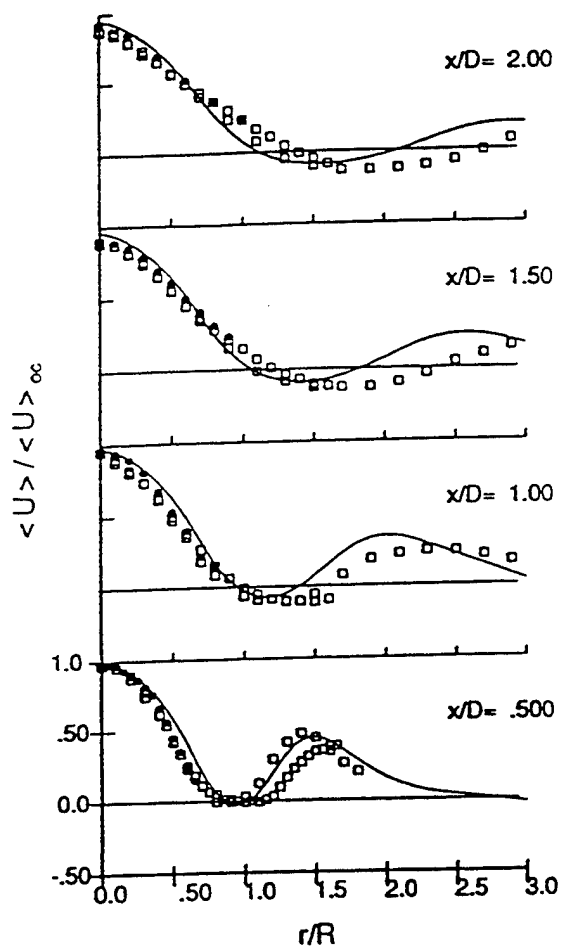


Figure 10-9: Computed mean axial velocity profiles (lines) compared against data (symbols) for the methane flame.

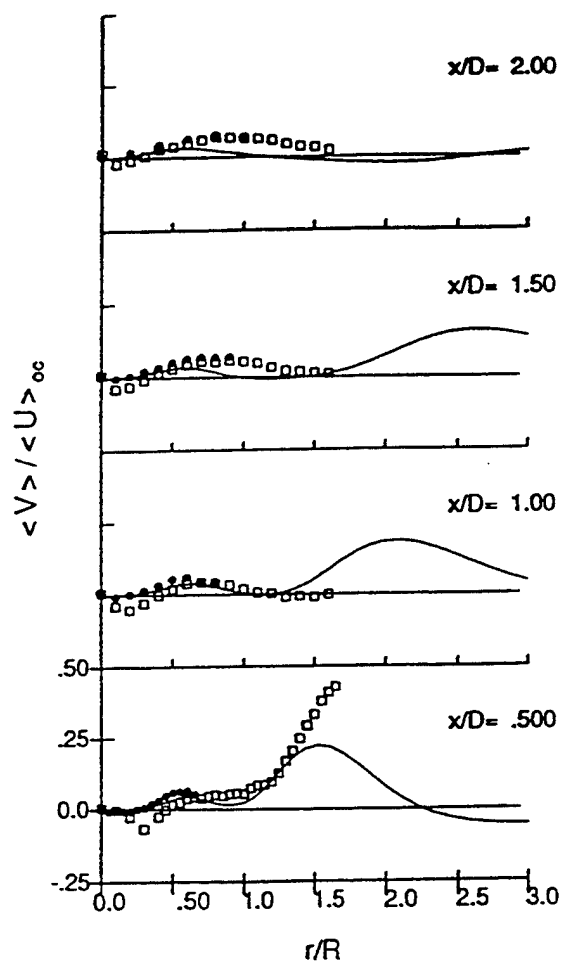


Figure 10-10: Computed mean radial velocity profiles (lines) compared against data (symbols) for the methane flame.

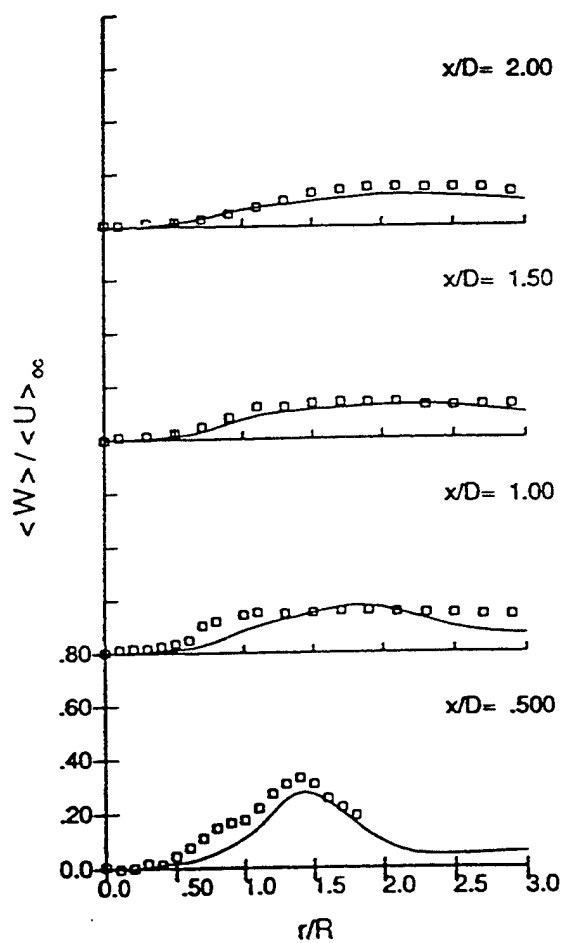


Figure 10-11: Computed mean swirl velocity profiles (lines) compared against data (symbols) for the methane flame.

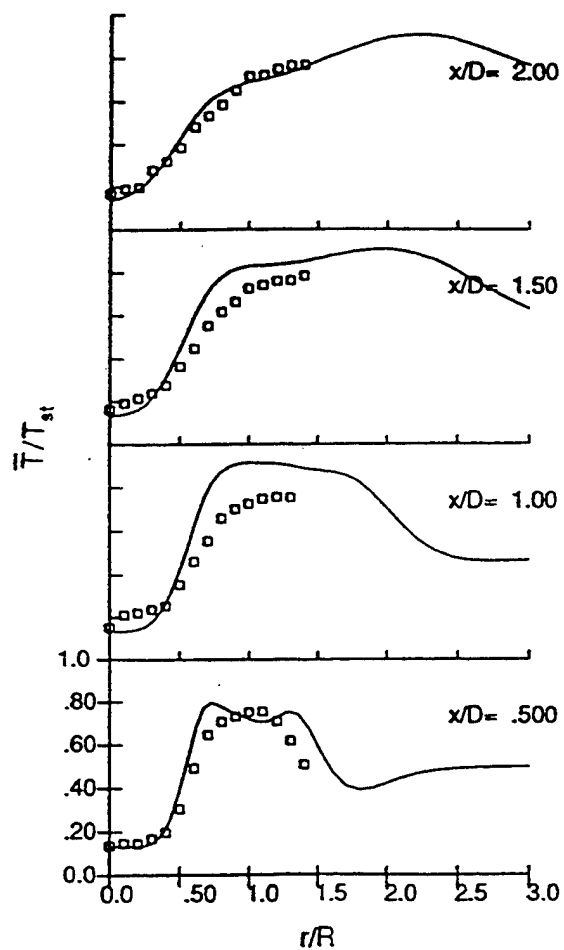


Figure 10-12: Computed mean temperature profiles (lines) compared against data (symbols) for the methane flame.

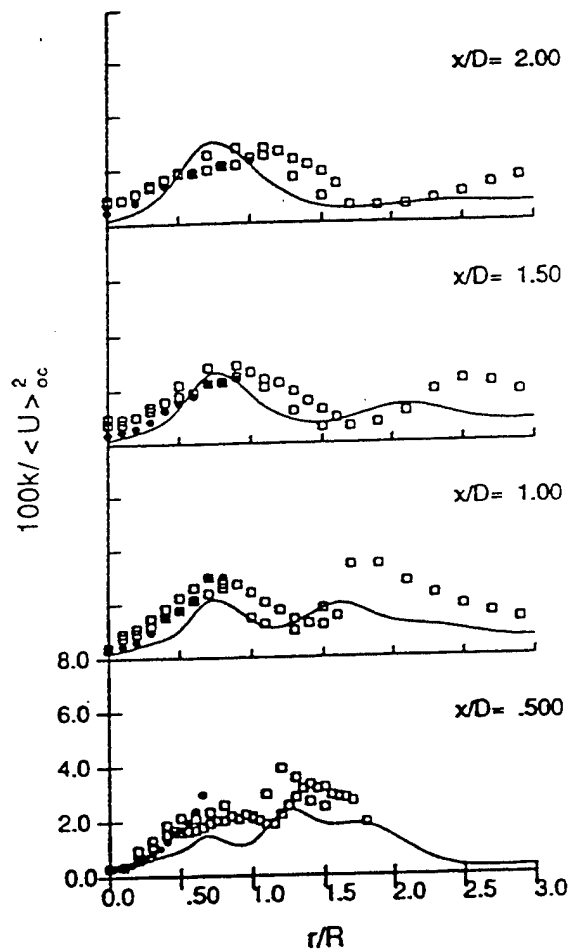


Figure 10-13: Computed turbulent kinetic energy profiles (lines) compared against data (symbols) for the methane flame.

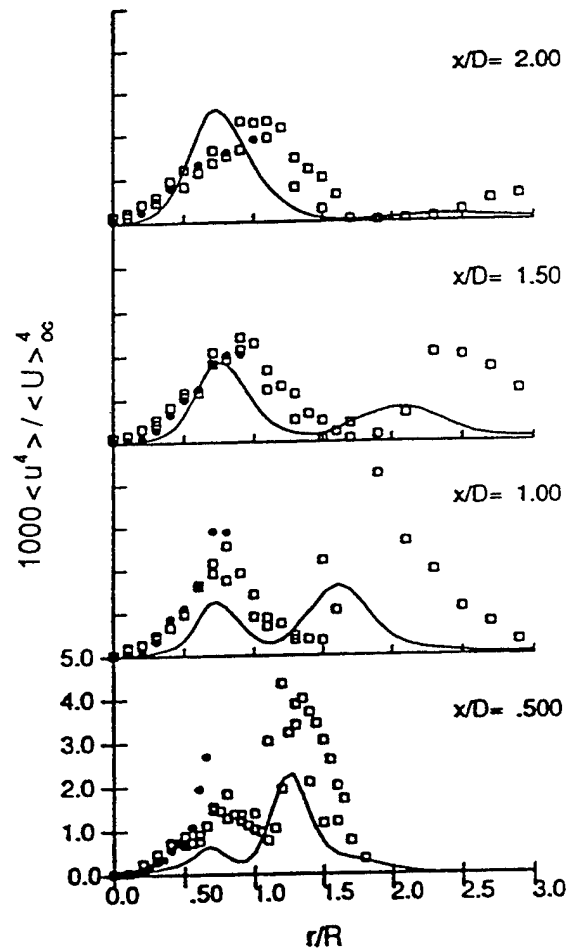


Figure 10-14: Computed profiles of fourth moment of axial velocity (lines) compared against data (symbols) for the methane flame

The results for the hydrogen and methane cases have validated the new models and the elliptic flow algorithm used. The calculations represent the first quantitative results from the new code incorporating the algorithm and models. The results compare very well with the detailed data from practical combustors.

10.5 Summarizing Remarks

Computations using the joint pdf approach have been reported for two swirl combustor configurations. The study uses a newly developed solution algorithm for elliptic flows and new simplified models for velocity and turbulence frequency. The methane combustor calculations represent the first fully self-contained joint pdf calculations for elliptic reacting flows. The results for both combustors are in good agreement with data. The study serves to further validate the joint pdf method and the models, and is a significant step in the development of a pdf-based combustor design system.

The ability of the joint pdf method to accurately calculate the mean and turbulent velocity fields, scalar transport, and temperature using multi-step finite-rate chemistry offers significant advantages for its use in the design of current and future high performance and low emissions gas turbine combustors.

The present results are compared against calculations using the scalar pdf method (in which the joint pdf of only the scalars is considered) and other conventional turbulent combustion models in the next chapter. The study demonstrates the advantages and the superior accuracy of pdf methods, in particular the joint velocity-scalar pdf method.

REFERENCES

- 10-1. M. S. Anand, A. T. Hsu, and S. B. Pope, "PDF Calculations for Swirl Combustors," AIAA Paper 96-0522, 1996. Submitted to AIAA Journal.
- 10-2. T. D. Dreeben and S. B. Pope, FDA 92-13, Cornell University, Ithaca, NY, 1992.
- 10-3. S. B. Pope, Report FDA 95-06, Cornell University, Ithaca, NY, 1995.
- 10-4. C. K. Westbrook and F. L. Dryer, Combustion Science and Technology, **27**, 1981.
- 10-5. M. S. Anand, F. Takahashi, M. D. Vangsness, M. D. Durbin and W. J. Schmoll, ASME 95-GT-307, To be published in The Transactions of the ASME.
- 10-6. M. D. Durbin, M. D. Vangsness, D. R. Ballal, and S. R. Katta, ASME 95-GT-111, 1995.

11. ASSESSMENT OF PDF VERSUS CONVENTIONAL MODELS

11.1 Overview

The objective of the work presented in this chapter is to systematically assess the performance of the joint pdf method against several other methods and models used in practical combustion computations. The methods evaluated include laminar chemistry, the eddy breakup model, the assumed pdf model, the scalar pdf method, and the joint velocity-scalar pdf method. As explained earlier, the treatment of turbulent transport and the two-way turbulence/chemistry interactions are some of the key issues in the computations of turbulent reacting flows. The assessment is done by comparing the different model results against benchmark data from two different gas-turbine-like combustors presented in the previous chapter. The present work shows that the pdf methods, especially the joint pdf method, offer considerable advantage in dealing with these key issues, and, as a result, are more accurate than the conventional models. The study presented in this chapter was conducted under Allison's IR&D program. It is reported in detail in Ref. 11-1. An application of the pdf method to a practical design problem and the advantages offered are also presented and discussed.

11.2 Background

As discussed in Chapter 2, important physical phenomena to be considered in the simulation of turbulent reacting flows include the chemistry closure problem, turbulent transport and the two-way interaction between turbulence and chemistry. The chemistry closure problem is caused by the following two factors: (1) according to the Arrhenius law, the reaction rate coefficient is an exponential function of the temperature and (2) in turbulent flames, large fluctuations in temperature and species concentrations occur. Because of these two factors, the mean reaction rate is often very different from the reaction rate calculated from the mean temperature and species concentrations, and the modeling of this term becomes a major hurdle in turbulent combustion simulations. This effect of turbulence on chemistry is part of the two way turbulence/chemistry interaction. In the other direction of this interaction, the fluctuation in reaction rates causes density fluctuations in the turbulent flames, which in turn causes turbulence modulation and other effects including counter-gradient diffusion.

The pdf methods, including the scalar pdf and joint velocity-scalar pdf methods, offer key advantages for addressing these issues. In the present study, we try to assess the performances, including the accuracy and computer resources requirements, of these methods, and compare them with the conventional combustion models such as the assumed pdf model, the eddy breakup model, and laminar chemistry. The accuracies of these methods are assessed by comparing the numerical results for a swirling hydrogen jet flame and a methane step-swirl combustor against benchmark experimental data for these two configurations.

11.3 Description of Models Used for Comparison

11.3.1 Laminar Chemistry and Eddy Breakup Models

The lowest order of approximation for turbulent reaction rates is the use of laminar chemistry, where the mean temperature and mean species mass fraction are used to calculate the reaction rate coefficients. This simplistic treatment, though known to produce erroneous results, is still occasionally used. Because of the temperature and species concentration fluctuations in a turbulent flame, the reaction rates calculated using laminar chemistry model are often too high. A quick fix to this problem is found in the eddy breakup model, where an upper limit is set for the reaction rate based on the turbulent time scale.

11.3.2 Assumed PDF Model

The next level of approximation in the hierarchy of turbulent combustion models is the assumed pdf model. The assumed pdf method (see, e.g., [11-2]) relies on assumptions of the shape of the pdf, and can only handle simple chemistry models where a single conserved scalar can be defined from which all other variables can be derived. The advantage of this method is its simplicity, while the disadvantages are its limited applicability and the a priori assumption of the shape of the pdf.

11.3.3 The Scalar PDF Method

An alternative to assuming the shape of the pdf is to solve for it from a pdf transport equation. Hence a model for treating turbulent combustion is not needed. A pdf transport equation can be derived for the scalars such as the species mass fractions and the enthalpy, and from the transport equation the pdf distribution can be solved for; this forms the basis for the scalar pdf method

[11-3, 11-4]. The scalar pdf method offers the advantage of treating the turbulent reaction rate without modeling. It relies on a finite difference or finite volume flow formulation to provide the mean velocity and turbulence time scale, and turbulent convection of scalars has to be modeled. The other advantage of the scalar pdf is that it can be used in conjunction with existing, well established numerical methods for the flowfield calculations. However, the inherited deficiencies of the current Reynolds-averaged methods in calculating turbulent transport are the drawbacks. While the interaction of turbulence on chemistry is accounted for in the scalar pdf method, the reverse interactions (see section 2.1.4) are not fully accounted for.

The joint pdf method overcomes the problems with calculating turbulent transport and more comprehensively accounts for turbulence/chemistry interactions.

11.4 Description of the Solution Methods Used

11.4.1 The Scalar PDF Method

A node-based Monte Carlo method is used in the present study to solve the scalar pdf equation [11-3, 11-4]. The mean flow variables, including the mean velocity, pressure, and turbulent kinetic energy, are provided by a pressure based variable-density finite-volume flow solver (which will be further described in the next section). The species mass fraction, temperature, and density are obtained from the Monte Carlo pdf solver. To couple the finite volume solver and the Monte Carlo pdf solver, the mean velocity and turbulent time scale are passed from the finite volume solver to the Monte Carlo solver and the mean density is passed from the Monte Carlo solver to the finite volume code.

11.4.2 Finite-Volume Method

The finite volume method used for the scalar pdf calculation as well as conventional model calculations is the well known pressure-based low-speed variable-density Navier-Stokes method (SIMPLER) [11-5], with a standard k- ϵ model. The solver employs a staggered grid, with the scalar quantities located at the centers of the cells and the velocities at the cell boundaries. A power-law differencing scheme is used to discretize the governing equations. Various chemistry models and spray and evaporation models are available in the code.

An assumed pdf model is used in the reaction calculations. The transport equations of the mixture fraction, $\langle\phi\rangle$, and mixture fraction variance, $\langle\phi'^2\rangle$, are solved. A beta-function pdf is determined based on $\langle\phi\rangle$ and $\langle\phi'^2\rangle$, from which the temperature and density are determined.

When using multistep chemistry models in the finite volume method, the above assumed pdf method is not applicable, and the eddy breakup model is used to simulate the effect of turbulence on the reaction rate. In this method, the reaction rate is calculated using laminar chemistry, but an upper limit for the reaction rate is determined based on the turbulence time scale.

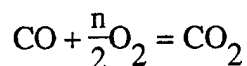
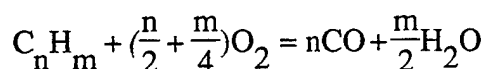
11.4.2 The Joint PDF Method

The joint pdf method used is the same as that described in Chapter 10. The new pressure algorithm PA II along with the SFM II and SLM II models for frequency and velocity are used.

11.5 Thermochemistry

Hydrogen and methane flames are studied in the present work. A fast chemistry model is used for the hydrogen flame calculations because the time scale for hydrogen-air reaction is very small compared to the turbulent time scale.

For methane flame calculations, a general 2-step chemistry by Westbrook and Dryer [11-6] for saturated hydrocarbon fuels is used. The two steps are:



with the reaction rate constants for methane given by

$$A_1 = 1.5 \times 10^7, \quad N_1 = 0, \quad E_1 = 1.25 \times 10^5$$

$$A_2 = 1.0 \times 10^{12.35}, \quad N_2 = 0, \quad E_2 = 1.67 \times 10^5.$$

For details on the chemistry models, the readers are referred to Ref. 11-6.

For both the fast chemistry and the 2-step chemistry models, lookup tables were created to reduce the CPU requirements of the calculations. In the case of the fast chemistry, a one-dimensional table is created. For the two-step chemistry, a three-dimensional table is generated for a given specific time increment. In all the table generation processes, the NASA CEC thermal data were used to calculate the variable specific heat and the temperature.

11.6 Results and Discussion

11.6.1 Swirling Hydrogen Jet Diffusion Flame

For the purpose of quantitatively assessing the various models used in combustor designs, the first case considered in the present study is a hydrogen swirl combustor [11-7]. The schematic and the details of the combustor and experiments are presented in Chapter 10. The inlet average mean velocities are 100 m/s for the central fuel jet, 20 m/s for the annular swirling air jet, and 4 m/s for external air. The swirl angle is 30 degrees, corresponding to a swirl number of 0.38.

The hydrogen swirling jet experiment is one of the very few cases where there is no ambiguity about the inflow conditions for the velocity field, which makes it ideal for model validation and evaluation. Velocities and turbulent kinetic energy at 1.5 mm, or 0.17 fuel jet diameters, downstream of the jet exit are provided by the experiment and are used in the present study as inflow boundary conditions. The inflow profile for the fuel mass fraction is assumed to be uniform.

The computation assumes the flow field to be axisymmetric. For the scalar pdf, assumed pdf, and laminar chemistry computations, the computational domain extends 280 mm downstream from the jet exit; the lateral boundary of the domain is 75 mm from the centerline. A 70x76 grid is used in the computation. To enhance the resolution in regions of interest, the grid is slightly stretched. For the Monte Carlo simulation of the scalar pdf, 50 notional particles are used for each computational cell. A time averaging is performed to reduce the statistical error [11-8]. The time averaging is restricted to about the last 300 time steps.

In the results presented below, the velocity is nondimensionalized using the centerline nozzle exit velocity $\langle U \rangle_{oc} = 130.3$ m/s. The axial distances and radius are normalized by the nozzle diameter, $D = 9.45$ mm and nozzle radius $R = D/2$, respectively. The temperature is normalized by the stoichiometric temperature, $T_{st} = 2377$ K.

Figures 11-1 through 11-3 show the predicted velocity and turbulent kinetic energy distributions compared with experimental data. The symbols represent the experimental data and curves are numerical predictions using joint velocity-scalar pdf, scalar pdf, assumed pdf, and laminar chemistry, as indicated by the figure legends. The joint pdf method predicted the $\langle U \rangle$ velocity better than the other three methods. It also could be argued that the joint velocity-scalar pdf does a better job for turbulent kinetic energy at some locations. The solutions from the scalar pdf, the assumed pdf, and the laminar chemistry for the velocity distribution seem to overlap one another. The joint velocity-scalar pdf also provides information on other statistical quantities and higher moments, that are discussed in Chapter 10.

Of more importance to combustion analysis than the velocity distribution is the temperature rise due to combustion. Figure 11-4 shows the numerical solution for temperature compared to the experimental data, and Figure 11-5 shows the joint velocity-scalar pdf and scalar pdf predictions of the temperature fluctuation compared with experimental data. One immediately notices that the solution obtained using a laminar chemistry is unacceptable: The peak temperature is grossly overpredicted, and the flame is too narrow. The assumed pdf method, because it took into consideration the effects of turbulent fluctuations, provided a much better solution for the temperature field, although it still underpredicted the flame edge temperature at $x/D=7.94$ and overpredicted the temperature at $x/D=26.5$. Both the scalar pdf and the joint pdf methods predicted the temperature distribution fairly accurately, with the joint pdf method matching the data slightly better, demonstrating the superiority of the pdf methods.

Figure 11-6 shows the temperature variance predicted by the scalar and joint pdf methods compared with experimental data. The measurement of temperature variance in the experiment depended on the existence of nitrogen, and therefore missed the inner peak corresponding to the large temperature gradient on the left side of the flame for $x/D=1.06$, 5.29 , and 7.94 . Although some differences exist between the predictions, both the scalar pdf and the joint pdf methods are able to predict the temperature fluctuations with reasonable accuracy.

11.6.2 Step-Swirl Methane Combustor

The second case considered in this study is a step-swirl methane combustor for which experimental data were obtained by Durbin et al. [11-9]. The combustor details are presented in Chapter 10. The case considered has an outer swirl angle of 30 degrees and no inner swirl. The average velocity of the inner air jet is 14.4 m/s; the average velocity of the outer air jet is 8.6 m/s; and the average fuel jet velocity is 2.5 m/s.

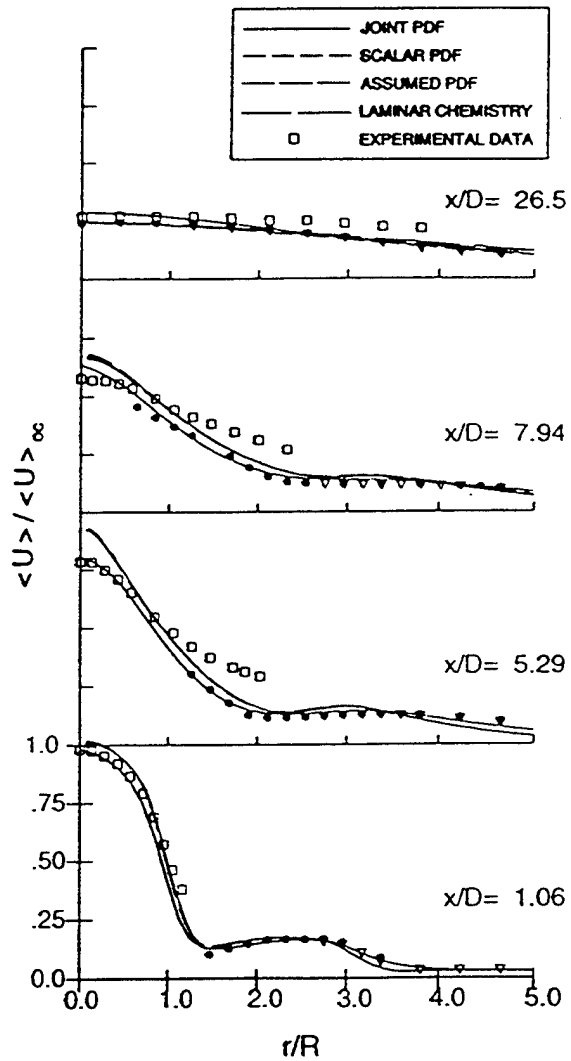


Figure 11-1. Computed axial velocity profiles compared with experimental data for the swirl hydrogen flame.

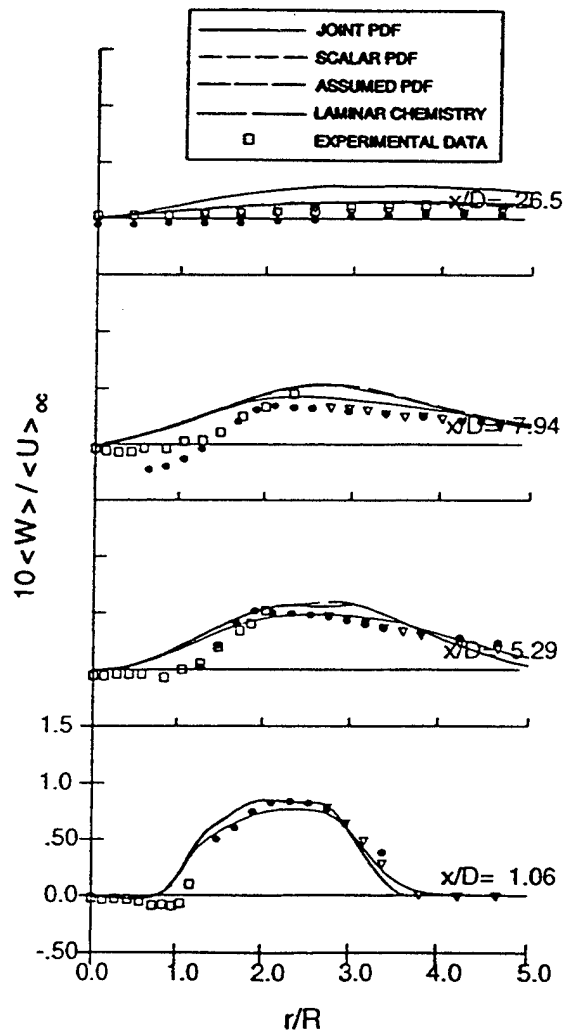


Figure 11-2. Computed swirl velocity profiles compared with experimental data for the swirl hydrogen flame.

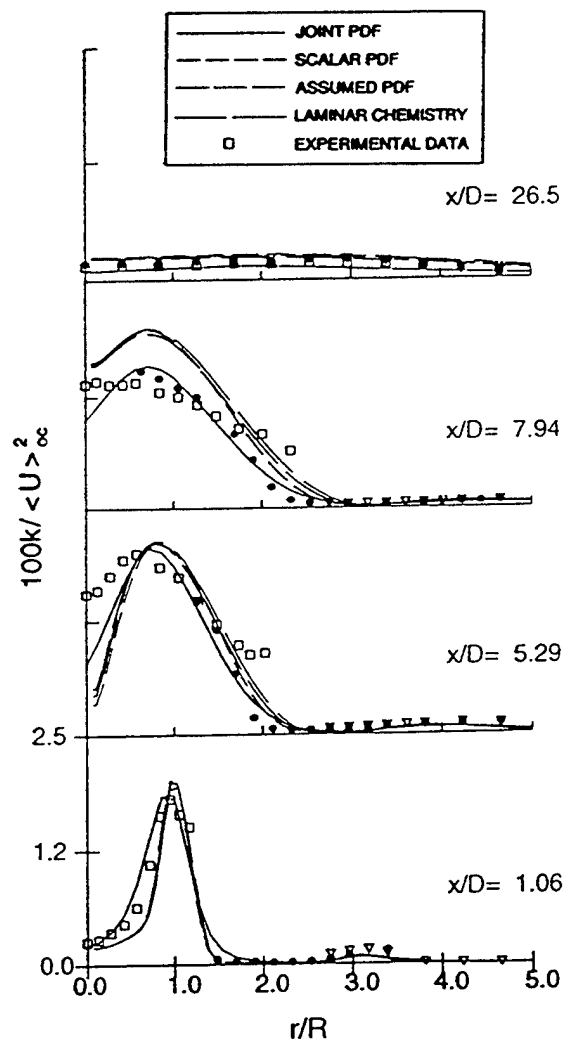


Figure 11-3. Computed turbulent kinetic energy profiles compared with experimental data for the swirl hydrogen flame..

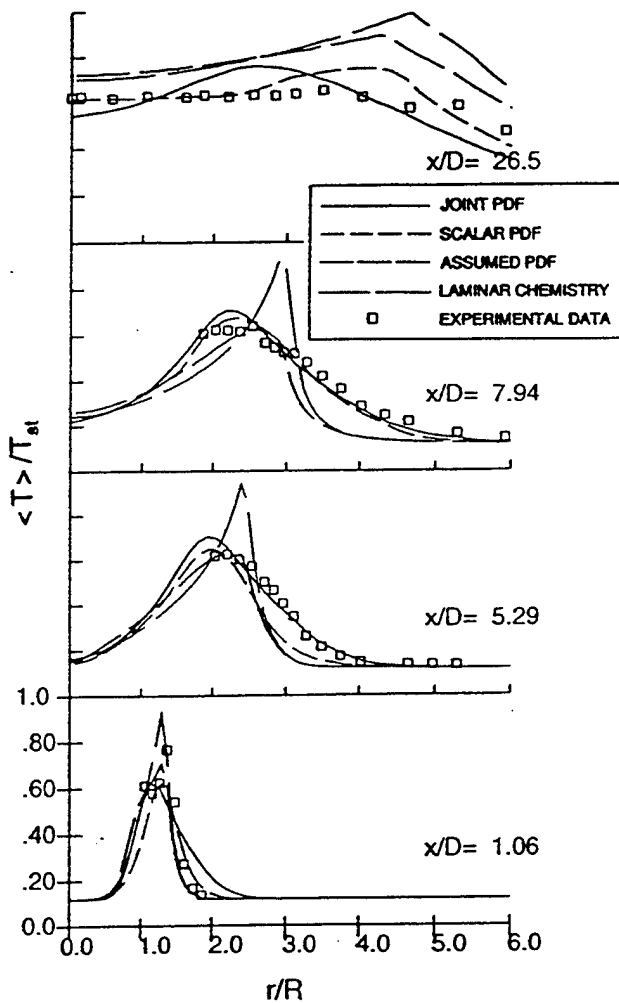


Figure 11-4. Solutions for the mean temperature compared with experimental data for the swirl hydrogen flame..

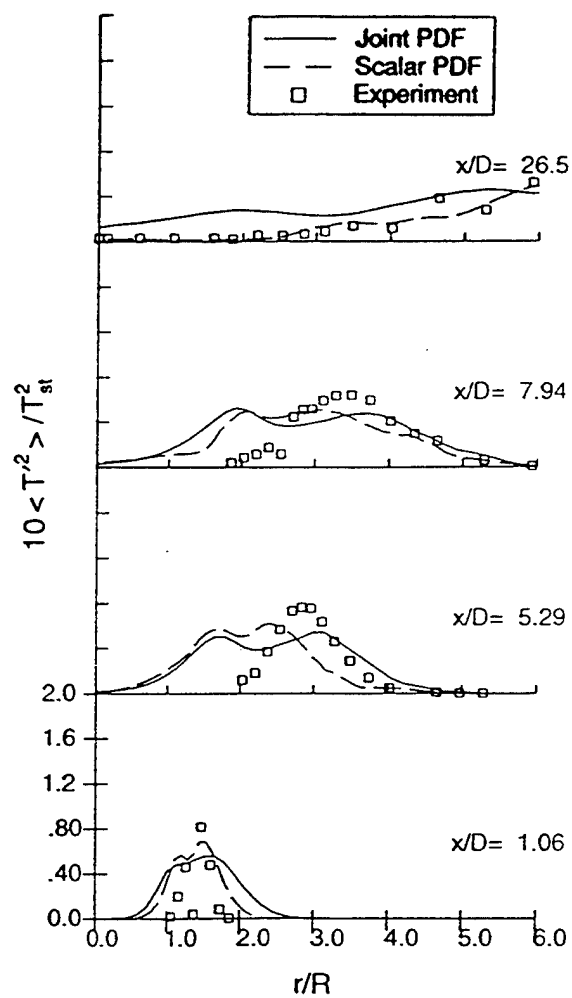


Figure 11-5. Solutions for the temperature variance compared with experimental data for the swirl hydrogen flame.

The numerical setup of the step-swirl combustor calculation is similar to that of the swirling hydrogen flame calculation, with the same number of grid points and notional particles. The computational domain extends 75 mm from the centerline and 130 mm downstream from the jet exit.

The flow field in the step-swirl combustor consists of two recirculation zones, one caused by the step, and a second one caused by the outer swirling jet. The flow is fully elliptic, and the ability to resolve the recirculation is crucial in the computation of this case.

Unfortunately, the experimental data for inflow conditions is incomplete for this case: velocity profiles are available at 3 mm downstream of the inlet only from $r/R=0$ to $r/R=1.3$, and temperatures or fuel mass fraction distributions are not available. Because the exit velocity profile of the swirler is far from uniform, the information on the inflow condition is crucial to the correct simulation of swirling jets. In the present study, the inflow velocity profiles had to be judiciously extended beyond $r/R=1.3$ based on reported experimental mass flow rates from different streams. With guidance from the conditioned (conditioned upon different streams) velocity measurements, a sharp peaked mixture fraction distribution is used instead of a plug flow profile.

In the results presented below, the velocity is normalized using the centerline nozzle exit velocity $\langle U \rangle_{oc}=21.6$ m/s. The axial distances and radius are normalized by the nozzle diameter, $D=40$ mm and nozzle radius $R=D/2$, respectively. The temperature is normalized by the stoichiometric temperature, $T_{st}=2272$ K.

Figures 11-6 through 11-8 show the comparison between the predicted velocity profiles and the experimental data, and Figure 11-9 shows the comparison for turbulent kinetic energy. The velocity results show that the finite volume method (for both scalar pdf and eddy breakup model) predicted a higher spreading rate for the outer jet, or a larger separation bubble, than the joint pdf method. In general, both the velocity components and the turbulent kinetic energy are well predicted by the three different methods.

The comparison between the numerical solutions for temperature and experimental data is shown in Figure 11-10. The results for $x/D=0.5$ show that the joint pdf method predicted the convection of scalars more accurately, while the other two methods predicted too much spreading. The advantage of the pdf methods is highlighted again in the temperature predictions. Although in the eddy breakup model calculation, the reaction rate is modified to take into account of turbulent effects, because the model does not account for temperature and species fluctuations, the solution show unrealistically high peak temperature at $x/D=0.5$, similar to the laminar chemistry solution

in the hydrogen case. The peaks exist irrespective of the changes made in the inflow conditions. On the other hand, the pdf models were able to correctly simulate the physics in the turbulent flame, including fluctuating temperature and its effects on reaction rates, the mean temperature is better predicted.

The temperature distributions predicted by the three different methods at downstream locations show some differences. Although the predicted temperature profile at $x/D=1.5$ gives the appearance that the eddy breakup model produces an accurate solution, an overall evaluation shows that the eddy breakup model overpredicts the temperature near the jet exit while underpredicts it at downstream locations ($x/D=2.0$), and the agreement at $x/D=1.5$ is quite coincidental.

Because of the uncertainties in inflow conditions and the sensitivity of the solutions to these inflow condition, more detailed comparisons cannot be made. However, based on the results obtained, one can draw the following conclusions:

(1) The eddy break up model can produce spurious peaks in the mean temperature in the reaction zone. The error in temperature could be as high as $T/T_{st}=0.25$ (570K) or higher (see values at $r/R=0.7$ and $r/R=1.5\sim 1.7$, $x/D=0.5$ in Figure 11-10). Such large errors in the high temperature regions have serious implications on the predictions of combustor performance and emissions predictions.

(2) Although the scalar pdf method accounts for turbulence fluctuation effects, inaccurate prediction of the mean and turbulent transport of scalars can seriously undermine its accuracy, as can be observed from results at $r/R>1.5$ at $x/D=0.5$ in Figure 11-10.

It is well known from experimental observations and detailed chemical kinetic calculations that a difference of 50K in mean temperature in the vicinity of the reaction zone can cause large differences in pollutant formation, especially for NO_x. The present results underscore the importance of the pdf methods in accurately predicting combustion efficiency and pollutant emissions such as NO_x, CO and unburned fuel. Similarly, the ability of the joint pdf method to accurately calculate turbulent transport is also very important for predicting the above mentioned combustor parameters.

All the computations presented in this work are done on IBM RS6000 work stations. Because there is no uniform criteria for convergence, a comparison on exact CPU hours is not possible. In general, the scalar pdf method is estimated to be 4 to 5 times more time consuming and the joint

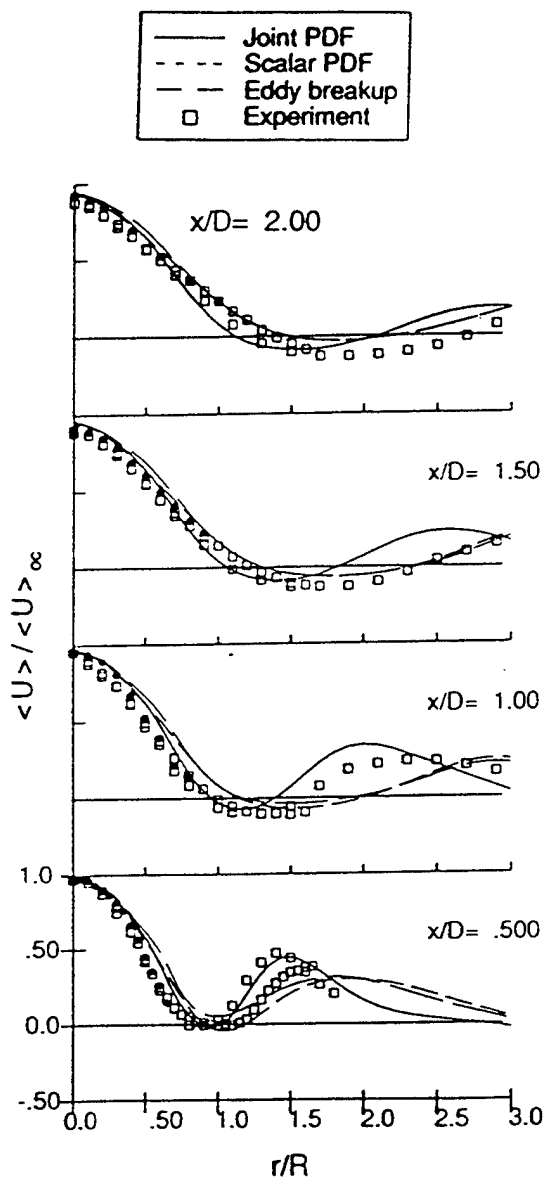


Figure 11-6. Computed axial velocity profiles compared with experimental data for the step-swirl methane combustor.

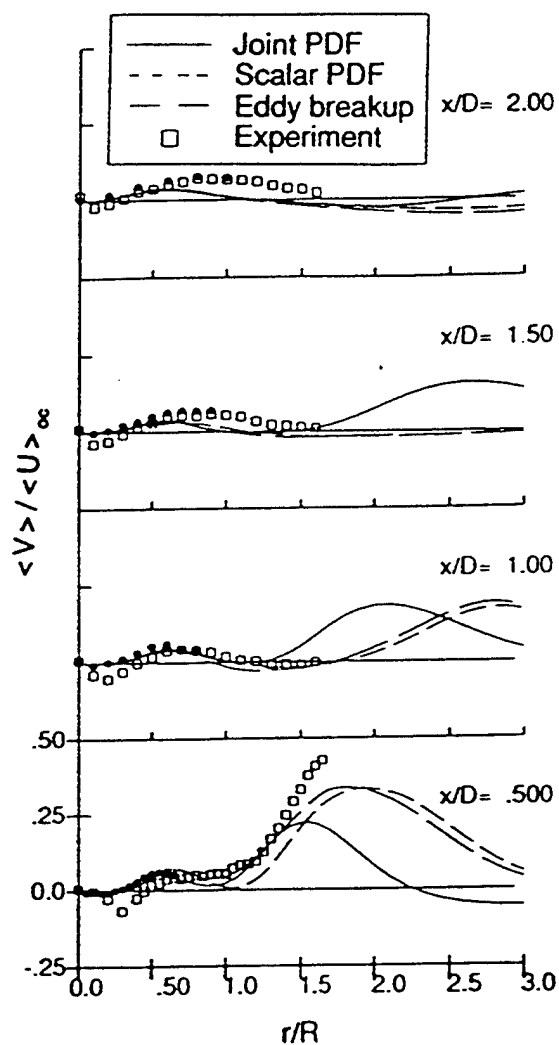


Figure 11-7. Computed radial velocity profiles compared with experimental data for the step-swirl methane combustor.

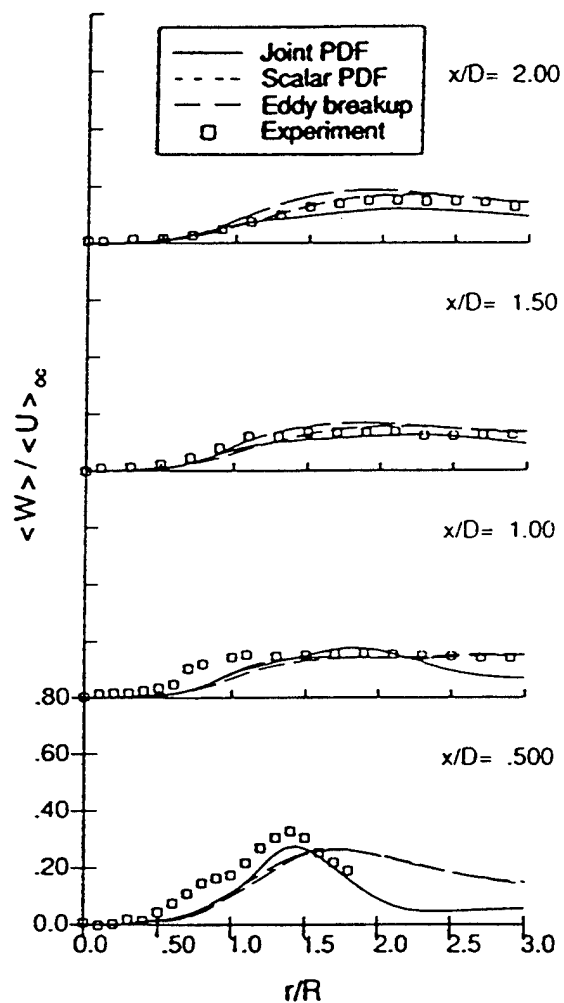


Figure 11-8. Computed swirl velocity profiles compared with experimental data for the step-swirl methane combustor.

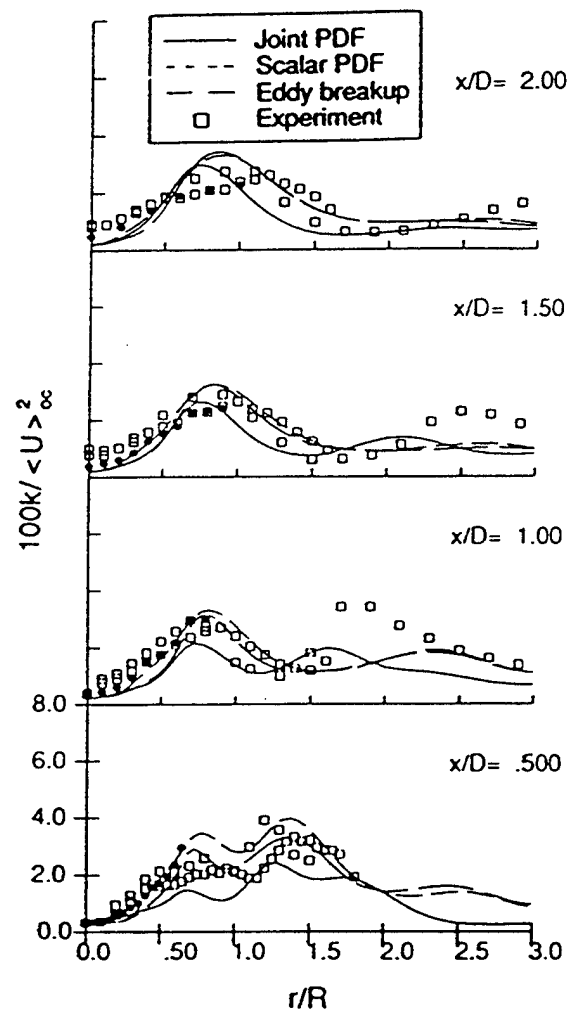


Figure 11-9. Computed turbulent kinetic energy profiles compared with experimental data for the step-swirl methane combustor.

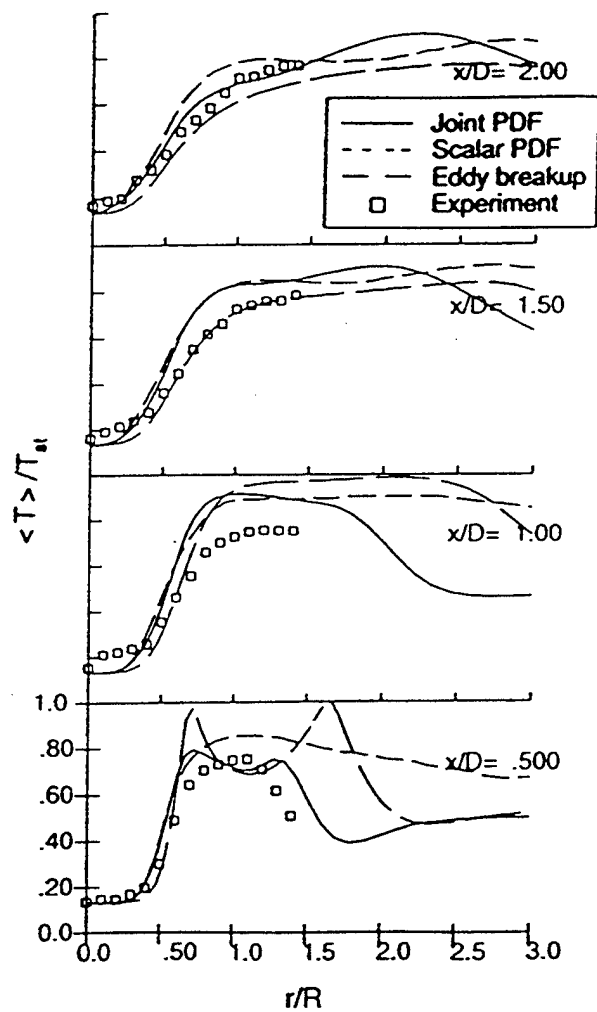


Figure 11-10. Computed mean temperature profiles compared with experimental data for the step-swirl methane combustor.

pdf method 5 to 6 times more time consuming than the finite volume schemes. Considering that the pdf algorithms are new and no significant efforts are made to speed up the computation, we believe that considerable speedup can be achieved through better choices of numerical parameters and improvements in solution algorithms. Furthermore, the Monte Carlo method is very amenable to parallel processing, and considerable speed up can be achieved through parallel computing. It is estimated that a realistic combustor design calculation can be achieved with the joint pdf method with a 1-day turnaround time.

11.7 Computations for a Low Emissions Lean Premixed Combustor

The unique advantages offered by the pdf method are demonstrated through an application to the design of one of Allison's advanced low emission combustors. The combustor is based on a premixer module concept in which fuel (natural gas) and air are mixed under high swirl in a premixing module. Combustion occurs in a lean premixed mode so that the emissions are significantly lower than in conventional diffusion flame combustors. A schematic of the premixer module is shown in Figure 11-11. For the purpose of demonstration, the scalar pdf method is used for the computations of the mixing and reacting flow within the module as well as in the combustor downstream. (More work is needed with the joint pdf method for application to complex geometries with body fitted grids as explained in the next chapter. However, the advantages seen for the scalar pdf method will only be enhanced with the joint pdf method. The two-step finite rate methane chemistry (section 11.5) is used for the computations. Figure 11-12 shows the contour plots of the computed mean axial velocity field, along with those of mean temperature and fuel mass fractions. Measurements for mean velocities, mixture fraction and mean temperature have been made and data are available for comparison. The computations are in good agreement with data both qualitatively and quantitatively.

The crucial advantage provided by the pdf method is the ability to more realistically model premixed combustion with the Monte Carlo algorithm. The joint velocity-scalar pdf method has been used previously in detailed modeling studies of premixed flames [11-10 through 11-12] and its ability to calculate turbulent flames speeds and other fundamental parameters has been demonstrated.

For the combustor under consideration, the results in Figure 11-12 show that the flame is stabilized in front of the large recirculation zone as expected since the velocities are low in that region. The extent of the recirculation zone and the location of the flame are consistent with the experimental data. Also, as expected and borne out by experiments, the discrete fuel jets are well

mixed within the premixer module and the mixture fraction distribution at the exit of the premixer module and especially in the combustor is uniform. Since the mixture fraction within most of the module is lean and within combustible limits, conventional finite-volume based combustion models predict the flame to spread well into the premixer model (even with using finite-rate chemistry) thereby predicting "flashback" as well as erroneous temperatures and emissions. Accurate prediction and avoidance of flashback is one of the key issues in premixed combustor design. However, with the pdf method used, even if the mixture fraction is within combustible limits, the individual computational particles do not burn until they come in contact with other burnt particles. Hence, the interaction of convective and turbulent transport with flame-speeds is captured resulting in the correct prediction of the flame.

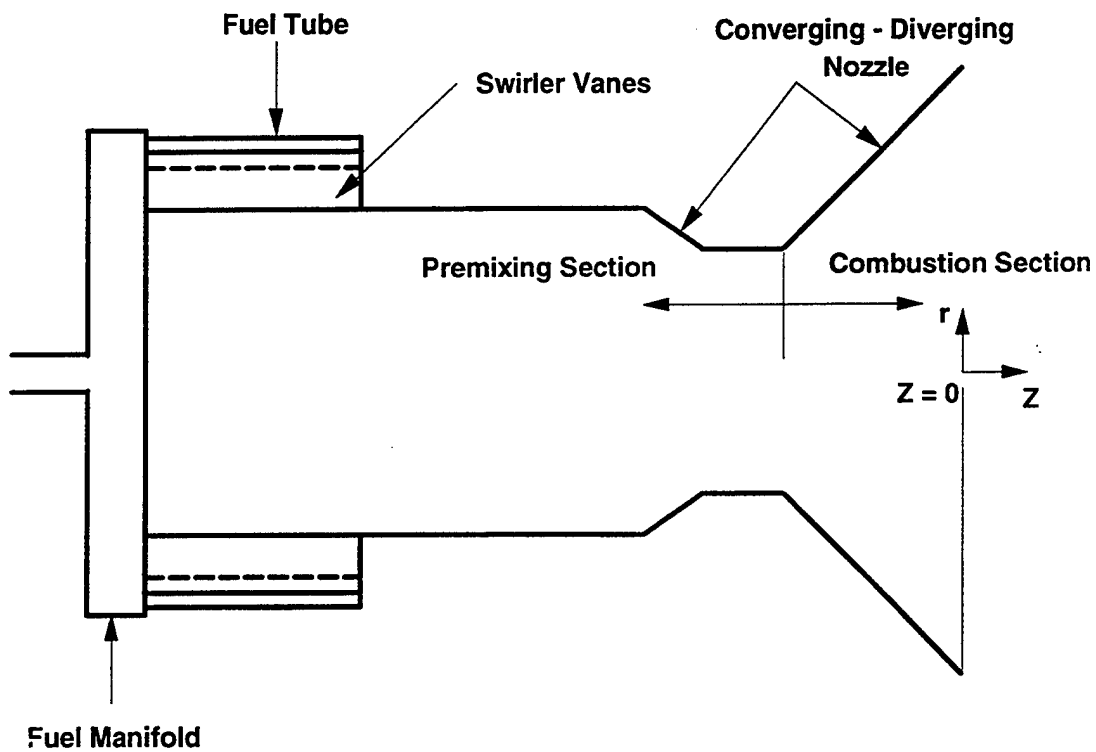


Figure 11-11. Schematic of the RSPN low emissions combustor module.

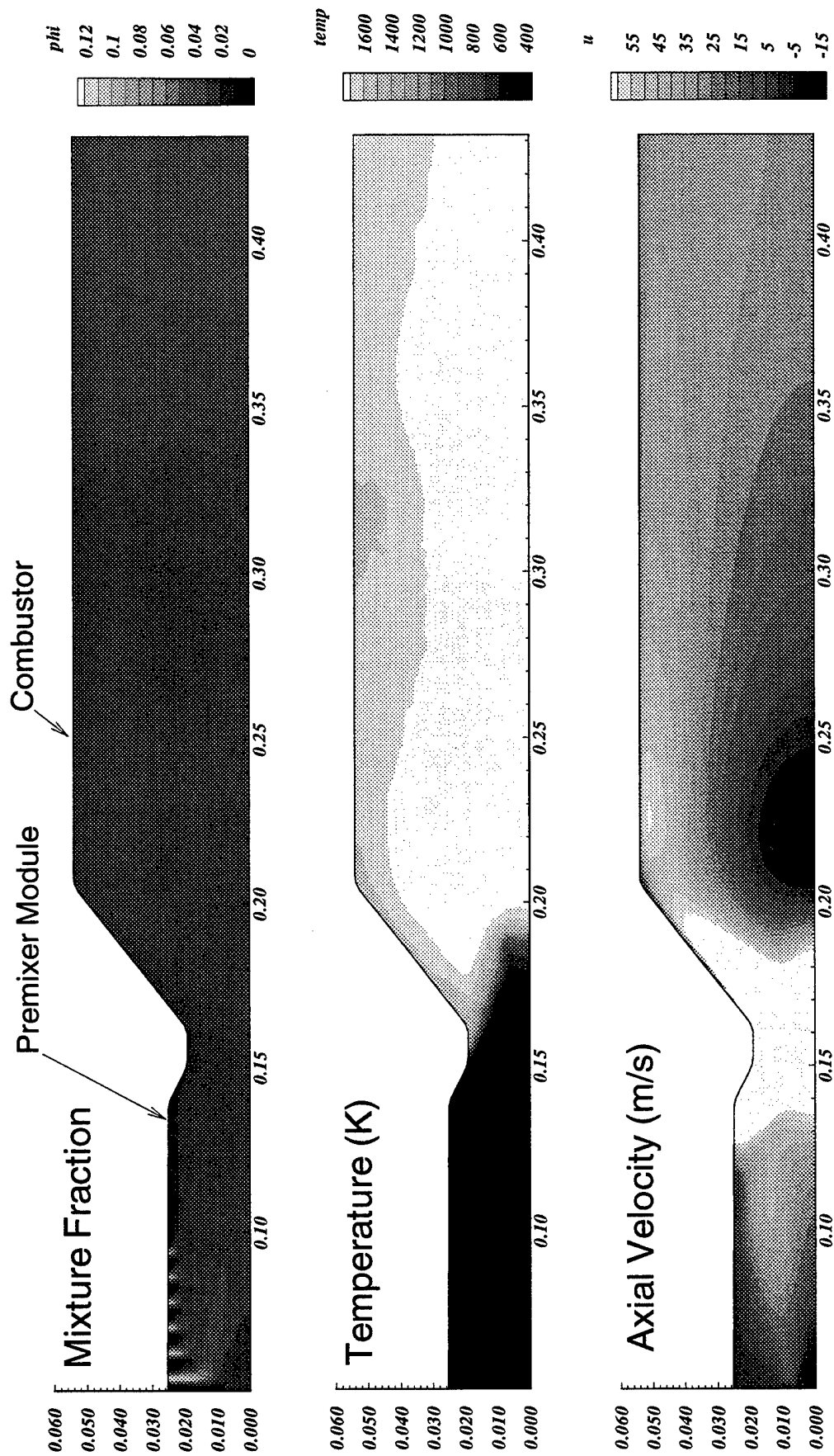


Figure 11-12. Contour plots of mean mixture fraction, temperature and axial velocity computed using the PDF method for the RSPN low emissions combustor. PDF methods offer unique capability for premixed combustor design. (Scalar PDF is used here.)

11.8 Summarizing Remarks

Five different combustion models were evaluated in the present study. The results show that the use of laminar chemistry produces unacceptable results, and the eddy breakup model also produces inaccurate temperature predictions. Assumed pdf is a major improvement over the other conventional combustion models and provides reasonably good aerothermal predictions, provided that simple one step chemistry models are acceptable. The present work again demonstrated that the scalar pdf and joint velocity-scalar pdf methods are superior to the conventional combustion models in handling turbulent combustion problems. The present results underscore the importance of the pdf methods in accurately predicting combustion efficiency and pollutant emissions such as NO_x, CO and unburned fuels. This is demonstrated by an application to a "real" combustor hardware. The additional ability of the joint pdf method over scalar pdf method to accurately calculate turbulent transport and other turbulence/chemistry interactions is also important for predicting combustor performance and emissions.

REFERENCES

- 11-1. A. T. Hsu, M. S. Anand, and M. K. Razdan, " An Assessment of PDF Versus Finite-Volume Methods for Turbulent Reacting Flows," AIAA 96-0523, 1996. Submitted to AIAA Journal of Propulsion and Power.
- 11-2. W. P. Jones and C. Priddin, "Prediction of the Flow Field and Local Gas Composition in Gas Turbine Combustors," Twenty-Seventh Symposium (International) on Combustion, The Combustion Institute, Pittsburgh, 1978.
- 11-3. S. B. Pope, "A Monte Carlo Method for the PDF Equation of Turbulent Reactive Flow, " Combustion Science and Technology, Vol. 25, No. 5, 1981.
- 11-4. A. T. Hsu, Y-L. P. Tsai, and M. S. Raju, "Probability Density Function Approach for Compressible Turbulent Reacting Flows," AIAA Journal, Vol. 32, No. 7, 1994.
- 11-5. K.C. Karki and S. V. Patankar, "Calculation Procedure for Viscous Incompressible Flows in Complex Geometries," Numerical Heat Transfer, Vol. 14, 1988.
- 11-6. C. K. Westbrook and F. L. Dryer, "Simplified Reaction Mechanisms for the Oxidation of Hydrocarbon," Combustion Science and Technology, Vol. 27, 1981.
- 11-7. M. S. Anand, F. Takahashi, M. D. Vangsness, M. D. Durbin, and W. J. Schmoll, "An Experimental and Computational Study of Swirling Hydrogen Jet Diffusion Flames," ASME 95-GT-307, 1995. To be published in the Transactions of the ASME.
- 11-8. A. T. Hsu, M. S. Raju, and A. T. Norris, "Application of a PDF Method to Compressible Turbulent Reacting Flows," AIAA Paper 94-0781, 1994.

- 11-9. M. D. Durbin, M. D. Vangsness, D. R. Ballal, and S. R. Katta, "Study of Flame Stability in a Step Swirl Combustor," ASME Paper 95-GT-111, 1995.
- 11-10. M. S. Anand and S. B. Pope, "Calculations of Premixed Turbulent Flames by PDF Methods," Combustion and Flame, **67**, No. 2, 1987.
- 11-11. S. B. Pope and M. S. Anand, "Flamelet and Distributed Combustion in Premixed Turbulent Flames," Twentieth Symposium (International) on Combustion, The Combustion Institute, Pittsburgh, pp 403-410, 1984.
- 11-12. S. B. Pope, "Turbulent Premixed Flames," Annual Review of Fluid Mechanics, **19**, pp 237-270, 1987.

12. CONCLUDING REMARKS

Significant progress has been made in the development of an advanced and more accurate combustor design tool based on the joint probability density function (pdf) method. The pdf method was chosen based on its inherent and demonstrated advantages over conventional other advanced methods for treating turbulent reacting flows.

Several new submodels and algorithms within the pdf method were developed and validated to enable the application of the pdf method to complex flows of practical interest, such as in gas turbine combustors. The method and the models have been validated against a variety of flows consisting of the essential features of gas turbine combustor flows. Both available experimental data and experiments specifically designed to fill the voids in data in the literature were used to provide benchmark quality data for the validation. The joint pdf results were uniformly in good agreement with data for all the flows considered. The joint pdf results were compared with results from conventional methods and assessed against experiment data. The joint pdf results were clearly more accurate than those from conventional methods. A baseline combustor design system based on the joint pdf method has been developed.

However, significant development effort lies ahead. There are several areas for further improvement of the baseline design system so that the full potential of the pdf design system is realized. The development of the method under the current program focused on gaseous fuels. The current design system can be applied to gaseous fuel applications such as in certain low emissions combustor concepts. There are no theoretical limitations for incorporating liquid fuel sprays in the pdf method. In fact, the advanced spray transport models are also Lagrangian-based and use the Monte Carlo technique. Hence the pdf method and the spray transport models are naturally compatible. A preliminary demonstration of the pdf method incorporating sprays (although nonevaporating and nonreacting) in the boundary-layer algorithm has been performed by Anand [12-1]. The method needs to be extended for evaporating and reacting sprays and incorporated in the elliptic flow algorithm. Allison is a leader in the development of advanced evaporation and spray models [12-2, 12-3]. These models will be incorporated in the joint pdf design system.

The other areas of further development are the treatment of internal blockages, development of the pdf method using body-fitted grids, accurate and efficient implementation of the detailed

combustion chemistry, enhancement of computational efficiency through advanced parallel processing strategies, and extension to complex 3-D flows.

Treatment of internal blockages and the use of body-fitted grids are needed to model complex combustor geometries and the flows in the combustor diffuser or casing. The main challenge here is to develop the tracking procedure for irregular grids in the Monte Carlo solution algorithm and to develop a pressure algorithm for such grids.

To fully exploit the advantages offered by the pdf method to treat complex chemistry, a method to include detailed combustion (which typically includes hundreds of reactions and tens of species) in a computationally efficient way is needed. Allison is collaborating with Professor Pope of Cornell University to further develop and validate such a method which is in part based on the Manifold Method [12-4, 12-5]. The method has shown considerable promise and has demonstrated that accuracy matching that of the detailed chemistry can be obtained with considerably less computational effort.

As more complex flows are calculated with the pdf method, it is essential to utilize parallel processing strategies with the goal of achieving computational turnaround times of a day to allow the combustor designer to effectively analyze and iterate on combustor designs. The current baseline design system already incorporates basic parallel processing strategies and uses particle partitioning. Other strategies such as domain decomposition and other advanced techniques need to be explored.

Computations in complex 3-D geometries will also need to exploit multiblock and multigrid solution strategies to reduce computational effort and to have geometry flexibility without sacrificing computational accuracy. A version of the multigrid capability has already been implemented and tested in the baseline design system.

In conclusion, the current program has been instrumental in the significant development and validation of the joint pdf method as a gas turbine combustor design tool. The demonstrated level of accuracy that can be achieved with the pdf method in calculating complex chemistry, turbulent transport, and turbulence/chemistry interactions is key to the accurate prediction of critical combustion performance characteristics such as efficiency, emissions, exit and wall temperatures, lean blowout, stability, flashback, autoignition, etc., in advanced combustor concepts. Several planned future development activities will lead to the realization of the full potential of the joint pdf design system.

REFERENCES

- 12-1. M. S. Anand, "A Study of Particle-Laden Jet Flow by the PDF Method," AIAA 90-1856, 1990.
- 12-2. N. K. Rizk, J. S. Chin, and M. K. Razdan, "Modeling of Gas Turbine Fuel Nozzle Spray," ASME 95-GT-225, 1995. To be published in The Transactions of the ASME.
- 12-3. J. S. Chin, "An Engineering Calculation Method for Turbine Fuel Droplet Evaporation at Critical Conditions with Finite Liquid Diffusivity," AIAA 95-0494, 1995.
- 12-4. U. A. Maas and S. B. Pope, "Simplifying Chemical Kinetics: Intrinsic Low-Dimensional Manifolds in Composition Space," Combustion and Flame, **88**, 1992, pp. 239-264.
- 12-5. U. A. Maas and S. B. Pope, "Laminar Flame Calculations Using Simplified Chemical Kinetics Based on Intrinsic Low-Dimensional Manifolds," Twenty-Fifth Symposium (International) on Combustion, The Combustion Institute, Pittsburgh, 1994, pp. 119-192.

APPENDIX: LIST OF PUBLICATIONS

(WHOLLY OR PARTIALLY SUPPORTED BY THIS CONTRACT)

1. M.S. Anand, A.T. Hsu, and S.B. Pope (1996) "PDF Calculations for Swirl Combustors," AIAA Paper 96-0522. Submitted to AIAA Journal.
2. S. B. Pope (1995) "Position, Velocity and Pressure Correction Algorithm for Particle Method Solution of the PDF Transport Equations," Report FDA 95-06, Cornell University, Ithaca, NY.
3. Jayesh and S. B. Pope, (1995) " Stochastic Model for Turbulent Frequency," Report FDA 95-05, Cornell University, Ithaca, NY.
4. M. S. Anand, F. Takahashi, M. D. Vangsness, M. D. Durbin, and W. J. Schmoll (1995) "An Experimental and Computational Study of Swirling Hydrogen Jet Diffusion Flames," ASME Paper 95-GT-307. To be published in the Transactions of the ASME.
5. M. S. Anand, S.B. Pope and H.C. Mongia (1993) "PDF Calculations for Swirling Flows," AIAA 93-0106. To be published AIAA Journal.
6. S. B. Pope (1992) "Particle Method for Turbulent Flows: Integration of Stochastic Differential Equations," Journal of Computational Physics.
7. S. B. Pope (1991) "Application of the Velocity-Dissipation Probability Density Function Model to Inhomogeneous Turbulent Flows," Physics of Fluids A, 3, No. 8-1, 1947-1957.
8. S. B. Pope (1991) "Combustion Modeling Using PDF Methods" in *Numerical Approaches to Combustion Modeling*, Eds. E. Oran and J. Boris, Progress in Astronautics and Aeronautics.
9. S. B. Pope and Y. L. Chen (1990) "The Velocity-Dissipation Probability Density Function Model for Turbulent Flows," Physics of Fluids A, 2, No. 8, 1437-1449.
10. M. S. Anand, S.B. Pope and H.C. Mongia (1990) "Pressure Algorithm for Elliptic Flow Calculations with the PDF method," CFD Symposium on Aeropropulsion, NASA CP-3078, 347-362.
11. S. B. Pope (1990) "The PDF Method for Turbulent Combustion," CFD Symposium on Aeropropulsion, NASA CP-3078, 335-346.
12. A. R. Masri and S. B. Pope (1990) "PDF Calculations of Piloted Turbulent Nonpremixed Flames of Methane," Combustion and Flame, 81, 13-29.
13. M. S. Anand, S.B. Pope and H.C. Mongia (1989) "Calculations of Axisymmetric Turbulent Jets by the PDF Method," Seventh Symposium on Turbulent Shear Flows, Stanford University, Stanford, 3.3.1-3.3.6.